

UNIVERSITY OF TECHNOLOGY, SYDNEY

Luminescence Studies of ZnO Crystals and Nanowires

by
Matthew Foley

A thesis submitted in partial fulfillment for the
degree of Doctor of Philosophy

in the
Department of Physics and Advanced Materials
Faculty of Science

2011

Declaration of Authorship

I, Matthew Foley, declare that this thesis titled,
'LUMINESCENCE STUDIES OF ZNO CRYSTALS AND NANOWIRES'
and the work presented in it are my own. I confirm that:

- This work was done wholly or mainly while in candidature for a research degree at this University.
- Where any part of this thesis has previously been submitted for a degree or any other qualification at this University or any other institution, this has been clearly stated.
- Where I have consulted the published work of others, this is always clearly attributed.
- Where I have quoted from the work of others, the source is always given. With the exception of such quotations, this thesis is entirely my own work.
- I have acknowledged all main sources of help.
- Where the thesis is based on work done by myself jointly with others, I have made clear exactly what was done by others and what I have contributed myself.

Production Note:

Signed: Signature removed prior to publication.

Date: 5 AUGUST 2011

“There is a theory which states that if ever anyone discovers exactly what the Universe is for and why it is here, it will instantly disappear and be replaced by something even more bizarre and inexplicable.

There is another theory which states that this has already happened.”

- Douglas Adams

“There are two possible outcomes: if the result confirms the hypothesis, then you’ve made a measurement. If the result is contrary to the hypothesis, then you’ve made a discovery.”

- Enrico Fermi

Abstract

ZnO is a direct semiconductor with a band gap of 3.4 eV at room temperature making it a hot topic for optoelectronic research across a broad range of applications. The current solid state lighting technology typically uses nitride semiconductors in the generation of light, more commonly gallium nitride. ZnO is a more efficient light generator than GaN owing to its high excitonic binding energy, and for this reason, ZnO is a potential material that may soon compete with GaN as a cornerstone of the solid state lighting revolution. Significant obstacles preventing the wide scale usage of ZnO include the lack of reliable p-type doping and high degree of uncertainty surrounding the nature of its defects, intrinsic n-type conductivity and optical properties.

The aim of this thesis is therefore to explore the luminescence and defect properties of doped and undoped ZnO nanowires and crystals.

During the project, ZnO nanowires were grown through a vapour deposition method under varying growth conditions. Changes in the choice of substrate, gas flows, pressures, and growth times were linked to changes in the structural and optical properties of the nanowires as characterised by scanning electron imaging and complementary spectroscopic techniques. Gold coated epitaxially matched sapphire substrates positioned close to the source material were found to produce highly aligned nanowires arrays. Cathodoluminescence (CL) imaging showed a localisation of defect luminescence near the surface of ZnO nanowire sidewalls. Oxygen deficiencies were also found to be localised on the sidewalls of the nanowires, supporting a correlation between green luminescence and oxygen vacancies in ZnO.

Post processing plasma modification of ZnO crystals and powders were used to identify defects contributing to the observable green luminescence. The defect emissions

were fitted with constrained Gaussian peaks which were linked to multiple competitive radiative centres. Variations in the near band edge (NBE) to green defect intensity ratios were also investigated to assist in the assignment of the defect peaks.

Incorporation of transition metals into ZnO was achieved through thermal in-diffusion and sol-gel preparation methods. Significant quenching of the defect related optical emissions relative to the UV emission was observed for both Mn doped samples, while an enhancement of the defect emission was observed near the surface of Fe doped crystals. Monochromatic CL imaging was shown to be an effective method of determining the depth of iron incorporation in iron doped ZnO crystals owing to the enhancement of the green emission.

Acknowledgements

I would like to thank my supervisors Dr. C. Ton-That and Prof. M. Phillips for all the support and opportunities they have offered me during my time as a student at the University of Technology, Sydney. Words cannot begin to express my gratitude for time and support they have given to me.

My thanks also extends to the team in the Microstructural Analysis Unit. Their assistance in preparation, data acquisition, sample analysis and general discussion have been invaluable tools in helping me complete my studies.

Within the MAU I would also like to thank my fellow students and colleagues. There have been a number of you over the years, and each of you have contributed in some way to my successes.

To the staff and students outside the lab, your insights into alternative solutions to issues were always welcomed, and for that I extend my gratitude. To my family and friends - your assistance and understanding have given me the strength to complete this mammoth effort.

To my wife Ginnie I would like to say a special thanks. Your support during the past few years has been incredible, and it is to you that I dedicate this work.

List of Publications and Presentations

Refereed Journal Publications

C. Ton-That, M. Foley, L.L.C. Lem, G. McCredie, M.R. Phillips, B.C.C. Cowie. Diffusion synthesis and electronic properties of Fe-doped ZnO.
Mat. Lett. 64, 3, 386-388, 2010.

M. Foley, C. Ton-That and M. R. Phillips. Luminescent properties of ZnO structures grown with a vapour transport method.
Thin Solid Films 518, 15, 4231-4233, 2010.

M. Foley, C. Ton-That and M. R. Phillips. Cathodoluminescence inhomogeneity in ZnO nanorods.
Appl. Phys. Lett. 93, 243104, 2008.

C. Ton-That, M. R. Phillips, M. Foley, S. J. Moody and A. P. J. Stampfl. Surface Electronic Properties of ZnO Nanoparticles.
Appl. Phys. Lett. 92, 26, 1-3, 2008.

C. Ton-That, M. Foley, and M. R. Phillips. Luminescent properties of ZnO nanowires and as-grown ensembles.
Nanotechnology 19, 415606, 2008.

Oral Presentations

M. Foley, C. Ton-That and M. R. Phillips. Spatially Inhomogeneous Defect Distribution in ZnO Nanorods.
Australian Microbeam Analysis Society XI, Canberra. February 2011.

M. Foley. Luminescence inhomogeneity in ZnO nanorods.
Australian Institute of Physics, NSW Branch, Postgraduate Awards. 2010.

M. Foley, C. Ton-That and M. R. Phillips. Cathodoluminescence characterisation of vapour transport grown ZnO structures.
2010 International Conference On Nanoscience and Nanotechnology, Sydney. February 2010.

M. Foley, C. Ton-That and M. R. Phillips. Local electronic structure and luminescence properties of ZnO nanowires.
SPIE Microelectronics, MEMS and Nanotechnology, Canberra. December 2007.

Poster Presentations

M. Foley, C. Ton-That and M. R. Phillips. Zinc oxide nanostructures and their cathodoluminescent properties.

NSW Branch of Materials Australia Jules Byrnes Student Presentation Evening. 2009.

C. Ton-That, M. Foley and M. R. Phillips. Luminescence properties of ZnO nanowires and as-grown ensembles.

SPIE Microelectronics, MEMS and Nanotechnology, Canberra. December 2007.

Contents

Declaration of Authorship	i
Abstract	iii
Acknowledgements	v
List of Publications and Presentations	vi
List of Figures	xii
List of Tables	xv
Common Acronyms	xvii
1 An introduction to ZnO	1
1.1 Brief overview of ZnO as an optoelectronic material	1
1.2 Motivation and aims of this work	3
1.3 Structure of thesis	4
2 Review of ZnO optical properties, fabrication and nanostructures	6
2.1 Crystal structure	7
2.2 Basic physical parameters for ZnO	7
2.3 Energy band gap	9
2.4 Band gap engineering	13
2.5 Defects in crystalline materials	14
2.5.1 Native point defects in ZnO	15
2.5.1.1 Vacancies	16
2.5.1.2 Interstitials	18
2.5.1.3 Impurities	19
2.5.1.4 Antisites	19
2.6 Exciton formation in ZnO	21
2.7 Luminescence	23
2.7.1 Recombination	23

2.7.1.1	Radiative recombination	23
2.7.1.2	Bound exciton luminescence	25
2.7.2	Non-radiative recombination mechanisms	27
2.8	Optical properties of ZnO	28
2.8.1	Near band edge emission	29
2.8.2	Green defect-related radiative recombination	30
2.8.2.1	Theoretical findings	30
2.8.2.2	Experimental findings	32
2.8.3	Yellow-orange emission	34
2.8.4	Red emission	34
2.9	Methods of ZnO growth	35
2.9.1	Chemical vapour deposition	35
2.9.2	Growth mechanisms	36
2.9.2.1	Vapour-solid	36
2.9.2.2	Vapour-liquid-solid	37
2.9.2.3	Vapour-solid-solid	42
2.9.3	Summary of growth mechanisms	42
3	Experimental techniques	44
3.1	Preparation procedures	44
3.1.1	Cleaning and preparation of growth substrates	44
3.1.2	Carbothermal reduction of ZnO	47
3.1.3	Furnace setup	48
3.1.4	Parameter ranges	50
3.1.4.1	Preparation of transition metal doped ZnO through in-diffusion	51
3.2	Characterisation techniques	52
3.2.1	Scanning electron microscopy	53
3.2.1.1	Cathodoluminescence	55
3.2.1.2	Depth resolved cathodoluminescence	57
3.2.1.3	Power density cathodoluminescence	58
3.2.2	Photoluminescence	60
3.2.3	Monte Carlo simulation	61
3.2.4	Synchrotron light techniques	62
3.2.4.1	Angle resolved	64
3.2.4.2	X-ray absorption near edge structure	65
3.2.5	X-ray diffraction	65
3.2.6	Ultraviolet-visible spectroscopy	67
4	Growth and characterisation of ZnO nanowires	69
4.1	A review on ZnO growth	69

4.2	Effects of growth conditions on nanostructures in relation to temperature and precursor vapour composition	71
4.2.1	Effect of substrate type on growth quality and orientation . .	73
4.2.2	Carrier gas	77
4.2.3	Growth seeds	80
4.2.4	Growth time	81
4.2.5	Distance from source	83
4.2.6	Summary of growth conditions on ZnO nanostructures	87
4.3	Relationship between structure and optical properties	89
4.3.1	Inhomogeneity in optical properties of ZnO structures	89
4.3.2	Luminescent properties of individual wires and as-grown ensembles	98
4.4	Conclusions	101
5	Luminescence properties of plasma-treated ZnO	103
5.1	A comprehensive review of plasma treated ZnO	103
5.2	Plasma experimental details	107
5.3	Plasma treatment of ZnO:Zn phosphor	110
5.4	Plasma treatment of ZnO powder	113
5.5	Plasma treatment of ZnO crystals	114
5.6	Summary of plasma results	118
5.6.1	ZnO:Zn phosphor	118
5.6.2	ZnO powder	119
5.6.3	ZnO crystal	120
5.7	Conclusions	120
6	Transition metal doping of ZnO	123
6.1	An overview of transition metal doped ZnO	123
6.2	Manganese doped ZnO	126
6.2.1	Manganese doped ZnO crystal	126
6.2.1.1	Analysis of Manganese in-diffused ZnO	128
6.2.2	Manganese doped nanoparticles	131
6.2.2.1	XANES analysis	131
6.2.2.2	X-ray diffraction	132
6.2.2.3	Ultraviolet-Visible spectroscopy	137
6.3	Iron doped ZnO	138
6.3.1	Analysis of Iron in-diffused ZnO	139
6.3.1.1	Synchrotron light analysis of Fe doped ZnO	139
6.3.1.2	Cathodoluminescence analysis of Fe doped ZnO . . .	142
6.4	Summaries	144
6.4.1	Mn-doped ZnO	145
6.4.2	Iron doped	145

7	Conclusions and future directions	146
7.1	Conclusions	146
7.2	Future directions	148
7.3	Closing remarks	149
A	Determination of circularity of a droplet	151
B	Derivation of Bragg’s Law for a hexagonal unit cell	153
C	Datasheets	156
	References	158

List of Figures

2.1	Crystal structures of ZnO	8
2.2	Crystallographic orientations in ZnO	9
2.3	Effect of temperature on the band gap of ZnO	12
2.4	Temperature resolved CL of ZnO NBE emission	12
2.5	Band gap vs. a-plane lattice constant for $Mg_xZn_{1-x}O$ and $Be_xZn_{1-x}O$ ternary alloys	14
2.6	Diagram of two types of defect in a crystalline materials	16
2.7	Schematic of point defects in a crystal	18
2.8	Formation energies of defects in ZnO as a function of the Fermi level	20
2.9	Thermal ionisation of excitons in ZnO and GaN as a function of tem- perature	22
2.10	Radiative recombination channels	24
2.11	Relevant bound excitons in ZnO	25
2.12	Typical CL spectrum for ZnO with identified peaks	29
2.13	Phase diagram for Au-Zn alloys	37
2.14	Schematic of VLS growth	39
2.15	Three proposed models for VLS growth	40
2.16	Schematic illustration of catalyst droplet formation with different con- tact angles	41
3.1	AFM scan of gold droplets	46
3.2	Fitted data showing size distribution of droplets formed by annealing gold films of different thicknesses	47
3.3	External view of three zone furnace	49
3.4	Internal of three zone furnace	50
3.5	SEM system utilised in this work	54
3.6	Schematic diagram of processes induced by electron bombardment . .	55
3.7	Collection of CL light through parabolic mirror	55
3.8	Penetration depth of incident electron in ZnO	57
3.9	Depth resolved CL of ZnO	59
3.10	Power density CL of ZnO	60
3.11	Electron interaction in ZnO	62
3.12	Influence of carrier diffusion on interaction volume	63

3.13	Accelerating voltage versus CL generation depth from Monte Carlo simulations	64
3.14	XRD plot of ZnO powder	66
3.15	Schematic of a UV-Vis experiment	67
4.1	SEM images of ZnO structures produced at different temperatures . .	72
4.2	Epitaxial relationship of ZnO on Al ₂ O ₃	74
4.3	Comparison of substrate choice	76
4.4	Comparison of gas flow conditions	79
4.5	Comparison of growth seeds	80
4.6	Comparison of CL spectra from different seeds	81
4.7	Influence of growth time on structure	83
4.8	Relative positioning of growth relative to source	84
4.9	CL spectra for ZnO structures formed at a distance from the source material	85
4.10	Example of ZnO structures formed at a distance from source material	86
4.11	Aligned rods grown on sapphire	90
4.12	XRD $\theta - 2\theta$ plot of ZnO nanorods shown in Figure 4.11	91
4.13	Rocking curve of (0002) plane from ZnO nanorods grown on <i>a</i> -plane sapphire	91
4.14	CL spectra obtained from the tip and the sidewalls of ZnO nanorods	92
4.15	CL spectra obtained from the sidewalls of ZnO nanorods at different accelerating voltages	93
4.16	Monochromatic images of ZnO nanorods showing localisation of CL emission	94
4.17	Monochromatic CL line scans of ZnO nanorods	95
4.18	Energy bands in ZnO with depletion regions	96
4.19	Schematic diagram of ARPES experiment	97
4.20	Comparison of the O 1s XPS spectra of the nanorods acquired at different photoelectron detection angles	98
4.21	Extraction of individual nanowires	99
4.22	CL comparison of extracted and as grown wires	100
5.1	Hydrogen interstitials in ZnO	106
5.2	Typical CL spectra obtained from H ₂ plasma treated ZnO:Zn phosphors	109
5.3	Plasma chamber	110
5.4	CL emissions from plasma treated ZnO:Zn	111
5.5	CL emissions from plasma treated ZnO	113
5.6	Comparison of CL spectra for ZnO crystals subjected to different plasma treatment methods	115
5.7	Depth resolved plots for ZnO crystal subjected to different plasma conditions	116

6.1	EDX plot of pre- and post- annealed Mn-coated ZnO	127
6.2	CL spectra of Mn doped ZnO single crystals	128
6.3	Relative intensity ratios of NBE and DL for Mn coated and uncoated ZnO crystals as a function of annealing time	130
6.4	XANES of Mn doped ZnO powder	132
6.5	XRD pattern for Mn doped ZnO	133
6.6	c/a ratio as a function of Mn nominal concentration in Mn-ZnO powders	134
6.7	Williamson-Hall plots for Mn doped ZnO powders	136
6.8	UV-Vis absorption edge for Mn doped ZnO	137
6.9	Band gap obtained for Mn-ZnO powders from UV-Vis and CL	138
6.10	XANES spectra of Fe in-diffused ZnO crystal	140
6.11	Valence-band photoemission spectra of ZnO crystal	141
6.12	CL spectra comparing ZnO crystals with and without Fe in-diffusion	143
6.13	Stitched CL image of cleaved iron in-diffused crystal	143
6.14	Cleaved ZnO crystal showing the impact of Fe incorporation on the CL emission	144
A.1	Comparison of as-scanned and processed annealed gold film	152
B.1	Schematic for manipulation of Bragg's Law for hexagonal unit cell . .	154

List of Tables

1.1	Comparison of different wide band gap semiconductors	2
2.1	Properties of ZnO	10
2.2	Defect formation energies for native point defects in ZnO.	21
2.3	Summary of bound exciton lines in ZnO at low temperature	26
3.1	Parameter ranges for furnace growth	50
3.2	CASINO simulation parameters for depth approximations	63
4.1	Substrate lattice parameters	75
4.2	Summary of growth conditions and resulting nanostructures	88
5.1	ZnO samples utilised in plasma treatment experiments	108
5.2	Summary of hydrogen plasma treatments for Zn doped ZnO	108
5.3	Fitted peak values for plasma treated ZnO:Zn phosphor	112
5.4	Fitted peak values for plasma treated ZnO powder	114
5.5	Fitted peak values for plasma treated ZnO crystal	114
6.1	Oxidation and charge states of Mn and Fe	125
6.2	Integrated areas of the NBE and deep level peaks for Mn doped ZnO at different annealing times. 30 kV accelerating voltage, 3.3 nA beam current	129
6.3	Integrated areas of the NBE and deep level peaks for Mn doped ZnO at different annealing times. 10 kV accelerating voltage, 10 nA beam current	130
6.4	Calculated lattice constants for Mn doped ZnO from experimental data	134
6.5	Summary of results from Williamson-Hall calculations on Mn doped ZnO powders	135
C.1	ZnO single crystal substrate supplied by MTI Corporation	156
C.2	Zn doped ZnO phosphor supplied by Phosphor Technology	157
C.3	20 nm ZnO supplied by Nanostructured & Amorphous Materials . . .	157
C.4	ZnO powder supplied by Antaria (formerly Advanced Nanotechnology Ltd.)	157

Common Acronyms

Notation	Description
A ⁰ X	acceptor bound exciton.
AFM	atomic force microscope.
ARPES	angle resolved photoemission spectroscopy.
CL	cathodoluminescence.
CVD	chemical vapour deposition.
D ⁰ X	donor bound exciton.
DCL	depth-resolved cathodoluminescence.
DFT	density functional theory.
DL	deep level.
DLE	deep level emission.
DMS	dilute magnetic semiconductor.
FWHM	full width at half maximum.
GL	green luminescence.
LED	light emitting diode.
LO	longitudinal optical.

Notation	Description
NBE	near band-edge.
PDCL	power-density resolved cathodoluminescence.
PES	photoemission spectroscopy.
PL	photoluminescence.
sccm	standard cubic centimetres per minute.
SEM	scanning electron microscope.
SLS	synchrotron light source.
TM	transition metal.
UV	ultraviolet.
UV-Vis	ultraviolet-visible spectroscopy.
VLS	vapour-liquid-solid.
VS	vapour-solid.
VSS	vapour-solid-solid.
XANES	x-ray absorption near edge structure.
XPS	x-ray photoemission spectroscopy.
XRD	x-ray diffractometry.

Chapter 1

An introduction to ZnO

ZnO is an optoelectronic material with highly efficient light emission at room and higher temperatures that is a strong candidate for future lighting and other energy saving devices. Furthermore, it is possible to tailor the electronic, magnetic, and optical properties of ZnO through doping, alloying, quantum wells, heterostructures, and nanoengineering. This gives rise to a variety of possibilities in technologically important devices such as laser diodes, transparent electronics, and spintronic devices. Understanding the role of defects and their influence on the optical and electronic properties of ZnO is extremely important in many of these applications.

1.1 Brief overview of ZnO as an optoelectronic material

ZnO was one of the first semiconductors - along with germanium and silicon - to be grown with a purity level necessary to allow extensive characterisational studies. The characterisation of the material can be traced back as far as the early 20th century, with lattice parameters being identified by Fuller in 1929 [1], and refined from Bunn in 1935 [2] through to Gray [3] in 1954 and Reeber [4]. While the

piezoelectric properties were the initial focus of interest, it is the use of wide band-gap semiconductors in optoelectronic devices that has garnered the attention in recent decades. Wide band-gap semiconductors, such as ZnS, ZnSe, SiC, GaN, SnO₂ and ZnO, tend to show similar characteristics, as evidenced in Table 1.1.

Currently, GaN is considered the leading material for solid state lighting devices, owing to the strong emission characteristics and the ability to produce both *n*– and *p*– type materials. ZnO has a considerable advantage over GaN for use in light emitting diodes (LEDs) and UV lasers. The large excitonic binding energy of ZnO gives rise to a lower level of thermal ionisation of excitons at room temperature, allowing intense near band-edge excitonic emission at room temperature and above. This, in turn, hints at the possibility of room temperature optoelectronic devices with higher luminescence efficiencies than those currently available based on III-nitride materials.

Initially ZnSe and GaN based technologies and devices were able to produce short wavelength LEDs and injection lasers, however ZnSe has been known to produce unwanted defect levels when subjected to high drive currents. SiC, being an indirect band gap semiconductor, does not produce a bright light emission.

Room temperature lasing has also been observed in ZnO structures [5, 6]. In addition, ZnO possesses a high level of radiation stability [7–9] and is amenable to wet

TABLE 1.1: Comparison of different wide band gap semiconductors

Material	Typical structure	Lattice parameter		E_g (eV at RT)	Melting point (K)	Exciton binding energy (meV)
		a (Å)	c			
ZnO	Wurtzite	3.250	5.206	3.3	2248	60
GaN	Wurtzite	3.189	5.185	3.4	1973	21
ZnSe	Zinc-blende	5.667	-	2.7	1790	20
ZnS	Wurtzite	3.824	6.261	3.7	2103	36
6H–SiC	Wurtzite	3.08	15.12	3.0	3100	-
SnO ₂	Tetragonal rutile	4.737	3.185	3.6	1603	33

chemical etching [10]. The high radiation resistance lends ZnO to development of possible space applications, while the chemical etching - both in acids and alkalis - provides an opportunity for the large-scale fabrication of small devices. The similarities between the lattice parameters and identical crystalline structure of ZnO to GaN also means that ZnO can be utilised as a substrate for the epitaxial growth of high quality GaN films [11, 12].

Doping or alloying ZnO with transition or alkaline earth metals allows the manipulation of the band gap through a range of values. The introduction of magnesium to ZnO can result in a blue shift - or increase - of the band gap, while the addition of cadmium induces a red shift. Band gaps of 3.04 eV (9.1 atomic% Cd) to 3.99 eV (16.8 % Mg) have been reported [13]. These values allow for the production of tunable ultraviolet (UV) light between 310 nm and 400 nm. While other materials already have the capacity to emit light in this spectral range, the intense UV emission intensity offered by ZnO could potentially open the door for ultra high efficiency white light sources when coupled with a suitable phosphor.

1.2 Motivation and aims of this work

The focus of this work is to produce ZnO nanostructures and investigate their inherent optical properties. ZnO can exhibit a low luminescence efficiency owing to intrinsic defects, and it is these defects or impurities that can significantly affect the optical emissions by offering alternative radiative recombination channels to electron-hole pairs, or by quenching the overall emission by providing non-radiative recombination centres. The origin of the broad yellow-green peak often observed in ZnO is typically attributed to point defects, however the identification of the nature of the defects involved has been subject to considerable debate for the past 60 years. Theoretical and experimental results are often conflicting, and issues associated with incorrect assignments plague the literature with inaccurate conclusions.

It has been observed that defects in ZnO can be removed or passivated through doping with transition metal elements or post processing under plasma environments.

Utilising complementary luminescence characterisation techniques, the identification and spatial distribution of defects in nanostructured ZnO will be studied and compared to the defects observed in bulk samples. Furthermore, the introduction of extrinsic donor materials to ZnO will be investigated with respect to changes in the physical, chemical and electronic properties when compared to reference samples.

The main aims of this work can be summarised as:

- A comprehensive investigation into the effects of growth conditions on the formation of defects in ZnO and their influence on the optical properties
- Identification of the spatial distribution of luminescence centres and defect related emissions in ZnO
- Investigation into the effects of plasma treatments postprocessed ZnO on the surface effects and optical emission properties
- Investigation into transition metal incorporation through thermal in-diffusion and sol-gel methods, focusing on changes to the optical properties and chemical states of the dopants in ZnO

The overarching aim of this work is to investigate the origin of defects in ZnO with the intention of producing a level of control of the optical emission properties.

This work will systematically address these objectives, along with establishing the impact of this research within the current understanding of ZnO.

1.3 Structure of thesis

This thesis focuses on the study and analysis of the optical, electronic and morphological properties of nanoscale, powder and single crystal ZnO samples. This thesis can be divided into three sections;

- Outline and background of ZnO - Chapters 1 & 2
- Experimental details - Chapter 3
- Experimental results and conclusions - Chapters 4-7

Chapter 1 provides an overview of the research along with a brief background to place the work in context Chapter 2 introduces a comprehensive review of the current knowledge and research focus of ZnO, including the issues surrounding the present understanding of the nature of intrinsic defects and optical properties. Chapter 3 describes the various experimental characterisation and sample preparation techniques that apply across the investigatory chapters. Chapter 4 focuses on the growth and analysis of nanowires produced through a carbothermal method, specifically the influence of growth conditions on the morphology and optical properties of the resulting ZnO nanowires. Chapter 5 examines the effects of post-processing of ZnO materials through plasma treatment under different environments on the optical emissions. Chapter 6 investigates the impact of transition metal incorporation into ZnO crystals and powders. Chapter 7 offers a summary of the conclusions and an suggestion of possible future research directions.

Chapter 2

Review of ZnO optical properties, fabrication and nanostructures

ZnO is a wide band-gap (3.37 eV) [14] compound semiconductor with potential applications in a wide variety of optoelectronic devices, from ultraviolet (UV) lasers through to white light sources. The high exciton binding energy (60 meV [15]) makes excitons stable in ZnO at room temperature and above. UV luminescence has been reported from a variety of ZnO structures including disordered nanoparticles and thin films. Furthermore, as ZnO has a lack of central symmetry owing to its wurtzitic structure it can exhibit piezo- and pyroelectric properties. In addition, ZnO is a versatile material with a diverse range of growth morphologies including combs, rings, springs, wires and cages [5, 6, 16–19]. The ease with which these structures form - at comparatively low costs - offer promising potential for future devices. ZnO is also attractive for use with biomedical applications as it is considered biologically safe. In order to better understand the nature of ZnO, it is first necessary to investigate its structural and optical properties, and examine how they relate to potential ZnO applications.

2.1 Crystal structure

Under standard pressure and temperature, ZnO crystallises to a wurtzite structure [20] as shown in Figure 2.1. Wurtzite is a hexagonal lattice, belonging to the P6₃mc space group with lattice parameters of $a=0.3296$ nm and $c=0.52065$ nm. The structure of ZnO can be thought of as alternating planes of tetrahedrally coordinated O^{2-} and Zn^{2+} ions stacked along the c -axis. It is this tetrahedral coordination that gives rise to the noncentral symmetric structure, resulting in the piezo- and pyroelectric properties observed in ZnO. There are four surfaces of interest in ZnO - nonpolar $(10\bar{1}0)$ and $(11\bar{2}0)$ surfaces, and polar (0001) -Zn and $(000\bar{1})$ -O surfaces (see Figure 2.2). The non-polar surfaces are formed by breaking the same number of zinc and oxygen bonds and thus contain an equal number of the two ions, while the polar surfaces are either Zn or O terminated. These polar surfaces result in spontaneous polarisation along the c -axis. In order to maintain a stable structure, polar surfaces tend to undergo significant surface reconstruction or have faceting, however $ZnO \pm (0001)$ surfaces show atomically flat, stable faces, without any reconstruction [21, 22].

In addition to the wurtzite phase, ZnO can also crystallise into either cubic zincblende or rocksalt structures, also shown in Figure 2.1. Zincblende ZnO is stable only when grown on cubic structures, such as gallium arsenide [23], while the rock-salt structure is a high-pressure metastable phase obtainable only at high pressures (≈ 10 GPa) [20, 24, 25]. There is also a fourth possible phase - cubic caesium chloride - that has been theoretically predicted, however this would only occur at extremely high temperatures and has not yet been observed [26].

2.2 Basic physical parameters for ZnO

A compilation of the basic physical properties of ZnO can be found in Table 2.1. It is worth noting that there is still considerable uncertainty in some of the values

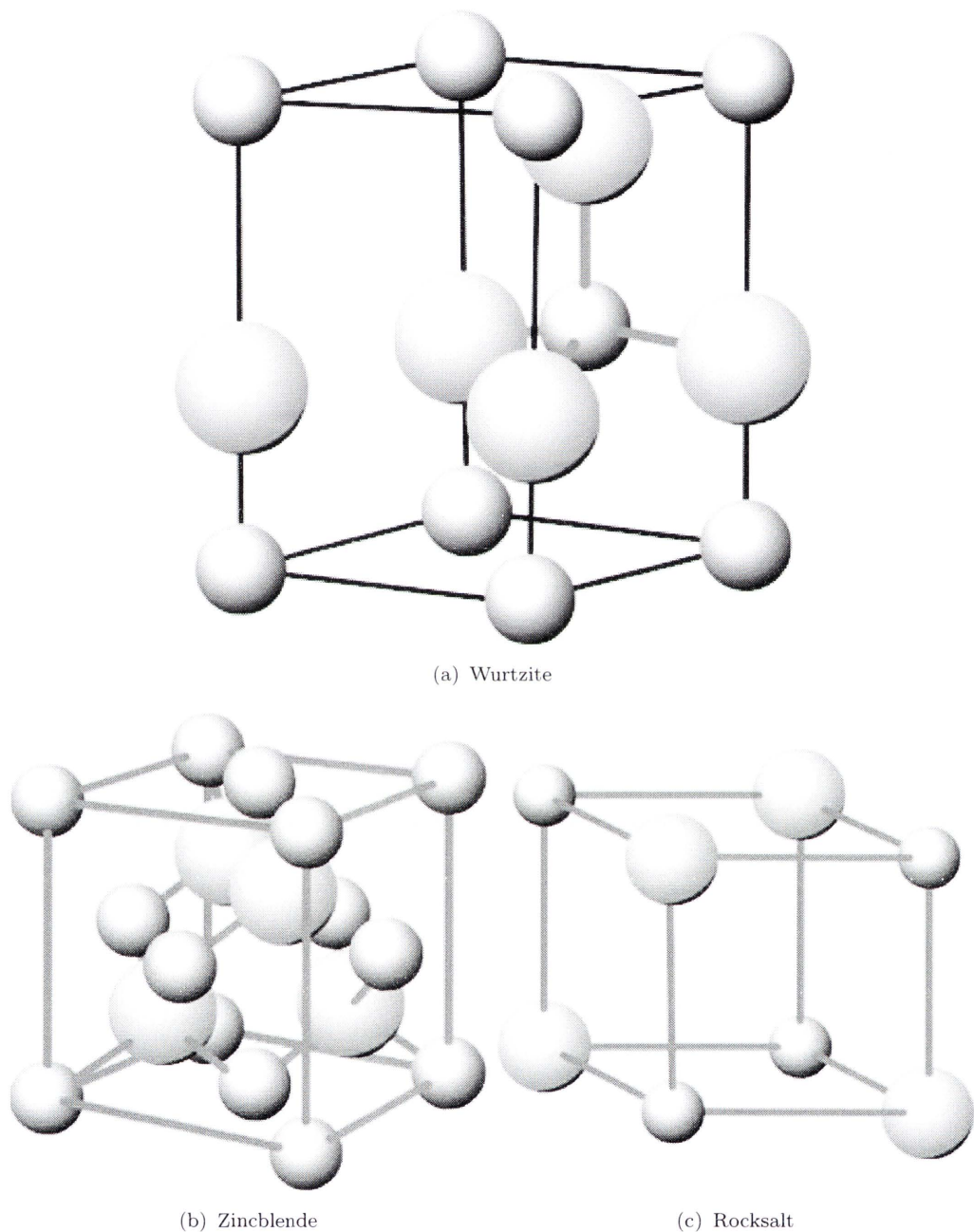


FIGURE 2.1: Unit cells for the common crystal structures of ZnO. The wurtzite structure is Zn-0001 terminated, while the zincblende also shows zinc terminated faces. Large and small atoms represent oxygen and zinc atoms respectively.

above, particularly in p-type ZnO where debate continues over whether or not p-doping really has been achieved at all. As there have been limited presented reports of p-type ZnO, the hole mobility and effective mass values are still under review. The thermal conductivity results show some spread of values, possibly due to the

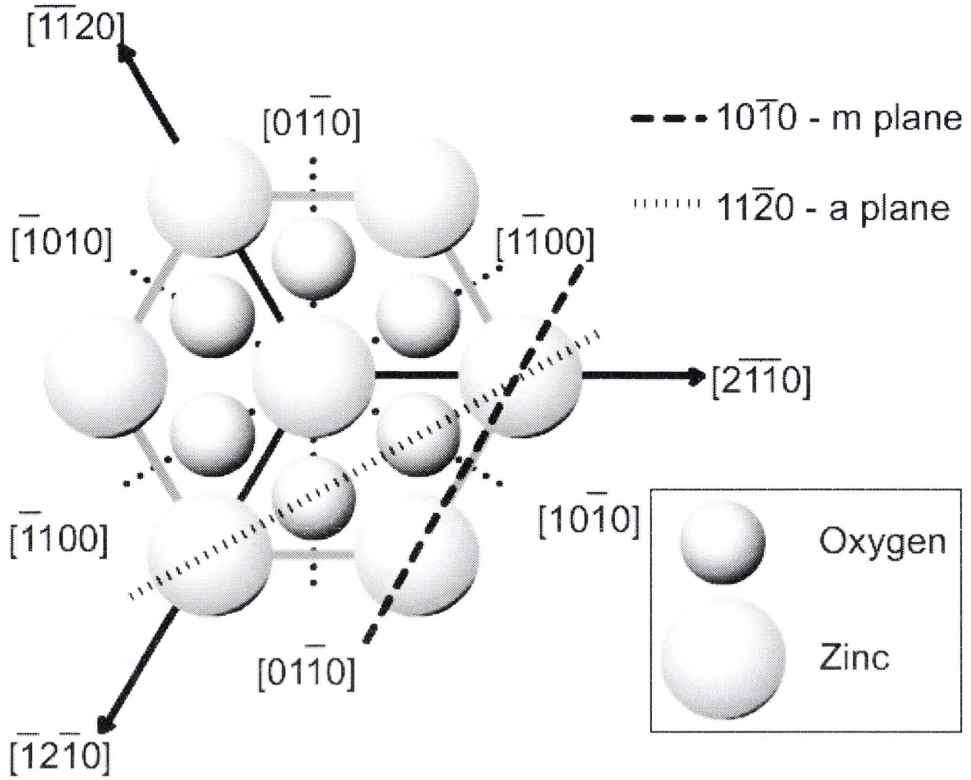


FIGURE 2.2: Common crystallographic orientations for ZnO in the wurtzite phase. The $(11\bar{2}0)$ and $(10\bar{1}0)$ planes and associated directions are shown as projections along the Zn- (0001) plane.

influence of defects in ZnO samples, as was found to be the case for GaN [27]. Carrier mobility values will likely rise as increased control over defects and compensation effects in ZnO is achieved.

2.3 Energy band gap

The band structure of a semiconductor is a vital piece of knowledge in solid state physics and materials engineering. Theoretical techniques have had varying degrees of success in determining the band structure of ZnO for its various structures that have then been compared to experimentally obtained data.

One of the earliest works on ZnO band structure calculations was proposed by

TABLE 2.1: Properties of ZnO

Physical parameter	Value
Lattice parameters at 300 K	
a	3.2496 Å
c	5.2065 Å
Density	5.606 g/cm ⁻³
Melting point	1975°C
Energy gap	3.37 eV (direct)
Exciton binding energy	60 meV
Intrinsic carrier concentration	< 10 ⁶ cm ⁻³ (max n-type doping > 10 ²⁰ cm ⁻³ electrons, max p-type doping < 10 ¹⁷ cm ⁻³ holes)
Electron effective mass	m _e [*] = 0.24 m _e
Hole effective mass	m _h [*] = 0.59 m _e
Hall mobility at 300K	
Electron	200 cm ² /Vs
Hole	5-50 cm ² /Vs

Rössler [28] in 1969, and since then several experimental works have been performed on wurtzite ZnO showing a discrepancy with his findings on the bulk material [29–32]. Langer and Vesely [29] reported experimental data relating to the core energy levels via x-ray induced photoemission spectroscopy. Their work suggested two conclusions - the unambiguous determination of the location of the Zn 3d level and the discrepancy between the theoretically determined energy levels and that the experimental data was angular momentum dependant.

UV photoemission experimental work has been conducted on the non-polar (10 $\bar{1}$ 0) face of hexagonal ZnO cleaved under vacuum [30, 31] that has placed the Zn 3d core level approximately 7.5 eV below the valence band, 3 eV lower than Rössler’s band calculation prediction. This value agrees with further experimental work from Vesely et al.[33] and Ley et al.[32], who reported 8.5 eV and 8.81 eV respectively. Girard et al.[34] have studied the electronic structure of the ZnO (0001) surface via ARPES for both normal and off-normal emission spectra. This yielded valuable information about the bulk and surface electronic states as well as further elucidating the Zn 3d states. From the spectra obtained, the dispersion of the four valence bands in

the (0001) direction have been compared to the calculations based on LDA work [35] with significant agreement between the experimental data and the theoretical expectations.

The polar (0001)-Zn and (000 $\bar{1}$)-O surfaces have also been subject to experimental and theoretical investigation. Girrard et al. [34] have identified two surface states on the (0001) surface; one state at 7.5 eV, the other at 4.5 eV. The first surface state was predicted by theory and has been attributed to the backbonding of the Zn 4s-O 2p hybridized bulk states, while the second state was not predicted, it has been related to the Zn 4s-O 2p derived states.

The impact of temperature on the band gap of ZnO has also been investigated, and the band gap has been found to shrink with increasing temperature as given by the empirical relationship (and shown in Figure 2.3)

$$E_g(T) = E_{g(T=0)} - \frac{\alpha T^2}{T + \beta} \quad (2.1)$$

where $\alpha = -5.5 \times 10^{-4}$ eV K $^{-1}$ and $\beta = -900$ K for temperatures up to 300 K. Excitonic transition energies have also shown a similar temperature dependence with $\alpha = -7.2 \times 10^{-4}$ eV K $^{-1}$ and $\beta = -1077$ K [36]. Furthermore, the spectral line shape of the band gap also varies as a function of temperature. As temperature decreases, the individual peaks that contribute to near band edge emission can be resolved. This can be observed in Figure 2.4, where the band edge emission shifts from a single broad peak centred at 3.17 eV at 270 K through to three clearly identifiable peaks separated by $E_{LO}=70$ meV (excitonic, 1-LO and 2-LO) at 80 K. The change in spectral shape can be attributed to phonon coupling.

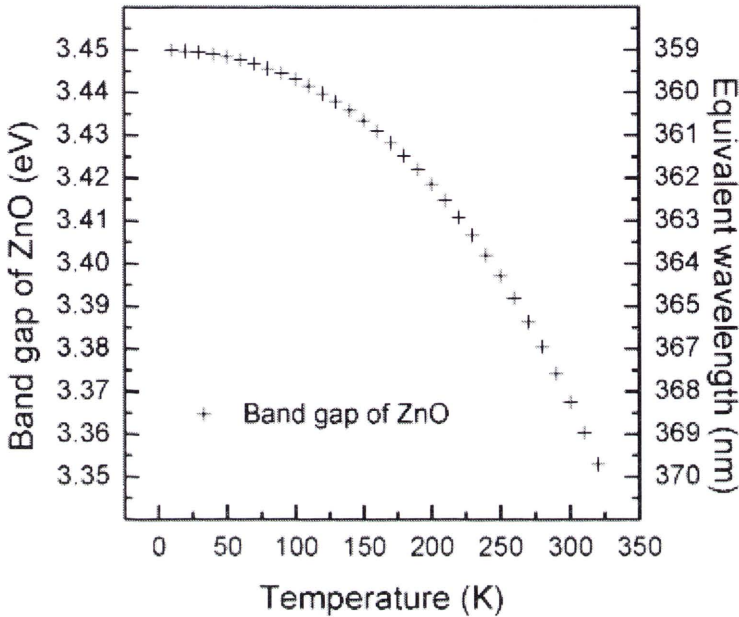


FIGURE 2.3: Relationship between the band gap of ZnO and temperature based on the empirical relationship in Equation 2.1 in the temperature range 0-350 K. The equivalent wavelength for recombinations occurring over this band gap are also indicated on the right hand axis.

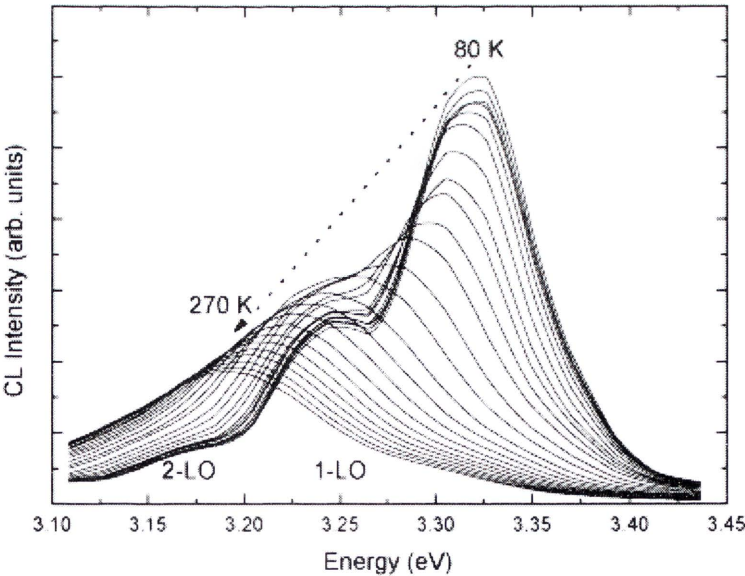


FIGURE 2.4: CL spectra obtained from ZnO with increasing temperature from 80 and 270 K. At low temperature the emission is separated into three resolvable peaks that merge together as the temperature increases

2.4 Band gap engineering

The band gap of ZnO can be manipulated to give a variety of values through alloying techniques. This allows for the potential development of such devices as UV detectors or field effect transistors. It has been found that $\text{Mg}_x\text{Zn}_{1-x}\text{O}$ and $\text{Be}_x\text{Zn}_{1-x}\text{O}$ alloys lead to an increase in the band gap, while $\text{Cd}_x\text{Zn}_{1-x}\text{O}$ reduces the band gap. The energy gap of a ternary semiconductor can be determined from Equation 2.2, which is an application of Vegard's Law [37], where b is a bowing parameter and E_{AO} and E_{ZnO} are the band gap energies for the alloy compound (MgO, CdO or BeO) and ZnO respectively.

$$E_g = (1 - x)E_{\text{ZnO}} + xE_{\text{AO}} - bx(1 - x) \quad (2.2)$$

The bowing parameter is dependant on the difference in electronegativity between ZnO and alloy compound.

It should also be noted that the lattice parameters of the material also undergo variation with the introduction of alloy materials. Comparing the a -plane lattice parameter to the band gap of the Mg- and Be- based ternary semiconductors as x varies from 0 to 1 yields a plot shown in Figure 2.5. For Be-ZnO alloys, the band gap increases to a maximum of 10.6 eV (when $x = 1$) while maintaining a wurtzitic structure, as the equilibrium state of BeO is wurtzite. By contrast, Mg-ZnO exhibits two different structures. As MgO is a cubic system, when $x \gtrsim 0.6$ the Mg-ZnO will present as a rocksalt system, while when $x \lesssim 0.4$ it instead will be wurtzite. When the composition ranges $0.4 \lesssim x \lesssim 0.6$, the quality of the material is poor owing to the mixed cubic-wurtzite structures that occur.

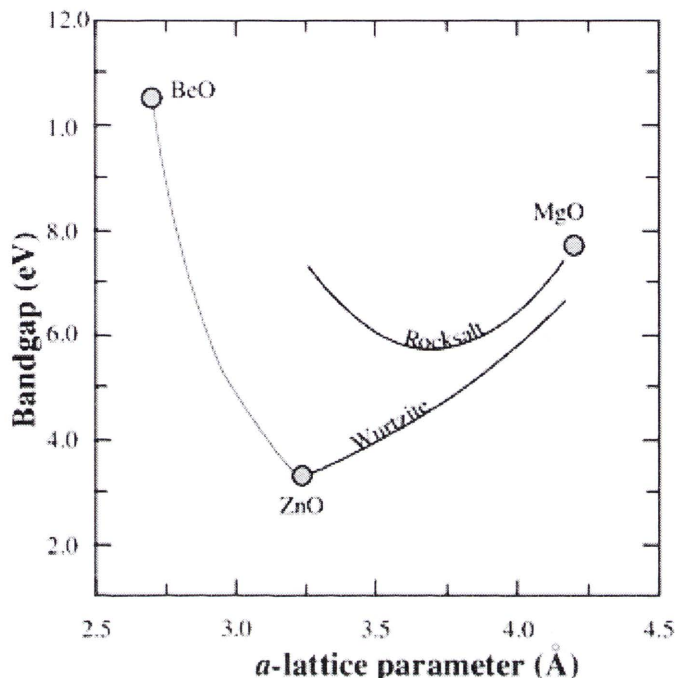


FIGURE 2.5: Band gap vs. a-plane lattice constant for $\text{Mg}_x\text{Zn}_{1-x}\text{O}$ and $\text{Be}_x\text{Zn}_{1-x}\text{O}$ ternary alloys. While the band-gap vs. composition of $\text{Mg}_x\text{Zn}_{1-x}\text{O}$ is comparatively well known, $\text{Be}_x\text{Zn}_{1-x}\text{O}$ intermediaries are not. Adapted from Izyumskaya et al. [38].

2.5 Defects in crystalline materials

Crystalline solids, such as ZnO, typically contain a wide variety of imperfections in their crystal structure. These crystallographic defects the lattice fall into a variety of classifications.

Line

There are two basic types of line defect - edge and screw. It is also possible to have a “mixed” defect combining both types. An edge defect, or dislocation, is caused by a plane of atoms terminating in the middle of the crystal. When this occurs, the adjacent atomic planes are not flat, but bend around the edge of the ending plane so that the crystal structure remains ordered on either side. A screw dislocation is similar, but instead of an edge, a helical path acts as the localisation of the defect. Dislocations are able to move if the surrounding

planes break their bonds to rebond with the atoms at the terminating edge as a result of thermal activation [39]. These defects result from lattice strain.

Planar

There are several forms of planar defects. Grain boundaries, where the crystallographic direction within the lattice changes abruptly, can occur when two crystals growing independently meet. Stacking faults are also considered planar defects. If a stacking sequence (such as ABCABCABC) is interrupted by one or two layers, this is known as a stacking fault (ABCAB~~ABC~~AB).

Bulk

Bulk defects can occur as voids - small regions where there are no atoms in which case they can be treated as vacancy clusters, or clustered impurities which can form regions of a different phase.

Point

When a defect does not extend through a crystal in any given direction it is referred to as a point defect. While there are no strict size limitations on how “small” a point defect should be, the term is typically used to describe defects involving single atoms (or the vacancy left by a missing atom).

2.5.1 Native point defects in ZnO

The point defects in ZnO are of considerable interest as they have been tentatively identified as the origin of several electronic properties of bulk and nanostructured material. A defect can act as a shallow or deep level defect. Shallow defects only require a small amount of energy to ionise, typically on the order of $k_B T$. Deep defects require energies larger than the thermal energy to ionize so that only a fraction of the defects present in the semiconductor contribute to free carriers. Deep level defects which are more than five times the thermal energy away from either band edge are very unlikely to ionize. In this case, the deep level defects can be

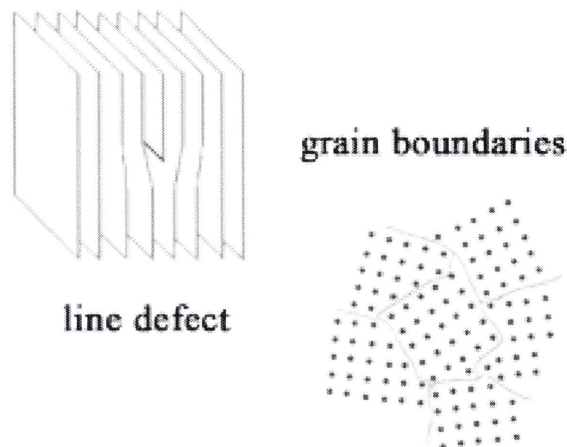


FIGURE 2.6: Examples of line and grain boundary defects in a crystalline material. A line defect occurs when a crystalline plane stops abruptly inside the material, causing planes located on either side to bend around the edge to keep crystalline order. Grain boundaries occur at the interface between different crystallographic directions, often when multiple crystals form next to each other

effective recombination centers in which electrons and holes recombine with each other. Such deep defects are often referred to as deep level traps.

2.5.1.1 Vacancies

Vacancies, such as zinc (V_{Zn}) or oxygen (V_{O}) in ZnO, are sites in the lattice that are usually occupied by an atom that remain empty ((a) in Figure 2.7). These defects can propagate through nearby neighbouring atoms moving to fill the vacant site. The stability of the surrounding crystal region ensures that the vacancy defect does not collapse.

In ZnO, first-principle calculations have consistently shown that V_{O} is a deep defect donor, where the $1+$ charge state is thermodynamically unstable. If the Fermi energy is above the $0/2+$ level, the defect is found in the neutral charge state. If the Fermi energy is below the $0/2+$ charge transition transfer level however, the defect has a $+2$ charge. This $0/2+$ level for V_{O} has been calculated to be 0.5-0.8 eV above the valence-band maximum [40–42]. Calculations that allow for the band gap

error of the local density approximation have estimated the $0/2+$ level to be 1-2 eV below the conduction band minimum [43–46], with the migration barrier for V_O to be ≈ 2 eV [47, 48], or ≈ 1.7 eV for V_O^{2+} [48]. Computational studies are unclear as to whether oxygen vacancies should occur in n -type ZnO, with some predicting defect concentrations of $\sim 10^{17} \text{ cm}^{-3}$ [45] while others claim that the formation energy is too high for significant concentrations to be found at equilibrium [48]. Irradiating ZnO with electrons shows that V_O can be converted to V_O^+ at low temperatures [49], with the vacancies being stable up to 400°C [50]. $V_{\text{Zn}}^{/2-}$ can be transformed under similar conditions to $V_{\text{Zn}}^{0/1-}$.

A Zn vacancy defect, V_{Zn} , is a double acceptor with first-principle calculations identifying the $0/1-$ and $1-/2-$ levels to be 0.1-0.2 and 0.9-1.2 eV above the valence-band maximum respectively [48, 51, 52]. Evans *et al.* [53] have estimated that the ground state for the 1- charge state can be found at 0.9 eV above the valence band. Janotti and Van de Walle [48] propose that the transition from a shallow donor level to the $1-/2-$ acceptor level associated with V_{Zn} could result in luminescence around 2.5 eV. Their suggestion is supported by the observation that hydrogen plasma treated ZnO samples show a reduced green luminescence intensity, consistent with V_{Zn} hydrogen passivation [54].

V_O has commonly been attributed to the ubiquitous green luminescence band centred around 2.4-2.5 eV (approximately 510nm) [50, 55, 56] due to an excited-to-ground state transition [57]. Annealing in O_2 or Zn vapour environments produces emission lines at 2.35 and 2.53 eV respectively, while annealing in ZnO powder eliminates both lines. This result suggests that the 2.35 eV emission is due to V_{Zn} while the 2.53 eV emission is due to V_O [58]. Furthermore, defects found at 2.1 eV have also been assigned to V_{Zn} through positron annihilation spectroscopy [59]. The green luminescence in ZnO and the role of vacancies will be further explored in Section 2.8.

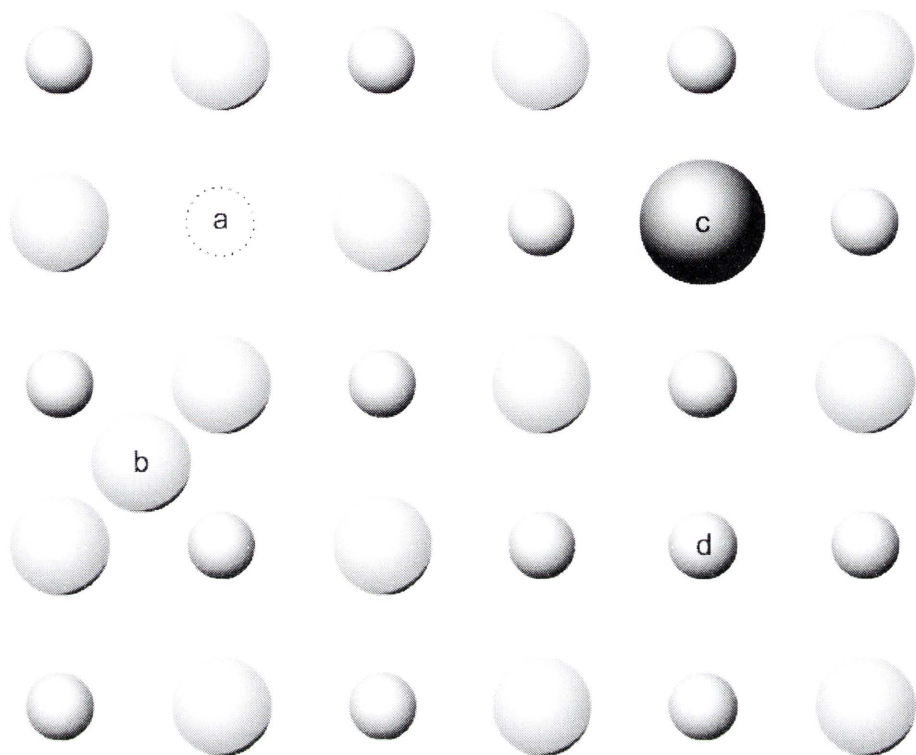


FIGURE 2.7: Examples of point defects in a ZnO crystal where small and large spheres represent oxygen and zinc respectively. a) an oxygen vacancy (V_O), b) a zinc interstitial (Zn_i), c) a substitutional impurity at a zinc site such as Li_{Zn} , d) an oxygen antisite (O_{Zn})

2.5.1.2 Interstitials

Interstitial defects occur when an atom occupies a site in the crystal structure at which an atom would not usually be found - not at a regular lattice site ((b) in Figure 2.7). In ZnO, zinc interstitials (Zn_i) are shallow donors that have a high formation energy in n -type ZnO [48]. They also have a migration barrier that can be as low as 0.57 eV, resulting in instability at room temperatures [43]. While there is a general consensus that zinc interstitials are not stable, complexes involving nitrogen impurities and Zn_i could exist as stable shallow donors [60].

2.5.1.3 Impurities

An impurity in a crystal can occur as either an interstitial or a substitutional defect (refer to (c) in Figure 2.7). In the case of a substitutional defect, there are two sub-cases; isovalent and aliovalent substitution. Isovalent substitution is where the impurity has the same charge as the ion that it is replacing, while aliovalent substitution is where the charge is either sub- or supervalent. Aliovalent substitutions change the total charge balance within the ionic compound, meaning that a charge compensation mechanism is required to keep the ionic compound neutral.

Unintentional doping as a result of impurities can create donor and acceptor levels within the crystal. As reviewed by Meyer *et al.* [61], photoluminescence peaks in ZnO at liquid helium temperatures have been attributed to excitons bound to elements, such as hydrogen, gallium, indium and aluminium¹. A broad green luminescence centred at 2.2 eV is often attributed to Cu in ZnO, following on from early works which found a fine structure in the peak as a result of copper impurities[62].

2.5.1.4 Antisites

If a type A atom - typically located at the corners of a cubic lattice - is instead found at the centre of the lattice - the usual location of type B - then this defect is known as an antisite defect, as the atom is not an impurity, a vacancy, or found at an otherwise unoccupied location ((d) in Figure 2.7). For ZnO, either O_{Zn} or Zn_O can occur, representing an oxygen atom located at the Zn position in the lattice and vice versa.

The native defects of ZnO are of interest as they can influence to the optical and electronic properties. Point defects are the most commonly investigated, as several intrinsic defects have low formation enthalpies and thus are likely to form readily

¹See Table 2.3 in Section 2.7.1.2 on page 25

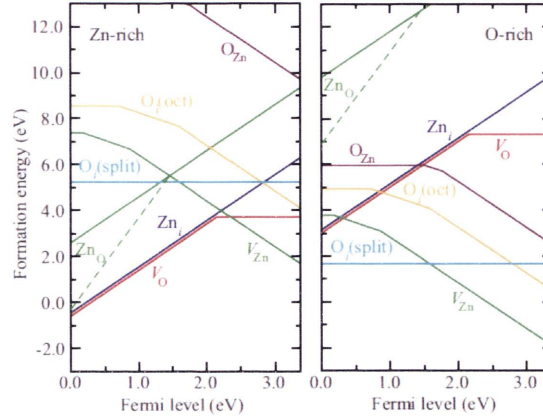


FIGURE 2.8: Formation energies of point defects in ZnO as a function of the Fermi level for Zn- and O- rich growth conditions. The zero of the Fermi level is set at the valence band maximum. The slopes of the segments indicate the charge state of the defect, and sharp changes in the gradient indicate charge state transitions. From Janotti and Van de Walle [48].

[63], while not normally appearing to be the cause of the unintentional n-type conductivity² in ZnO [51]. The point defects tend to occur as either deep donors (in the case of V_O) or compensating acceptors (such as V_{Zn}).

The location of defects in ZnO can be summarised utilising an energy diagram such as the one shown in Figure 2.8, which has been generated from theoretical computational studies.

A summary of the intrinsic defects and their formation energies can be found in Table 2.2.

The temperatures presented in the table indicate the temperature at which one could expect a defect to spontaneously occur as a result of gaining sufficient thermal energy. These temperatures are important to note when post-processing ZnO samples - temperatures need be considered when drawing conclusions regarding formation or reduction of defects.

² Zn_i related defects have been considered, but there is still considerable debate as to their influence

TABLE 2.2: Defect formation energies for native point defects in ZnO.

Defect	Charge state	E ^f (eV)
V _O	2+	-0.60
	+	1.91
	0	3.72
V _{Zn}	0	7.38
	-	7.55
	2-	8.43
Zn _i	2+	-0.45
	+	3.20
	0	6.95
O _i (oct)	0	8.54
	-	9.26
	2-	10.86
O _i (split)	2+	5.25
	+	5.24
	0	5.24
Zn _O	4+	-0.31
	3+	1.57
	2+	2.59
	+	6.49
	0	10.47
O _{Zn}	0	13.15
	-	14.68
	2-	16.45

Adapted from Janotti and Van de Walle [48]

2.6 Exciton formation in ZnO

When an electron is excited from the valence band to the conduction band, it leaves behind a hole. It is possible for the electron and the hole to correlate to form a quasiparticle known as an exciton. The number of excitons formed depends on the temperature of the crystal and the exciton binding energy, E_b , through the relationship in Equation 2.3.

$$N_{ex} \propto \exp\left(\frac{-E_b}{k_b T}\right) \quad (2.3)$$

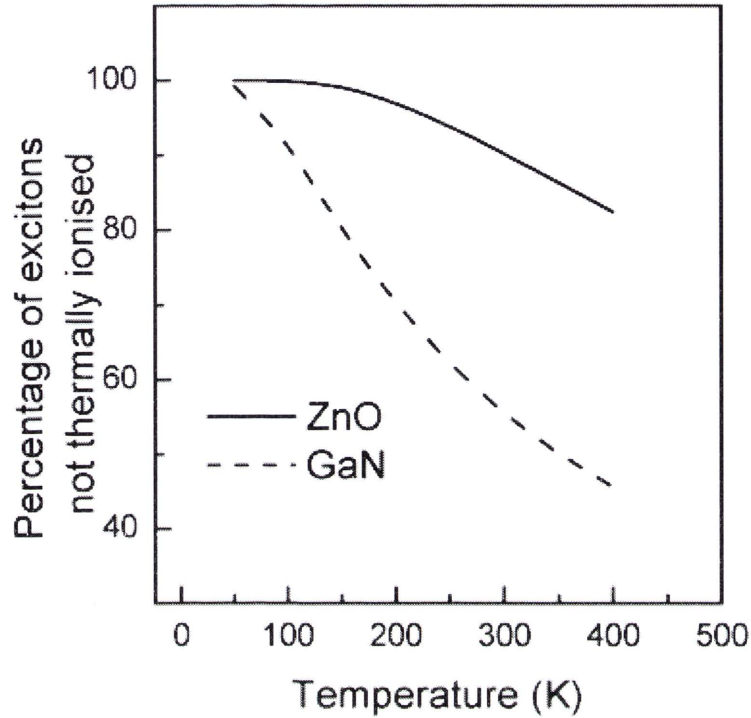


FIGURE 2.9: Thermal ionisation of excitons in ZnO and GaN as a function of temperature based on Equation 2.3. At 300 K, approximately 45% of excitons formed in GaN will be thermally ionised, whereas only 10% of excitons in ZnO are lost to thermal ionisation.

$$\text{As } T \rightarrow +\infty, N_{\text{ex}} \rightarrow 0$$

A comparison between ZnO and GaN shows the remaining excitons to be substantially higher for ZnO up to 500K owing to the higher exciton binding energy. This can be best shown in Figure 2.9 which shows the considerable difference between the excitonic efficiencies of the two materials under conditions near room temperature. The substitution of ZnO based devices for those currently utilising GaN technology would clearly result in higher efficiency. Once formed, excitons are able to travel in a particle-like fashion through the semiconductor lattice without a net charge transfer.

2.7 Luminescence

Luminescence is the general term used to describe radiative emission from a solid or powder following the introduction of an external energy source. While there are several types of luminescence, for ZnO it is worth focussing on just two forms - photo- and cathodoluminescence. These two luminescence mechanisms can be distinguished by the source of the energy used for excitation; photoluminescence occurs as a result of photon absorption from incident light, while cathodoluminescence is due to electron bombardment typically using an electron microscope or cathode ray tube.

2.7.1 Recombination

There are two types of transitions involving electron-hole pair recombination in semiconductors - radiative recombination and non-radiative recombination. Radiative recombination is the emission of a single photon with an energy equal to (or near) the band-gap energy of the semiconductor. Non-radiative recombination does not involve the emission of light, but instead the excess energy is converted to vibrational energy in the form of quantised crystal lattice vibrations known as phonons.

2.7.1.1 Radiative recombination

When an electron is excited from the valence band to the conduction band, it leaves behind a hole. The excited electron is then able to recombine with the hole, emitting the excess energy in a variety of ways. The different recombination channels are shown in Figure 2.10. The energy of the emitted photon can be converted from eV to a wavelength using $\lambda = \frac{1239}{eV}$. From this, it can be seen that as the recombination of the electron hole pair occurs over shorter gaps, the energy of the emitted photon

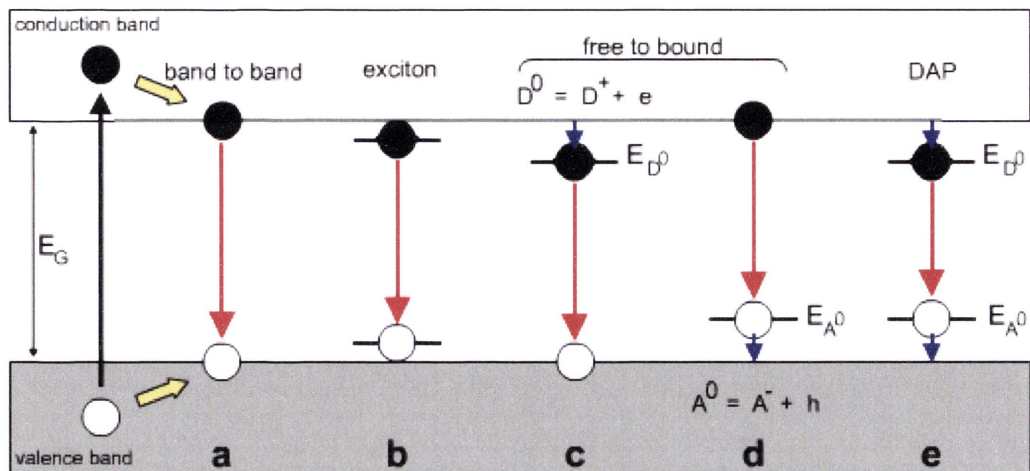


FIGURE 2.10: Schematic diagram of the radiative recombination channels possible as a result of an excitation of an electron-hole pair.

	Recombination channel	Energy of emitted photon	Notation
a)	Band to band	E_g	
b)	Bound (donor or acceptor) and free exciton	$E_g - E_x$	$[D^0X]$, $[A^0X]$, $[F^X]$
c)	Donor to free hole	$E_g - E_{D^0}$	$[D^0, h]$
d)	Free electron to acceptor	$E_g - E_{A^0}$	$[e, A^0]$
e)	Donor-acceptor pair	$E_g - E_{D^0} - E_{A^0} + \frac{q^2}{4\pi\epsilon_0\epsilon_r}$	$[D^0, A^0]$

decreases, producing a red-shit observed in the increased wavelength of the emitted light.

Band to band recombination occurs when an electron drops from its excited state in the conduction band to fill an empty hole state in the valence band. This results in emission of a photon with an energy equal to that of the band gap (Figure 2.10a). If an exciton forms, either as a free or bound exciton, the energy gap between the electron and the hole is slightly diminished, owing to the Coulombic attraction. As a result, when the electron-hole pair recombines, the energy of the emitted photon is equal to $E_g - E_x$ (Figure 2.10b). For ZnO, the near band-edge (NBE) UV emission peak tends to be dominated by excitonic emissions, rather than direct band to band, due to the high electron-hole pair binding energy.

Once an exciton has formed, it can propagate through the lattice where it can potentially be trapped by a defect or scattered by phonons, typically longitudinal optical

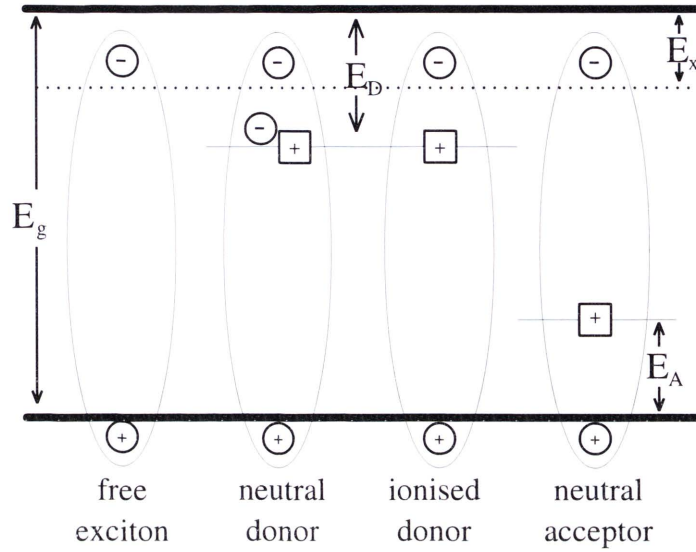


FIGURE 2.11: Relevant bound excitons in ZnO. The Coulombic binding of the electron in the conduction band to the hole in the valence band reduces the free exciton energy from that of the band gap by E_x . Excitons can be bound with either a neutral donor (D^0X) or neutral acceptor (A^0X).

(LO) phonons. An exciton in ZnO will only reach the surface of the semiconductor if it is formed near the surface due to reabsorption effects. The exciton “escape depth” is defined as the inverse extinction coefficient at the exciton energy. For ZnO, this depth is approximately $a^{-1}(E_x) \approx 70$ nm.

2.7.1.2 Bound exciton luminescence

If the temperature of the sample is sufficiently low ($T \lesssim 230\text{K}$), excitons are frequently found to be localised at defect sites in the lattice due to Coulomb binding of one carrier in the correlated electron-hole pair to the defect. The exciton luminescence that results from this bound exciton is thus redshifted from the energy of the free exciton by an amount corresponding to the localisation energy of the exciton to the defect. This is commonly cited as Hayne’s Rule [64]. Bound excitons in ZnO are commonly attributed to neutral shallow donors, although ionised donors and neutral acceptors have also been reported.

TABLE 2.3: Summary of bound exciton lines in ZnO at low temperature

Exciton line	Photon energy (eV)	Identified impurity
F^X	3.3767	-
I_0	3.3724	Al
I_1	3.3711	Ga
I_{1a}	3.3691	-
I_2	3.3677	-
I_3	3.3664	-
I_{3a}	3.3654	Zn_i
I_4	3.3629	H
I_5	3.3614	-
I_6	3.3605	Al
I_{6a}	3.3604	-
I_7	3.3600	-
I_8	3.3597	Ga
I_{8a}	3.3593	-
I_9	3.3564	In
I_{10}	3.3530	-
I_{11}	3.3483	-

Figure 2.11 shows the difference in transition for the bound exciton as compared to the free exciton. The Coulomb binding of the electron in the conduction band to the hole in the valence band reduces the free exciton energy from that of the band gap. The exciton's energy is then further reduced if it is bound to a donor or acceptor. Low temperature spectra obtained for ZnO have been found to contain a vast number of bound exciton complexes. The most prominent lines are labelled as I lines, with I_n where $n = 0, 1, 2, \dots$ in order of decreasing energy, following the notation used in early work on the subject [65]. A summary of the identified bound exciton lines can be found in Table 2.3 as found in literature [61, 66].

There is a considerable amount of controversy regarding the assignment of the I lines as found in Table 2.3 to various donor or acceptor bound excitons. There is general consensus, however, that I_3 - I_8 are due to donor bound excitons (D^0X_s), while I_9 - I_{11} have been suggested as either due to D^0X [61] or acceptor bound excitons

(A^0Xs) [67]. The I_0 - I_2 lines have been attributed to D^0X [67, 68] or excitons bound to ionised donors [61]. The study of bound excitonic luminescence provides information regarding the identity and impurities, as well as their relative concentrations, in a given ZnO sample.

2.7.2 Non-radiative recombination mechanisms

There are three main physical methods with which non-radiative recombination can occur; non-radiative via deep level, Auger recombination and surface recombination.

Non-radiative via deep level

Defects in the crystal structure are the most common cause resulting in non-radiative recombination. Point defects such as impurities, vacancies, interstitials and antisites can significantly alter the electronic properties of a semiconductor. It is common to have these defects form energy levels within the forbidden gap which act as efficient recombination centres. These levels are often referred to as traps or NBE luminescence killers owing to their promotion of the non-radiative processes or deep level emissions. Rather than releasing the energy gained through the recombination of the electron hole pair in the form of light, these defects instead can produce quantised vibrational quasiparticles known as phonons. These phonons vibrate through the lattice, dispersing the released energy as heat to the material and surrounding environment.

Auger recombination

Energy from the recombination can be given to a third carrier which is then excited to a higher energy level without shifting to another energy band. This third carrier then normally loses the excess energy to thermal vibrations in the semiconductor. Owing to the need to have a third particle present, Auger recombination is significant only in conditions when the carrier density is very

high. The generation process itself is not easily produced as the third particle would have to start in the unstable high-energy state.

Surface recombination

Substantial non-radiative recombination can occur at the surface of semiconductors. A surface is a disruption to the periodicity of the crystal lattice, which in turn leads to a variation in the band structure of the semiconductor. This variation can include the addition of electronic states within the forbidden gap of the semiconductor.

Atoms at the surface can not have the same bonding structure as the bulk atoms due to the lack of neighbouring atoms. Some of the valence orbitals do not form chemical bonds, leaving partially filled electron orbitals - dangling bonds. It is these dangling bonds that can act as recombination centres, and depending on their charge state they can be either acceptor or donor states. Dangling bonds can also act as non-radiative recombination centres, producing phonons rather than photons. However, the surface states on the non-polar surfaces of ZnO are resonant with the conduction and valence bands and thus do not significantly contribute to recombination processes [69–71]. It is possible to passivate the surface of a semiconductor to reduce the number of surface states through methods such as shallow doping or the epitaxial growth of a capping layer.

2.8 Optical properties of ZnO

Zinc oxide has a characteristic emission spectra comprising of two main peaks - the NBE emission at 3.3 eV and the broad defect related band occurring at 2.3 eV [14]. The NBE is dominated by FX and D⁰X emission [61], along with LO phonon replicas (the peaks labelled in Figure 2.12) while the green band is attributed to defect related recombination mechanisms.

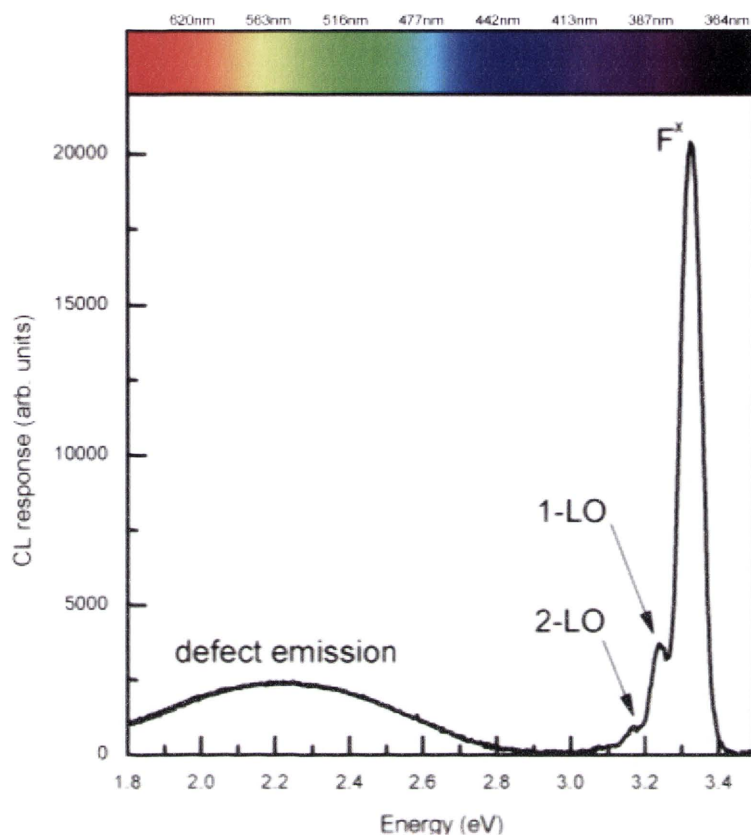


FIGURE 2.12: Typical CL spectrum for ZnO at 80K identifying F^X , 1-LO and 2-LO. Coloured bar at top represents approximate wavelength corresponding to energy of each peak.

2.8.1 Near band edge emission

While band to band transitions are the dominant recombination mechanism for an electron hole pair in high quality crystals, they are not necessarily the only method resulting in radiative emission. As seen in Figure 2.10, the recombination energy gap can be reduced by the coulombic force arising between an electron-hole pair in an exciton. This can be further reduced through donor or acceptor bound excitons, reducing the emitted energy from the recombination noticeably. This reduction in the emission energy gives rise to the near band-edge (NBE) peak observed in excitonic materials such as ZnO.

At liquid helium temperatures, it is possible to separate the narrow NBE peak into individual components, allowing for identification of different impurities and bound

defects. As the temperature increases, these peaks broaden and merge as calculated by Equation 2.4 [72];

$$\Delta\lambda_0 = \frac{2kT\lambda_0^2}{hc} \quad (2.4)$$

At room temperature, the full width at half maximum (FWHM) of a peak centred at 380 nm could be expected to broaden by as much as 6 nm. Typically the NBE at room temperatures is treated as a single broad³ emission centred at an energy just below the fundamental band gap. This is also influenced by the thermal ionisation of the various bound excitons.

2.8.2 Green defect-related radiative recombination

A variety of models have been proposed to explain the green emission from ZnO. It is widely accepted that the emission occurs as the result of either native defects or unintentional impurities, with point defects such as V_O or Zn_i , along with Cu interstitials, being investigated thoroughly. However, there is still no conclusive result to identify the origin of the emission.

2.8.2.1 Theoretical findings

Kohan et al [51] and Van de Walle [73] have used first principle calculations to establish the formation energies and electronic structure of the native point defects in ZnO. In their theory, the concentration of a defect within a crystalline structure depends upon its formation energy (E_f) as shown in Equation 2.5, where N_{sites} represents the concentration of crystal sites where the defect can occur. The lower the formation energy, the higher the equilibrium concentration of the defect; conversely

³Broad relative to the component excitonic emission peaks, but still narrow in comparison to the defect emission bands

a higher formation energy indicates a lower probability of defect formation [51].

$$c = N_{sites} \exp \left(-\frac{E^f}{k_B T} \right) \quad (2.5)$$

The formation energy of a point defect in a given charge state (q) is given by Equation 2.6 where $E^{tot}(q)$ represents the total energy loss of a system consisting of n_{Zn} and n_O , which represent the number of zinc and oxygen atoms respectively, μ_{Zn} and μ_O are the chemical potentials for zinc and oxygen, and E_F is the Fermi energy.

$$E^f(q) = E^{tot}(q) - n_{Zn}\mu_{Zn} - n_O\mu_O - qE_F \quad (2.6)$$

The chemical potentials for this relationship rely on the environment conditions during growth. Under zinc rich and oxygen rich growth conditions, it is possible to assign bulk chemical potentials to the system ($\mu_O = \mu_{O(bulk)}$ and $\mu_{Zn} = \mu_{Zn(bulk)}$). For intermediate ratios where the system is not particularly zinc or oxygen rich, $\mu_O < \mu_{O(bulk)}$ and $\mu_{Zn} < \mu_{Zn(bulk)}$, however the chemical potentials for both zinc and oxygen are in equilibrium with ZnO - $\mu_{Zn} + \mu_O < \mu_{ZnO}$.

Kohan et al. [51] have calculated the defect formation energy for a variety of native point defects in ZnO as a function of the Fermi level. They concluded that the two most common defects in ZnO are likely to be vacancies of oxygen or zinc. The oxygen vacancies have lower formation energy than zinc interstitials, and so are more likely to form in zinc rich growth conditions, while oxygen rich conditions should yield zinc vacancies. Furthermore, they suggested that the green luminescence emissions commonly observed in ZnO as transitions attributed to zinc vacancies, similar to earlier predictions regarding gallium vacancies causing yellow luminescence in GaN [74].

Defects in semiconductors can also arise as a result of the presence of other elements within the material - either deliberately or accidentally introduced during production or through post treatment methods. Hydrogen impurities in ZnO have been

investigated by first-principle calculations similar to methods outlined above. In contrast to other semiconducting materials, where hydrogen is amphoteric, hydrogen in ZnO always acts as a donor[73]. Hydrogen binds tightly with oxygen atoms in ZnO to form an OH bond of approximately 1\AA , either opposite to the Zn-O bond, or forming in the Zn-O bond (Zn-H-O) (see Chapter 5). In *n*-type ZnO, hydrogen incorporation formation energy is only 1.56eV, while in (theoretical) *p*-type samples the incorporation is more promising, suggesting that the introduction of hydrogen into ZnO during the growth process may increase acceptor solubility and inhibit the native formation of compensatory defects in a manner similar to the doping of GaN with Mg. If this is the case, then the issue of *p*-type doping is instead reduced to finding an efficient method of hydrogen extraction, potentially through post-growth annealing [14].

In terms of deliberate introduction of defects to produce *p*-type ZnO, nitrogen has been predicted as the shallowest acceptor [75]. Furthermore, it has been demonstrated that while N_O may be a shallow acceptor, $(\text{N}_2)_\text{O}$ is a double-shallow donor and there exists a competitive interaction between the N and N_2 during the doping process, which in turn controls the doping type [76]. In light of this, it has been suggested that N_2 or N_2O is not an effective doping method for the production of *p*-type ZnO due to the presence of the strong N-N bond, while N_O or NO_2 molecules can easily form N_O acceptors.

2.8.2.2 Experimental findings

Early studies explicitly attributed the broad green peak to copper impurities [62], however more recent evidence has suggested the defect was more likely to be related to V_O [55]. Both defect mechanisms offer plausible arguments, and it has been further proposed that there are two co-existing defects with similar energies resulting in the emission characteristics in this region of the spectrum. Experimental evidence

shows that copper impurities tend to result in a fine structure within photoluminescence spectra at liquid helium temperatures, while native point defects (such as V_O or V_{Zn}) give a structureless band at the same position with a similar width.

Vanheusden et al. [55] have also shown correlations between the concentrations of free electrons and V_O defects with the intensity of the green band. Through annealing experiments under both oxidizing and reducing environments, strong evidence was provided supporting V_O as the mechanism supporting the origin of the green defect band. This interpretation of the results has come under scrutiny however as the electron paramagnetic resonance signal used by Vanheusden to identify the oxygen vacancies (and thus their concentration in the ZnO) was in fact subsequently found to be related to an isotropic shallow donor level [77].

These optically detected magnetic-resonance studies also showed that the g values obtained for the structureless green band are different from those obtained for the fine structured green emission, thus supporting the observation of two different defect origins for the green band. Leiter et. al. [77] support V_O as the defect responsible for the structureless band, demonstrating similarities of this defect with anionic vacancies in other ionic crystals such as BaO, SrO, CaO and MgO. They also presented a model [78] whereby the two electron ground state of the neutral V_O is a diamagnetic singlet state where absorption of a photon transfers the system into a singlet excited state, relaxing nonradiatively into an emissive paramagnetic state that can be detected via optically detected magnetic resonance studies.

More recently, this structureless band has been attributed to a V_{Zn} [51, 79–81] or a defect complex incorporating Zn_i [82], O_{Zn} [83] or V_O [55, 77, 78, 84]. Furthermore, different electron transitions have been used to explain the green luminescence, such as $[D^0, h]$ -type recombination [55] (an oxygen donor level near the conduction band with the valence band), $[D^0, A^0]$ [80, 81] (any donor level to a deep V_{Zn} acceptor level), $[e, A^0]$ [51] (from the conduction band to the V_{Zn} acceptor) or an intracentre transition between two states of V_O [77], for example. Early suggestions of V_O

acting as a donor with $2+/+$ and $+/0$ levels near the conduction band have been investigated in detail in recent times [73]. From this work, it has been predicted that the only defect level found in ZnO relating to V_O is the $2+/0$ found at approximately 2.7 eV above the valence band. Further findings have shown that other proposed transitions are either energetically unfavourable [55] or, in cases such as D-*h*-type recombination in similar *n*-type semiconductor, highly improbable [85].

2.8.3 Yellow-orange emission

Evans *et al.* [53] have estimated that V_O ground state lies ≈ 2.1 eV below the conduction band minimum, resulting in a broad absorption band near 3.0 eV (409nm) and an emission band around 590 nm. Other works have indicated that the yellow/orange defect emission observed in ZnO can be associated with excess oxygen [84], specifically oxygen interstitials when produced using hydrothermal methods [86, 87], or related to dopants such as Li [88]. Lithium occupies a zinc site (Li_{Zn}), forming an energy state 150 meV above the valence band, with a second energy state occurring at 250 meV above the valence band maximum following increased Li concentrations [89]. This is likely due to a two-fold change in the ZnO - firstly a substitution of Li for V_{Zn} sites followed by the expected Li_{Zn} substitutions [90].

2.8.4 Red emission

ZnO has been observed to emit in the red region of the spectrum when annealed in Zn vapour at 1100°C. This emission is typically linked to an excess of Zn [91–95]. If the ratio of Zn to O is considered, an excess of Zn could be considered equivalent to an oxygen deficiency, however there is a significant difference between Zn_i and V_O at the atomic level. It has been observed that the red colour can also be induced by annealing in the presence of phosphorous or titanium instead of zinc vapour [93, 95], suggesting that V_O is more likely. Zinc and oxygen vacancies are annealed out

below 200° and 400°C respectively, or can form merged clusters which then anneal below 700°C [50, 59, 96]. After annealing however, the red remains, suggesting that another defect is the cause. Recent work shows that hydrogen in combination with an oxygen deficiency, rather than Zn_i is responsible. In samples containing hydrogen that exhibit red emission, the addition of oxygen has been shown to turn the ZnO clear. This suggests that red ZnO is a consequence of oxygen deficiencies in the presence of hydrogen [97].

2.9 Methods of ZnO growth

As remarked earlier, ZnO growth has been studied extensively in the optoelectronic fields. The strong tendency to grow with (0001) preferential orientation on a variety of substrates [98–100] has led to the development of several different growth techniques. Early work with epitaxial thin film growth focused on magnetron sputtering [100, 101] and chemical vapour deposition techniques [102–104], however the films produced were generally polycrystalline in nature.

2.9.1 Chemical vapour deposition

Chemical vapour deposition (CVD) is a growth technique for ZnO whereby a source material (typically a 1:1 weight mixture of ZnO powder and graphite) and a substrate are placed inside a growth furnace in such way that the temperature of the source material is higher than that of the substrate. A chemical agent can be used as both a sublimation activator and a transport agent to carry vapour species and deposit them onto the substrate to reform solid structures. CVD technique is useful for growing at low temperatures where the vapour pressure due to sublimation of the materials is too low to allow a growth using a sublimation-and-re-condensation process. Because the vapour pressures of ZnO at temperatures between 900-1200°C are low the CVD ZnO growth technique use a carrier gas as a vapour transport

agent so that an appreciable growth rate can be achieved. The maximum growth rate for ZnO pure crystal using this technique is about 0.1 mm/hr [105].

2.9.2 Growth mechanisms

Various models have been proposed to elucidate the growth mechanism behind CVD. Catalyst free vapour-solid (VS) processes are one of the more popular vapour phase synthesis methods, while vapour-liquid-solid (VLS) mechanisms have been used to produce faster, more controlled growth. VLS utilises a catalytic liquid alloy phase that adsorbs a vapor to supersaturation levels, from which crystal growth subsequently occurs. A clear understanding of the physical processes that occur during VLS growth is still under considerable debate. The complexity of the Au-Zn phase diagram (Figure 2.13) if compared to that of Au-Si or Au-Ge suggests that there is only a small temperature range within which vapour deposition growth can occur. It is necessary to consider a variety of possible mechanisms that may explain the growth of ZnO nanostructures. There are several proposed theories, and the following section will discuss them in more detail.

2.9.2.1 Vapour-solid

A typical VS process has the vapour phase generated through evaporation followed by chemical reduction or oxidation as required. These gaseous species are subsequently transported and condensed onto a substrate placed in a zone at a lower temperature than that of the source material. The decomposition of ZnO is comparatively simple, but does require high temperatures ($\approx 1400^{\circ}\text{C}$). Nanorods and nanowires have been successfully produced in this manner through the evaporation of commercial ZnO powder [16, 107, 108]. As lower temperatures and lower defect densities are often desired for ease of fabrication, a more direct method can be employed by heating Zn powder at $\approx 500\text{-}700^{\circ}\text{C}$ under an oxygen flow, however the Zn:O ratio

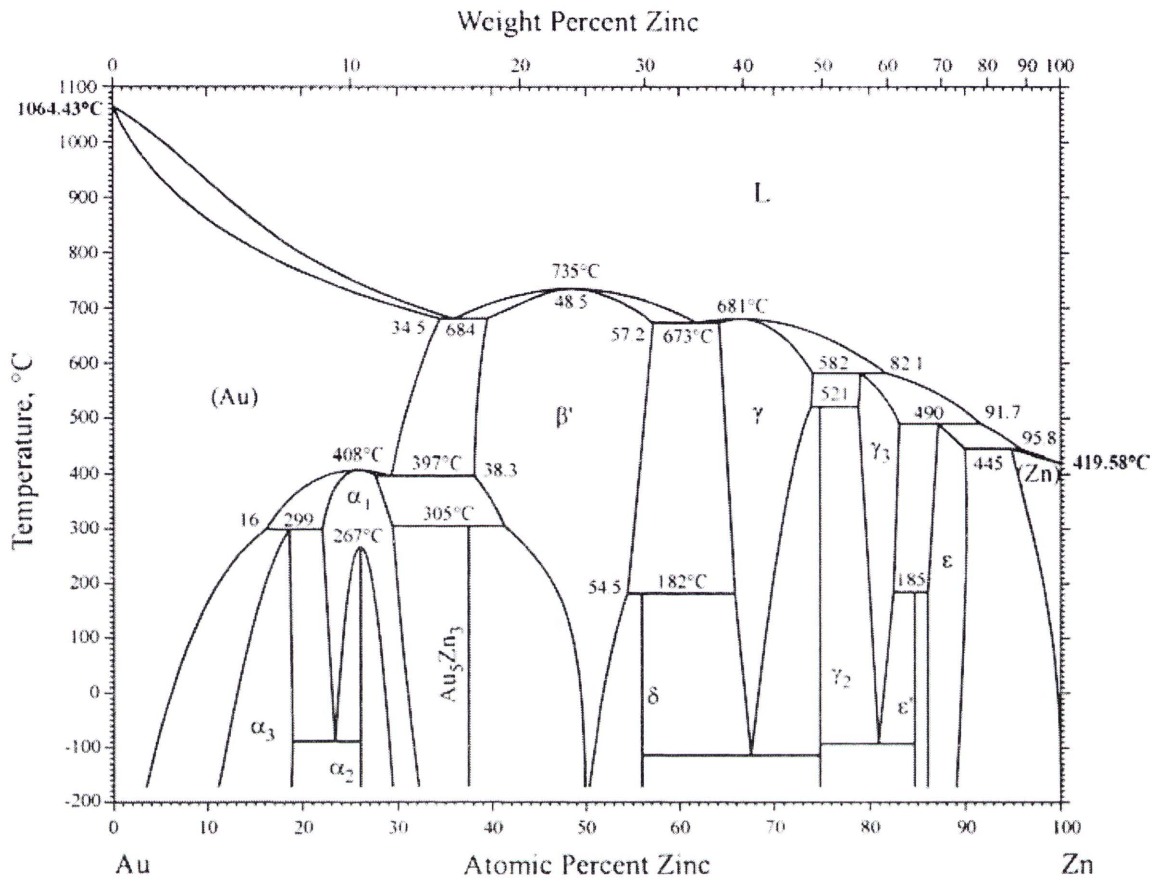


FIGURE 2.13: An Au-Zn phase diagram showing the various phases for Au-Zn alloys. From Okamoto [106].

must be monitored and controlled carefully to obtain desired nanostructures. While the method is simple experimentally, the process and mechanisms may involve the formation of intermediaries due to the higher temperatures employed. Furthermore, this method provides little to no control over the location of the subsequent growth of the nanostructures.

2.9.2.2 Vapour-liquid-solid

VLS is a mechanism that is employed as an explanation for the growth of low-dimensional structures from CVD processes. The use of VLS allows for comparatively fast growth as the intermediary liquid alloy phase can adsorb vapour far more readily to achieve supersaturation, resulting in crystal growth from nucleated seeds

at the liquid-solid interface. By controlling the nature and size of the liquid alloy, it is possible to have control over the physical characteristics of the nanostructures grown using this method.

Wagner and Ellis [109] observed gold tips at the ends of the silicon whiskers that they had prepared and found that a gold catalyst was necessary to initiate their growth. Their work has been further examined and refined, and VLS is now typically described as consisting of three stages:

- Formation of liquid alloy droplet at the desired point of growth
- Vapour phase of substance to be grown adsorbing to the liquid surface and diffusion across the droplet
- Supersaturation and nucleation at the solid-liquid interface resulting in crystal growth

The mechanism can be described in greater detail as follows.

A thin metal film is uniformly deposited over a substrate through a method such as sputter coating or thermal evaporation (Figure 2.14a). The coated substrate is then annealed at temperatures higher than the eutectic point of the alloy formed between the metal and the substrate to form droplets (Figure 2.14b). For gold and silicon, this temperature is approximately 363°C, substantially lower than the melting point for either gold ($\approx 1064^\circ\text{C}$) or silicon ($\approx 1414^\circ\text{C}$) [110]. The gold droplets have a radius determined as a function of the thickness of the metal film, annealing temperature, and interfacial tensions between the two components, as shown in Equation 2.7, where R_{min} is the minimum radius of the gold droplet, σ_{LV} is the liquid-vapour surface free energy, V_l is the molar volume of the liquid and s is the vapour phase supersaturation. Control over the density and dimensions of the nanostructures has been shown to be dependant on the deposited film thickness from which the particles form through a dewetting process [111].

$$R_{min} = \frac{2V_l}{RT \ln(s)} \sigma_{LV} \quad (2.7)$$

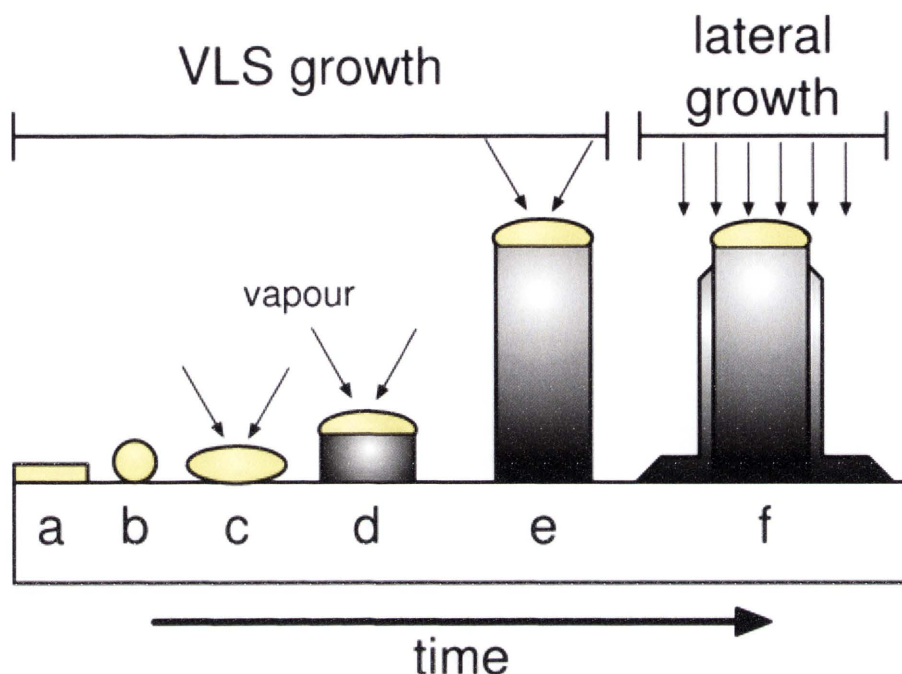


FIGURE 2.14: Schematic of VLS growth from nucleation to vertical growth. The Au film (a) melts to form Au droplets (b) which can then absorb Zn vapour to form a Zn-Au alloy (c). When this supersaturates, the Zn precipitates out at the interface between the alloy and the substrate to form ZnO (d). The growth continues vertically if conditions remain constant (e), however lateral growth can occur (f) where the vapour is absorbed directly by the sidewall of the nanostructure.

Alternately, it is possible to use lithographic techniques or colloidal dispersions to produce arrays of metal droplets over the substrate with well defined positions and size distributions [112].

The metal droplets act as seed particles which are enriched by adsorbing the vapour source material to a critical saturation level (Figure 2.14c). The adsorption and precipitation of the vapour phase (Figure 2.14d-f) is subject to considerable debate and is one of the key areas of discussion regarding the validity of VLS as a viable and controllable growth technique. There are three main models that are currently accepted as possible adsorption processes of the vapour phase as shown in Figure 2.15.

The first model indicates that the liquid alloy droplet initiates and guides the growth of the nanostructure by acting as a preferential site for adsorbing incoming atoms from the vapour phase. The growth begins after the droplet becomes supersaturated

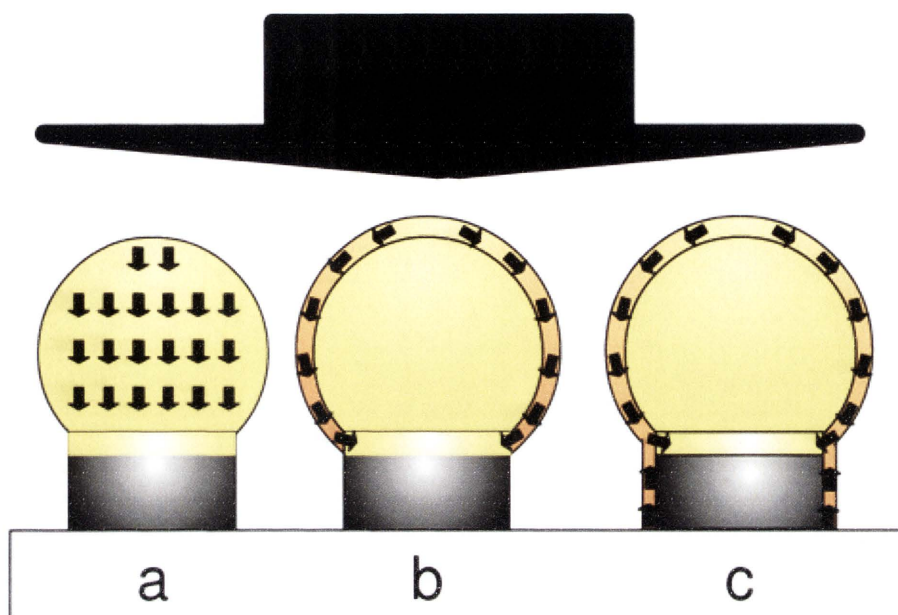


FIGURE 2.15: Three models proposed to explain VLS growth - a) Diffusion of vapour directly through gold droplet to the interface with the nanostructure. b) Diffusion of adsorbed atoms from the vapour phase over the surface of the gold droplet to the interface. c) Diffusion of vapour phase atoms from the surface of both the nanostructure and the droplet to the interface between the two.

with the growth material and the solid nanostructure is formed by precipitation from the droplet. The second model instead has atoms diffusing over the surface of the droplet to the interface between the solid substrate or nanostructure and the liquid alloy where they contribute to the nanostructure growth while the third model instead has the incoming atoms landing over the entirety of the droplet and already grown nanostructure, before then diffusing along the surface of the droplet and structure to the liquid-solid interface.

Regardless of the nature of the adsorption process, it is generally accepted that the crystalline growth in the region around the gold droplet is a result of the deposition of the growth material due to its higher melting point than that of the eutectic alloy. Vapour liquid solid has several advantages over other techniques. The introduction of a liquid intermediary phase results in a lowered reaction energy when compared to typical vapour-solid growth. The structures are grown only in areas of the substrate coated in the metal catalyst, allowing for large scale patterning of nano-arrays.

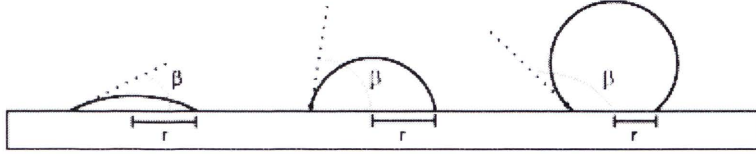


FIGURE 2.16: Schematic showing the effect of contact angle on the radius of the droplet. As contact angle β increases, the radius of the contact area between the droplet and the substrate r decreases for a droplet of a set radius.

Furthermore, the size and shape of the structures can be easily controlled by the nature of the catalysts enabling the fabrication of anisotropic arrays from a variety of materials.

Catalyst material requirements

As mentioned previously, there are several conditions that need to be met in order to consider using a particular material as a catalyst for VLS growth. Not surprisingly, the principle requirement is the formation of a liquid solution with the crystalline growth material of interest. Without this, there can be no saturation or diffusion across the catalyst droplet, resulting in no VLS growth. The catalyst also needs to have a low solubility with regards to the substrate in both its solid and liquid phases, and its vapour pressure needs to be such that the droplet does not vapourise or change in volume throughout the growth process. When reactive materials can be found in the growth process - as in CVD - it is preferential that the catalyst material remains chemically inert with the final nanostructure to produce high purity materials. The vapour-solid, vapour-liquid, and liquid-solid interfacial energies between the substrate and the catalyst contribute to the shape of the droplets and therefore must be examined carefully. Small contact angles between the droplet and substrate result in large area growth, while a larger contact angle will result in smaller formations, as shown in Figure 2.16. This relationship can be approximated using $r \propto 2\sqrt{\sin^2(45 - \frac{\beta}{4})}$.

2.9.2.3 Vapour-solid-solid

A further mechanism that has been proposed to explain the growth of ZnO nanostructures is that of vapour-solid-solid (VSS). In this process, a solid particle is utilised to act as the adsorption of the vapour phase, and ultimately the growth site of the nanostructure. There have been several reports suggesting that the catalytic particle remains in the solid phase for many different nanowire/catalyst systems such as GaAs/Au [113] or Si/TiSi₂ [114]. VSS differs from VS in that VS can only account for ZnO nanostructural growth under supersaturation conditions [115]. The presence of the solid catalyst particle on the substrate is required to provide a nucleation site for the Zn vapour. There are two ways in which a suitable solid particle can be produced - firstly through drop casting of ZnO powder suspensions over the substrate, or through the initial stages of VLS. If the substrate is initially covered in metal islands, such as Au, these droplets will act as preferential sites for Zn vapour incorporation, rapidly forming Au-Zn clusters [116]. The Zn concentration in these droplets increases over time, however the particles themselves remain solid. When the Zn concentration threshold is reached, nanostructural formation commences with the catalyst acting as a sink for Zn vapour, generating a concentration gradient across the catalyst particle. The diffusion of the Zn through the Au-Zn particle thus sets the upper limit for ZnO growth rates.

2.9.3 Summary of growth mechanisms

While each of the three proposed CVD based methods have been shown to produce nanostructures in a controlled manner, the most commonly used experimental method is that of VLS. The ability to control structural dimensions and locations of the nanostructures is desirable in the quest to produce large uniform arrays of aligned ZnO nanorods. The lower temperature requirement of VLS when compared to VS allows for more generalised growth equipment to be utilised, rather than the need to use high temperature furnaces and longer temperature ramping times. The

simplicity of the explanation as to the mechanisms involved in VLS when compared to VSS also suggest that it is a more likely growth process. As such, this work will utilise VLS as the process by which ZnO nanostructures will be produced.

Chapter 3

Experimental techniques

The majority of the experimental techniques that were used during the course of this work are well established. The methods can be found in standard textbooks and as such only the underlying principles are briefly discussed in this chapter. Where experimentally specific conditions are utilised, a more in depth outline is presented to familiarise the reader with the technique as it applies to this work.

In this work, ZnO samples were studied using a variety of techniques, investigating the morphological, electronic and optical properties. By utilising complementary techniques on individual samples consecutively, it is possible to elucidate a greater understanding of the findings.

The samples were produced or modified on site, except for when otherwise noted.

3.1 Preparation procedures

3.1.1 Cleaning and preparation of growth substrates

Two different substrates were used during the course of this work:

- Silicon wafer (001 orientation)
- a- ($11\bar{2}0$) and c- (0001) plane sapphire

The sapphire was supplied by MTI Corporation and polished on both planar faces. Substrates were cut to required sizes using a diamond pen. Substrates were cleaned in the following manner:

- 15 minute ultrasonic bath in acetone
- 15 minute ultrasonic bath in ethanol
- Deionised water rinse
- Nitrogen gas blow dry

Two materials were utilised as catalysts for growth. The first was a thin layer of gold as utilised in the majority of vapour-liquid-solid (VLS)-based ZnO growth [6, 87, 117–121], sputter coated over the substrate. This Au film forms liquid droplets when heated to temperatures above the melting point. The size distribution of the droplets can be modelled as a function of the film thickness, while the melting point of the gold is directly related to the droplet size [122]. This method was the predominant growth catalyst technique used throughout this work.

Extensive experimental investigation was undertaken in this work to determine the ideal thickness of the thin Au film to produce uniform droplet size distributions. Films of varying thicknesses were produced through sputter coating for different lengths of time. Film thickness uniformity was characterised by carrying out a series of image scans across scratches cut through the film using an atomic force microscope (AFM) tip scratch method described previously [123]. The films were annealed under a low pressure argon atmosphere (20 Torr) at temperatures ranging from 400 to 1000°C for 60 minutes before further AFM scans were performed. This temperature range was utilised to give an indication as to the possible size distributions of the droplets under potential growth conditions, while the low pressure

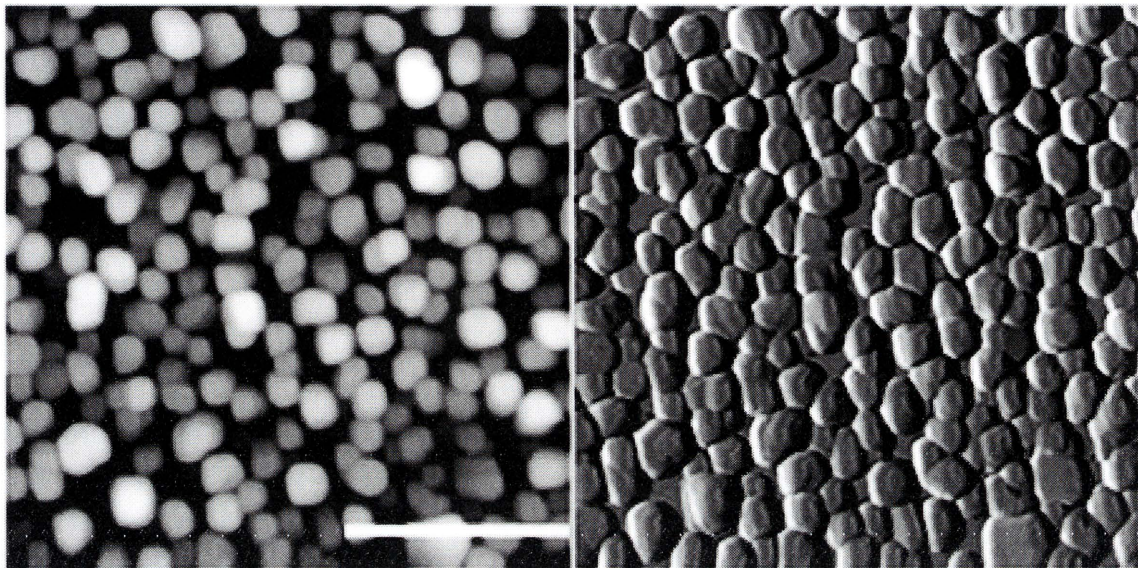


FIGURE 3.1: AFM scan of post-annealed gold film on silicon. Scale bar is $1\mu\text{m}$

environment was employed to minimise the likelihood of the films burning off at the higher temperatures. An example of an AFM scan of an annealed film can be seen in Figure 3.1.

The variation in annealing temperature showed minimal variation in the droplet distributions for the film thicknesses investigated at temperatures above the melting point of the gold film to 950°C . Above 950°C , the droplets exhibited reduced dimensions, possibly suggesting a loss in gold mass due to vaporisation.

The annealed film AFM scans were analysed using the software package ImageJ [124, 125], where near spherical droplets¹ were counted and their diameters were tabulated. The diameter distributions of the droplets were fitted to a normal distribution as shown in Figure 3.2. As a smaller diameter droplet along with a narrow size distribution is desirable, the chosen thickness for the gold film used in this work was 10 nm as this provided both of the required properties.

The second method utilised to produce a growth catalyst layer was drop casting of ZnO suspensions onto the substrate.

¹See Appendix A for determination of circularity

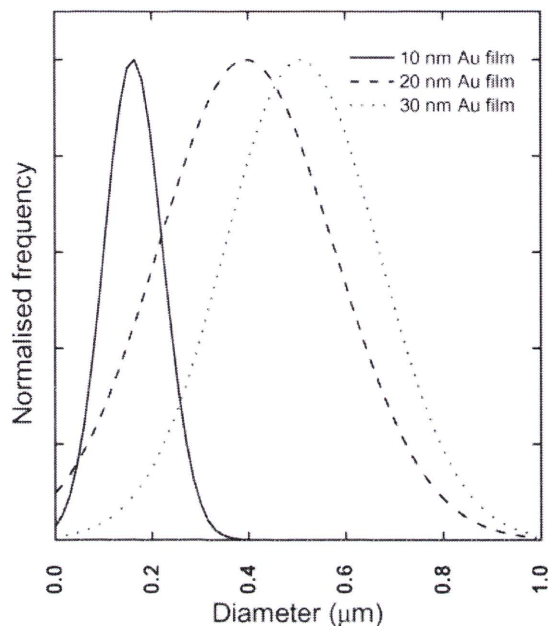


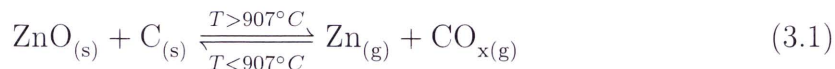
FIGURE 3.2: Distribution of gold droplet diameters produced through thermal annealing of sputter deposited gold films of different thicknesses on a silicon substrate. 10 nm thick Au film annealed at 950°C yields circular droplets with a mean diameter of approximately 150 nm.

A mass of ZnO powder (30 nm spheres provided by Inframat Advanced Materials) was dispersed in ethanol and ultrasonicated for approximately 15 minutes to break up the powder clumps, resulting in a suspension of nanospheres. This suspension was then drop cast using a micropipette onto a clean substrate. After the ethanol was completely evaporated, the particles were found to be relatively evenly distributed across the substrate, with minor aggregates occurring at the suspension-substrate-air interface. Different volumes of this suspension was then drop cast onto silicon to find the optimal parameters to produce the best dispersion over the substrate. The ideal dispersion of the ZnO seeds occurred when 0.1 grams of powder were mixed with 2 mL of ethanol, with 50 μL pipetted onto the substrate and left to dry.

3.1.2 Carbothermal reduction of ZnO

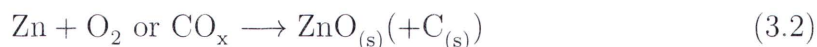
Zn vapour was produced through the carbothermal reduction of ZnO powder. ZnO has a melting point of 1875°C, but the addition of graphite can lower this to 907°C

[126]. This can be represented through Equation 3.1 where x is $= 2$ or less, giving carbon dioxide, monoxide or suboxide as possible products of the reaction.



The Zn vapour is then able to travel downstream from the source, assisted by the carrier gas, to a lower temperature zone.

A gold thin film can be used as a catalyst to initiate ZnO nanowires growth on the substrate. The gold forms a eutectic alloy with the substrate at temperatures well below the melting point of gold - for gold on silicon this temperature is 363°C . When the substrate reaches this eutectic temperature, the gold film melts and disperses into isolated liquid islands of relatively uniform size (see Figure 3.1 on page 46). The Zn vapour is adsorbed by the gold droplets, forming a Zn-Au alloy. When the droplet becomes supersaturated, the Zn begins to precipitate out at the interface of the droplet and the substrate. The Zn is then oxidised by the residual oxygen or carbon oxides to form ZnO [127] as shown in Equation 3.2.



The supersaturation of the droplets and formation of the ZnO solid will only occur at temperatures below 907°C , otherwise the newly formed solid could be reduced to Zn vapour again in the presence of C. The growth process continues to occur until either the source material is exhausted or if the temperature of the substrates is reduced to a level where the alloy solidifies.

3.1.3 Furnace setup

A computer controlled three-zone split furnace was used in the course of this work, as shown in Figure 3.3. Gas flow rates (measured in standard cubic centimetres per

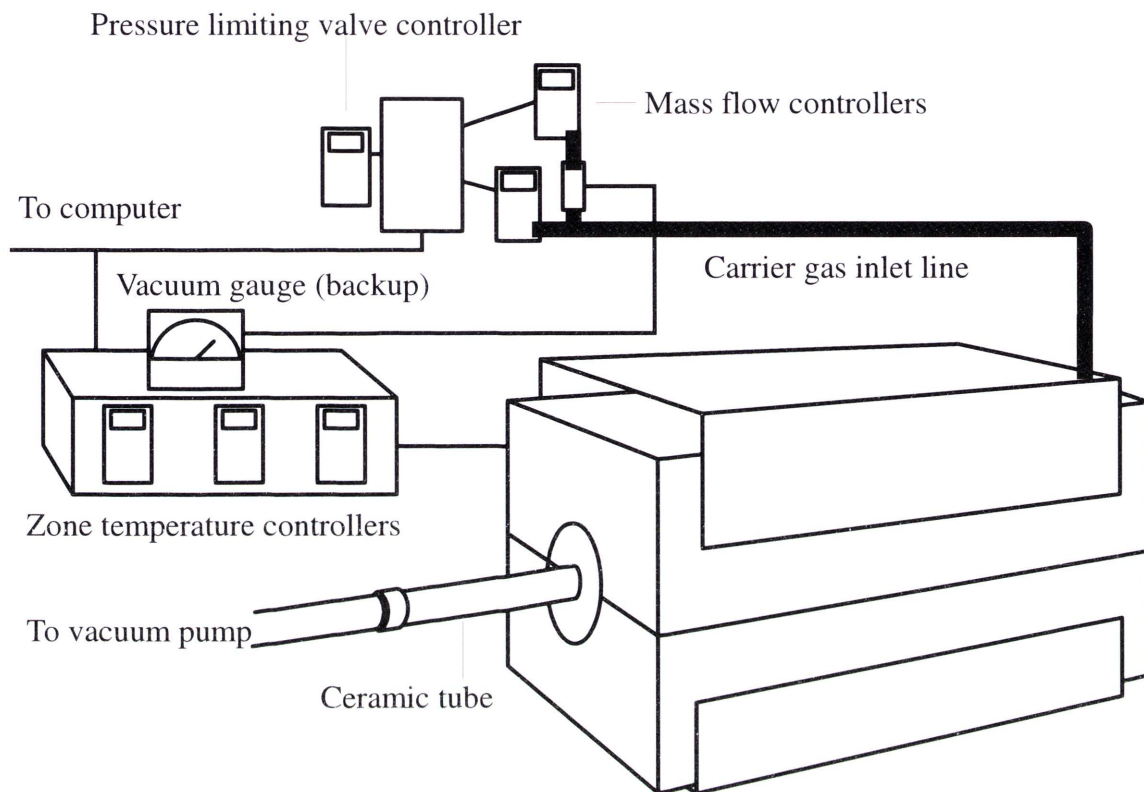


FIGURE 3.3: External view of three zone split furnace indicating important components

minute (sccm)) were controlled by mass flow controllers while the pressure was monitored and managed through a pressure limiting valve. The gas, pressure and zone temperatures were all controlled and recorded via a custom LabView application.

Within the ceramic tube, the source material is typically placed with the source at a higher temperature upstream from the substrate, creating a temperature gradient as seen in the internal schematic in Figure 3.4. The separation of the source and substrate can vary between 50 cm, where the substrate is at the end of the tube, and effectively 0 cm, where the substrate is almost touching the source.

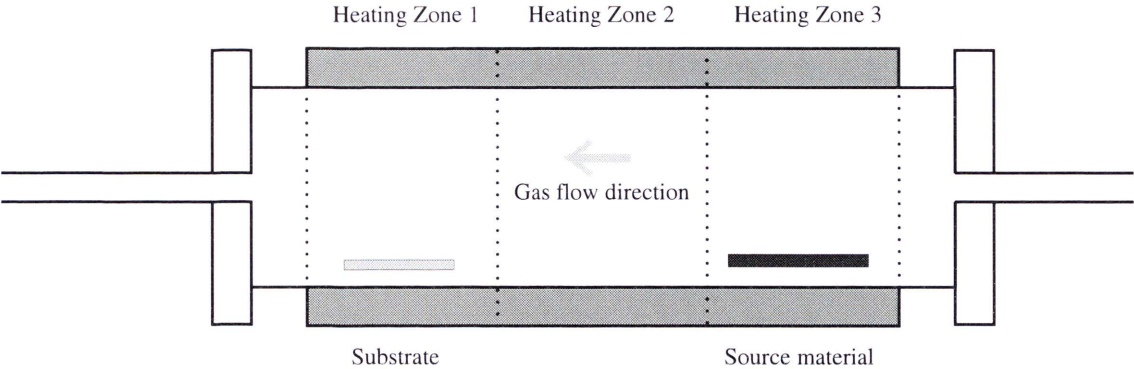


FIGURE 3.4: Schematic of internal components of growth furnace

TABLE 3.1: Parameter ranges for furnace growth

Parameter	Possible values
Pressure (end of ceramic tube)	0-750 Torr
Substrate temperature	400-900°C
Source temperature	900-950°C
Gas flow rate	0-1000 sccm (Argon) 0-200 sccm (Oxygen)

3.1.4 Parameter ranges

In the furnace, there are a variety of parameters available for adjustment. Each parameter has a range of values, and it is the systematic evaluation of each combination that yields a reproducible growth recipe. It should also be noted that varying the relative position of the substrate to the source material will yield different samples.

Extensive experimental investigation was undertaken to identify the optimal parameter range within which successful growth would occur (see Section 4.2.2 on page 77). Source temperatures were limited to above 900°C to ensure carbothermal reduction would occur, while substrates were kept above the eutectic temperature to make sure that liquid alloys would be present for Zn vapour adsorption.

The most successful conditions for the experimental growth set up used in this work were found to be:

- Pressure 10 Torr
- Source temperature 950°C
- Substrate temperature 500°C
- Gas flow - oxygen 15 sccm
- Gas flow - argon 15 sccm
- Growth time 60 minutes

3.1.4.1 Preparation of transition metal doped ZnO through in-diffusion

Thermal in-diffusion is a process commonly used in the semiconductor industry and a significant number of studies have occurred involving doped silicon and germanium [128–130] as well as ZnO [131, 132]. Crystal quality of diffusion doped ZnO [131] indicate that the process is suitable for dopant incorporation with the majority of dopants occupying host lattice sites. Furthermore, there is minimal formation of precipitates or secondary phase regions. Diffusion doping is achieved by coating a ZnO crystal with a transition metal before driving the metal into the material by high-temperature in-diffusion under controlled conditions. The following methodology was developed in this work and was performed to produce manganese (Mn) doped ZnO crystals.

- ZnO crystals (1 cm x 1 cm x 0.5 mm, polished on both faces as provided by MTI Corporation) were cut to 5 mm x 5 mm squares
- ZnO crystal squares were cleaned ultrasonically for 10 minutes in an acetone bath, then 5 minutes in an ethanol wash, rinsed with deionised water and dried with high purity nitrogen gas
- Cleaned squares were coated on one side with a 50 nm thick layer of the transition metal using an evaporative coater
- Individual coated squares were sealed in glass ampoules under vacuum following multiple argon purges to remove trace gases

- The ampoules were heated to 700-900°C (depending on the transition metal) for up to 40 hours
- The in-diffused samples were kept under vacuum while not being studied to reduce cross contamination

The concept behind in-diffusion is that the transition metal (TM) ions will diffuse from the thin coating at the surface into the bulk, entering into the crystal lattice. The diffusivity rate of a metal into ZnO, D , can be approximated by

$$D = D_0 \exp^{-\frac{E}{k_B T}} \quad (3.3)$$

where E is the activation energy in eV and D_0 is the diffusion coefficient for the metal. For Mn, $D_0 = 3.2 \times 10^{-3}$, $E = 2.87$ eV [133]. At 700°C, this results in a diffusion rate of $\approx 4.4 \times 10^{-4} \text{ nm}^2 \text{ s}^{-1}$. After 40 hours of annealing, the maximum Mn incorporation depth would be expected to be ≈ 63 nm, assuming that the diffusion is not limited by any external factors.

Furthermore, it is necessary to consider the likelihood of the metal film evaporating from the surface of the ZnO rather than diffusing into the crystal. To counteract this, the annealing temperature needs to be kept as low as possible. This reduces the rate of diffusion, and thus a trade-off between speed and successful diffusion is required.

3.2 Characterisation techniques

There are several complementary techniques that can be used to investigate the properties of ZnO. These can be divided into three subgroups depending on the method of generating signal - electron generated, photon generated, physical interaction.

3.2.1 Scanning electron microscopy

Scanning electron microscope (SEM) is a widely utilised surface analysis technique that can produce high resolution images of sample surfaces. It is typically utilised for morphological analysis of materials, but can also be used to determine the material composition using x-ray microanalysis. In a typical SEM (see Figure 3.5 for labelled parts), electrons are emitted from the cathode and accelerated towards the anode with energy ranging from 200-30,000 eV. The electron beam is focused by condenser and objective lenses, forming a small beam with a diameter on the order of nanometres. This beam passes through scanning coils which deflects the beam in a raster pattern over an area of the sample surface.

These primary electrons hit the surface and undergo a variety of scattering processes, depending on the material and the energy of the electron. In general, the interaction of high energy electrons ($> \text{keV}$) with matter leads to different processes including secondary, backscattered or Auger electrons, X-rays or cathodoluminescence, as shown in Figure 3.6. Each process can contain important information about the nature of the material, for example secondary electrons show the morphology and topography of the material surfaces, while backscattered electrons can detect contrast in areas with differing chemical compositions.

The different emission processes are detected through different methods. Secondary electrons are collected by an Everhart-Thornley detector which actively attracts the electrons and accelerates them towards a positively biased scintillator. When the electrons hit the phosphor, they produce flashes of light (through cathodoluminescence) that is collected by a photomultiplier. The ‘brightness’ of the signal depends on the number of electrons arriving at the detector. As the likelihood of a secondary electron escaping a sample increases at edges or steep surfaces, this gives images a three-dimensional appearance.

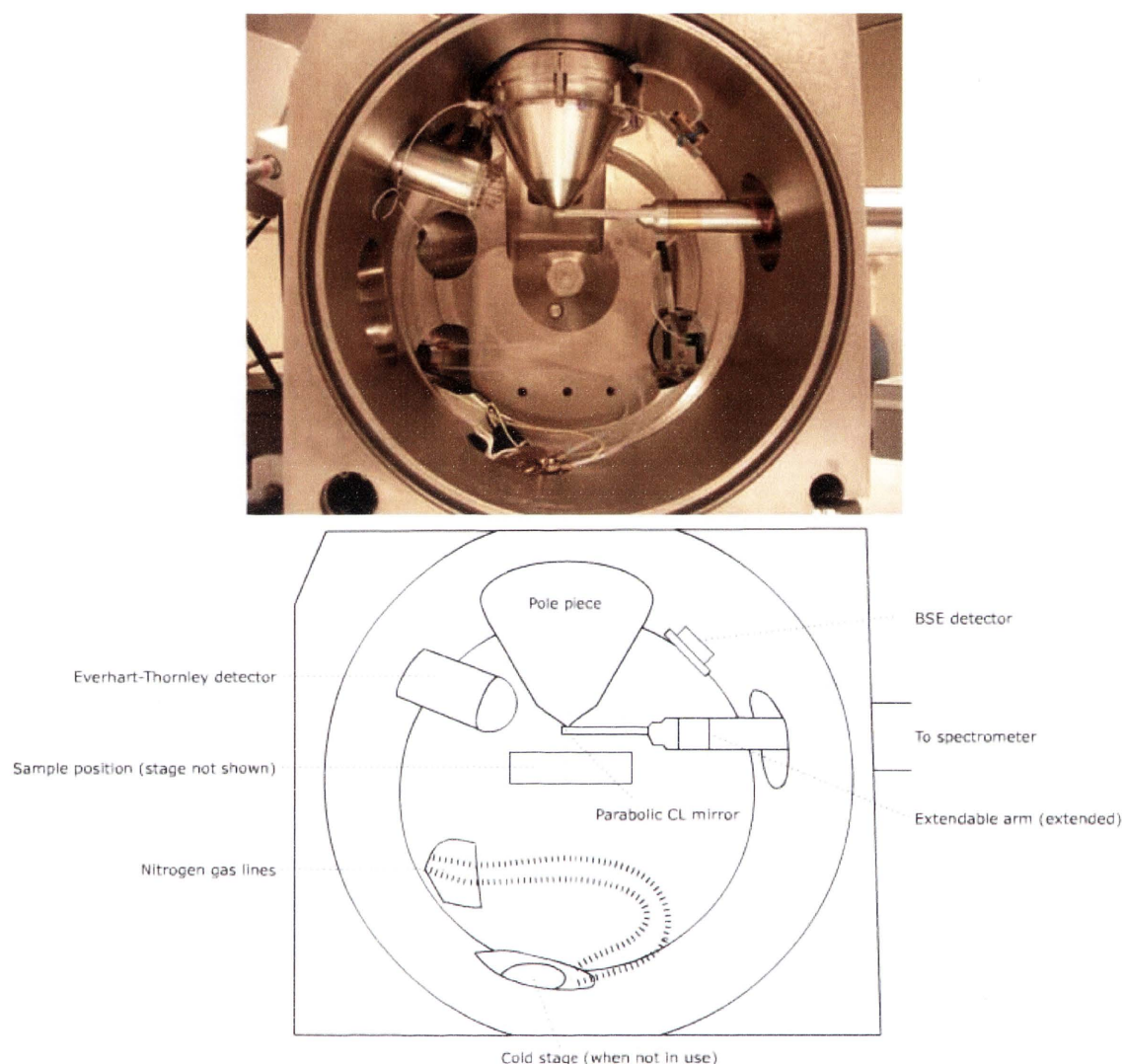


FIGURE 3.5: Quanta 200 SEM system used in this work with key components identified

For backscattered electrons, the Everhart-Thornley detector is inefficient as a detection method as a small number of backscattered electrons are emitted within the solid angle of the detector, and the attraction of the positive bias has little influence on the higher energy electrons. Typical backscattered electron detectors are positioned above the sample in a ring around the electron beam, thus maximising the solid angle for collection.

Cathodoluminescence is collected either through a fibre optic cable situated near the sample, or through a parabolic mirror situated directly over the sample in line

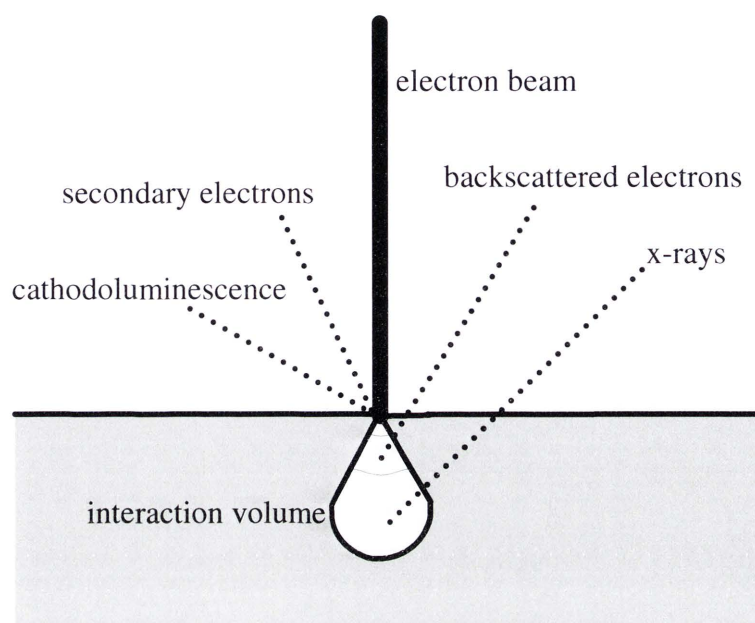


FIGURE 3.6: Schematic diagram of processes induced by electron bombardment

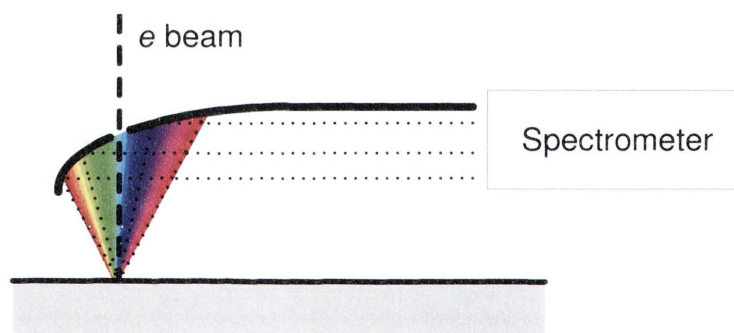


FIGURE 3.7: Collection of CL light through parabolic mirror

with the electron beam (Figure 3.7). The mirror has a small hole through which the beam is able to pass, generating light in the sample which is then collected from a significantly greater solid angle than that of a fibre. The light is transported to a spectrometer for analysis. The following section will focus on cathodoluminescence (CL) and its variants in terms of its use within the scope of this work.

3.2.1.1 Cathodoluminescence

Cathodoluminescence is the light emitted by materials as a result of electron bombardment and the subsequent generation and recombination of electron-hole pairs.

It is a powerful investigative tool that can examine the optical properties of materials in a non-invasive manner. CL can obtain resolution below that of the diffraction limit of light. The technique can be used to characterise the composition and defects of a material [134], and when this is coupled with the high resolution imaging the technique becomes an ideal tool to examine nanostructured materials such as nanorods or nanowires [135].

The spatial resolution of CL is strongly determined by the interaction volume of the electrons incident on the material. In this volume, the electron undergo a series of elastic and inelastic scattering events, which can result in electron-hole pair generation leading to cathodoluminescence. The penetration depth for an electron can be approximated by using the Kanaya and Okayama equation [136]:

$$R_e(\mu m) = \frac{0.0276AE_b^{1.67}}{\rho Z_e^{0.889}} \quad (3.4)$$

where E_b is the accelerating voltage of the electron beam in keV, A is the atomic weight of the material in gmol^{-1} , ρ is the material density in gcm^{-3} and Z_e is the effective atomic number. Z_e can be calculated by using a weighted average of the atomic numbers of the constituent atoms such as

$$\begin{aligned} Z_e &= \frac{A_{Zn}}{A_{ZnO}} \times Z_{Zn} + \frac{A_O}{A_{ZnO}} \times Z_O \\ &= \frac{65.38}{81.39} \times 30 + \frac{16.01}{81.39} \times 8 \\ &= 25.67 \end{aligned} \quad (3.5)$$

For ZnO, the penetration depth can be estimated from Figure 3.8. The generation of electron-hole pairs by electrons is different from that by photons. A photon is only able to produce a single electron-hole pair, while an electron is able to generate thousands within the generation volume (see Equation 3.6). The creation of a single electron-hole pair requires energy approximately equal to three times the band gap, independant of the incident electron energy. The local generation rate of the

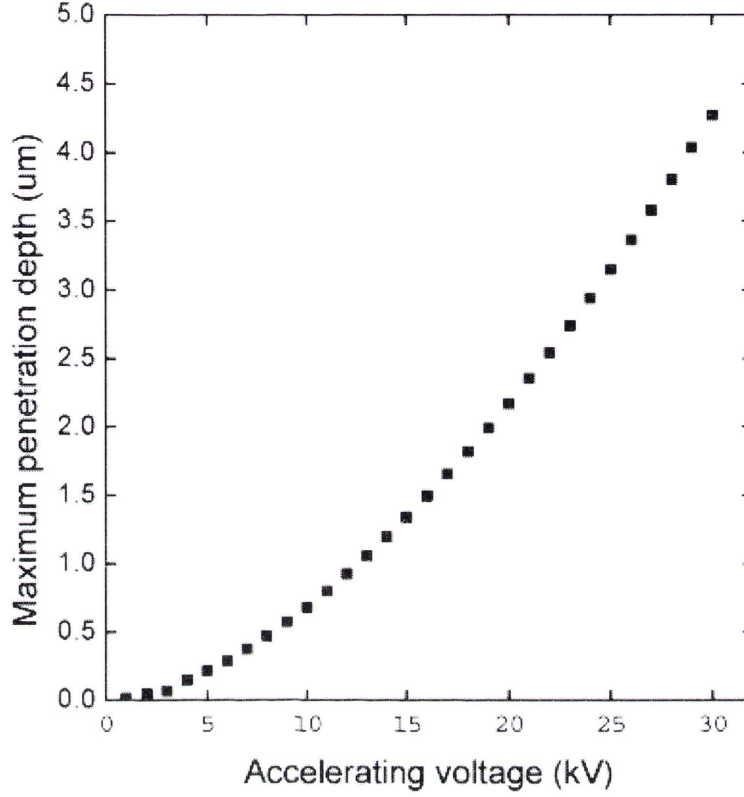


FIGURE 3.8: Maximum penetration depth of incident electron in ZnO versus accelerating voltage as determined by Equation 3.4

electron-hole pairs can be calculated from

$$G = \frac{E_b I_b Q (1 - \gamma)}{e E_g} \quad (3.6)$$

where I_b is the beam current, e is the charge on an electron, γ is the backscatter coefficient of the material, E_g is the band gap energy and Q is the quantum efficiency for electron-hole pair generation.

3.2.1.2 Depth resolved cathodoluminescence

As the accelerating voltage of the electron beam determines the penetration depth of the CL probing (as per Figure 3.8), it is possible to generate electron hole pairs at varying depths below the surface of the sample. Increasing the accelerating voltage

will produce a larger interaction volume; however it is necessary to reduce the beam current so as to maintain a constant power and hence the number of electron-hole pairs across sampling region. This is often referred to by the approximation

$$[n]_{eh} \propto I_B \cdot E_b \quad (3.7)$$

By probing deeper into the sample, it is possible to give insight into the nature of the electronic structure of the bulk as a direct comparison to that of the surface. The maximum depth from which data can be obtained is limited by the instrumental parameters and the material under investigation as per Equation 3.4, as well as the influence of self absorption of the emitted light at depths within the crystal. The self absorption effect can be observed in Figure 3.9, where the intensity of the NBE emission increases in a near-linear fashion up to 15 kV accelerating voltage (or a depth of approximately $0.7\mu\text{m}$), at which point the CL response begins to level off. Conversely, the DL emission continues to increase relatively linearly regardless of accelerating voltage, and thus penetration depth.

3.2.1.3 Power density cathodoluminescence

Power density measurements maintain a constant penetration depth and vary the beam power. By increasing the beam current, a greater number of electron-hole pairs are generated as per Equation 3.7, and it is possible to draw conclusions about the nature and origin of the observed CL. Typical deep level transitions have a relaxation time of the order of μs to ms , while exciton or band to band transitions are of the order of ps to ns .

By plotting the log of CL intensity versus the log of beam current, it is expected that the different emission peaks will show linear relationships owing to the relationship $I_{\text{CL}} \propto I_B^m$, or $\log(I_{\text{CL}}) \propto m\log(I_B)$ [137, 138]. The slope of the linear fit applicable to each of the emissions is able to give indications as to the recombination rates.

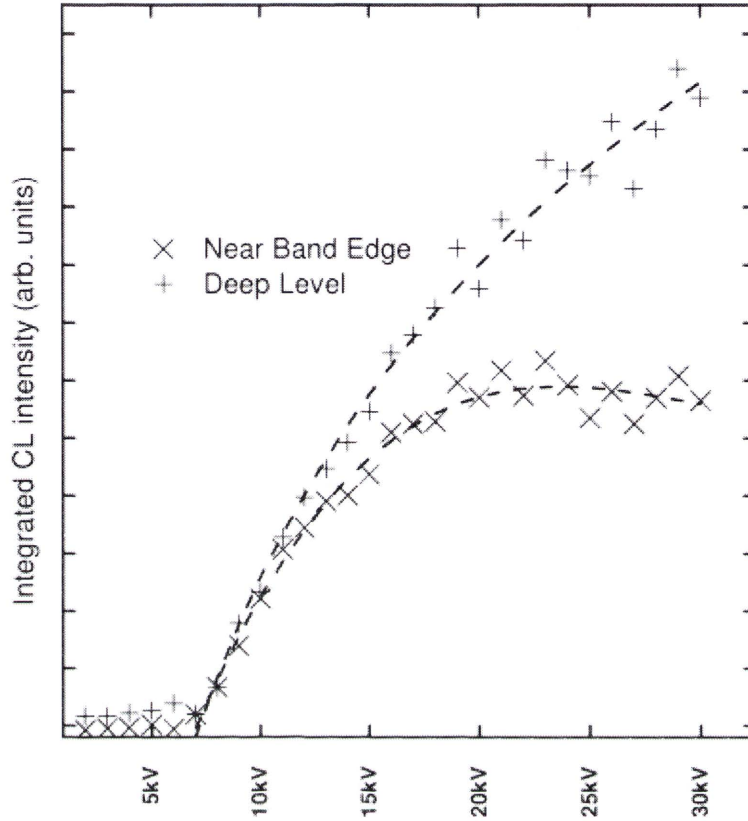


FIGURE 3.9: Example of depth resolved CL of a ZnO crystal. There is a minimum excitation depth required prior to generation of light as a result of a 'dead layer' present near the surface of the crystal. This dead layer is typically due to physical defects introduced during the polishing process. Electron beam power was maintained at 10 μ w, magnification at 8,000 \times .

For fast recombinations, such as direct band-to-band emission, the value for m is expected to be ≥ 1 [139], while defect related recombinations tend to have $m < 1$ [85, 140]. Figure 3.10 shows the difference between the UV and green emissions observed in ZnO crystals. Both slopes show a linear response on a log-log scale, with the NBE emission having a greater slope or m value. This indicates that the UV luminescence is due to transitions with fast relaxation times, such as excitonic or band to band, while the green is due to slower transitions such as deep level defects, agreeing with the assignments of the near band-edge (NBE) to the UV and deep level emission (DLE) to the green emissions.

Furthermore, if the incident electron beam power is producing e-h pairs faster than the recombination rate, the emission channel may show saturation effects, exhibiting

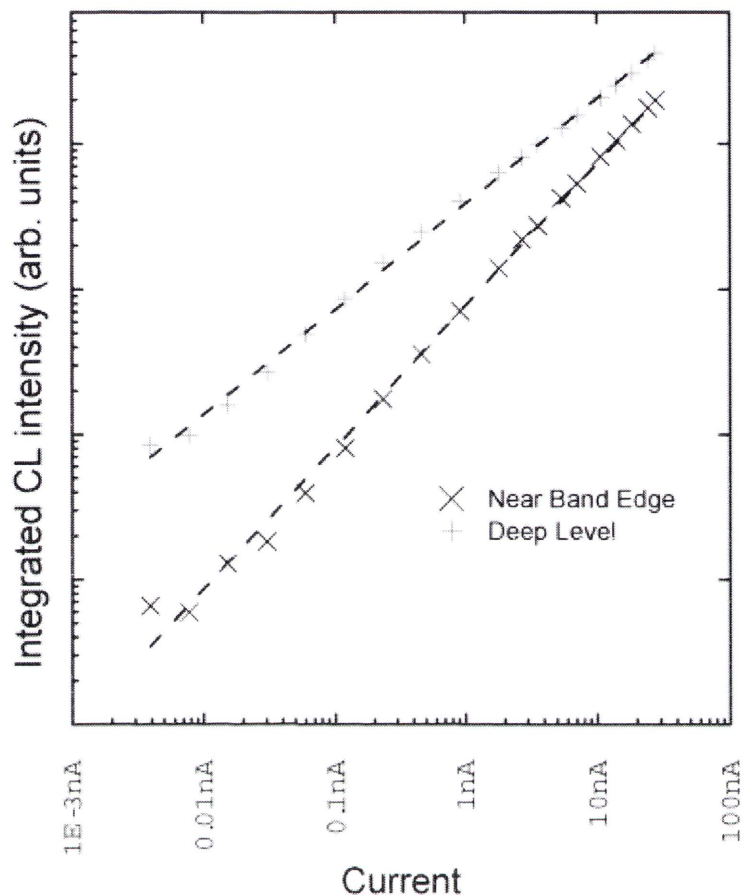


FIGURE 3.10: Power density CL of ZnO crystal at room temperature. Accelerating voltage = 30 kV. The difference in slope between the NBE and DLE emission is indicative of the rate of relaxation

a non-linear response at greater currents.

3.2.2 Photoluminescence

In photoluminescence (PL), instead of using electrons as the excitation source a high intensity laser is used. The photons from the laser will excite electrons from the valence to the conduction band, forming holes for later recombination. Once again, following recombination, any emitted photons are then guided through a monochromator via a series of lenses and collected by a photomultiplier tube.

3.2.3 Monte Carlo simulation

The penetration depth of an electron, and thus the resulting electron-hole pair generation, is a function of several variables as previously mentioned in Equation 3.4. This is only an approximation of maximum electron penetration depth however, and it is often useful to consider the overall interaction volume of the electrons within the material. One method that can be employed to determine the interaction volume in a solid is the Monte Carlo simulation code CASINO (monte CARlo SIMulation of electroN trajectory in sOlids) [141]. It is a single scattering Monte Carlo simulation that has been specifically developed for low energy electron beam interactions (0.1 to 30 KeV) and can generate a variety of signals commonly found during SEM operation. By appropriately designing the simulation parameters, it is possible to theoretically predict the signals that would be produced in a given sample.

CASINO is able to predict the interaction volume for both bulk and layered materials (in two dimensions), with typical results appearing as shown in Figure 3.11. Furthermore, the software is also able to take carrier diffusion into account, changing the interaction volume considerably at low accelerating voltages². For ZnO, with a minority carrier diffusion length of 60 nm[142], this changes the interaction volume from Figure 3.12(a) to Figures 3.12(c)-3.12(d). This change in the interaction volume is of considerable interest when investigating nanoscale material as the surface to bulk ratio of the probed region can vary dramatically from the predicted values depending on the accelerating voltages used. The initial electron injection and interaction volume (Figure 3.12(a)) shows the electron distribution as a teardrop, with the majority (90%) of the energy being deposited within 16 nm of the surface. The application of diffusion increases the 90% electron energy loss depths to between 30 and 35 nm for different surface recombination assumptions. The generally CL generation depth is taken as the depth at which the energy loss has resulted in 75% of the CL signal being generated.

²At higher voltages, the diffusion length of the carriers relative to the interaction volume dimensions becomes insignificant

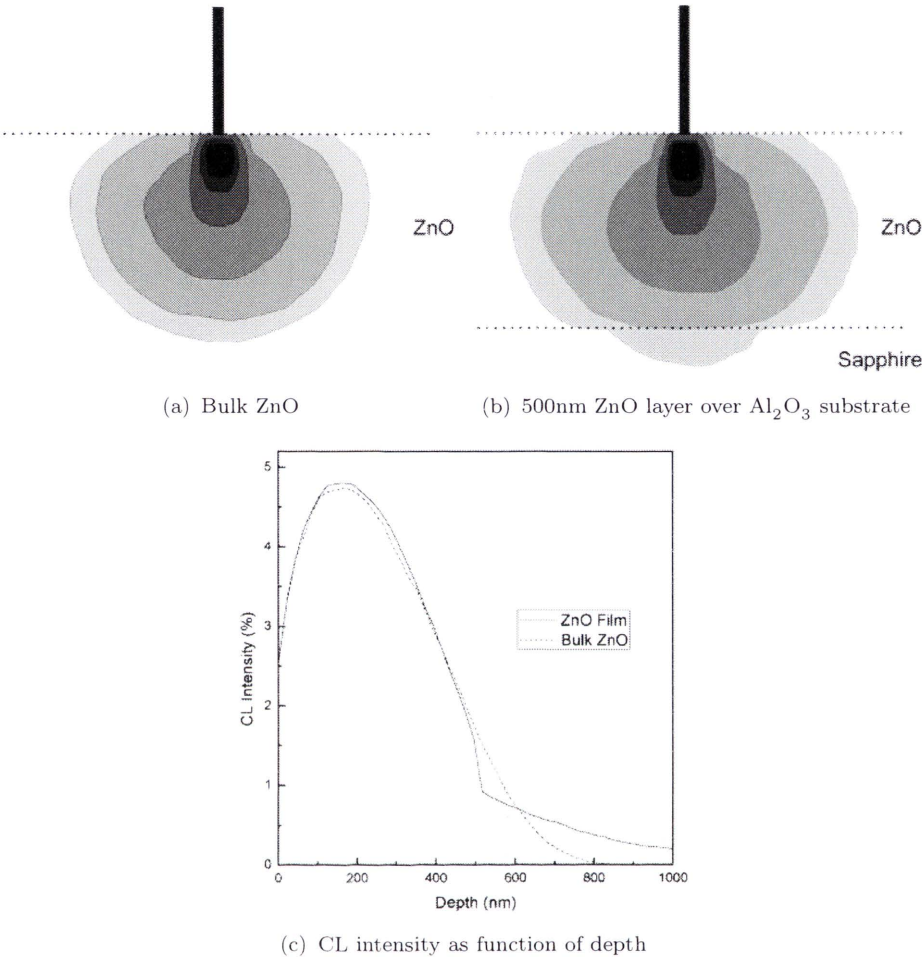


FIGURE 3.11: CASINO simulated electron interaction for bulk and thin film ZnO. Beam energy was fixed at 10 kV with 50,000 electrons simulated.

For experiments where information regarding approximate electron penetration depth (and thus CL generation depth) in ZnO is required, the parameters found in Table 3.2 were utilised. The results of these simulations were used to generate the plot in Figure 3.13, linking the accelerating voltage with an approximate CL generation depth.

3.2.4 Synchrotron light techniques

In order to allow for core level interaction in atoms, high energy x-rays need to be used. Synchrotron radiation provides x-rays several orders of magnitude greater

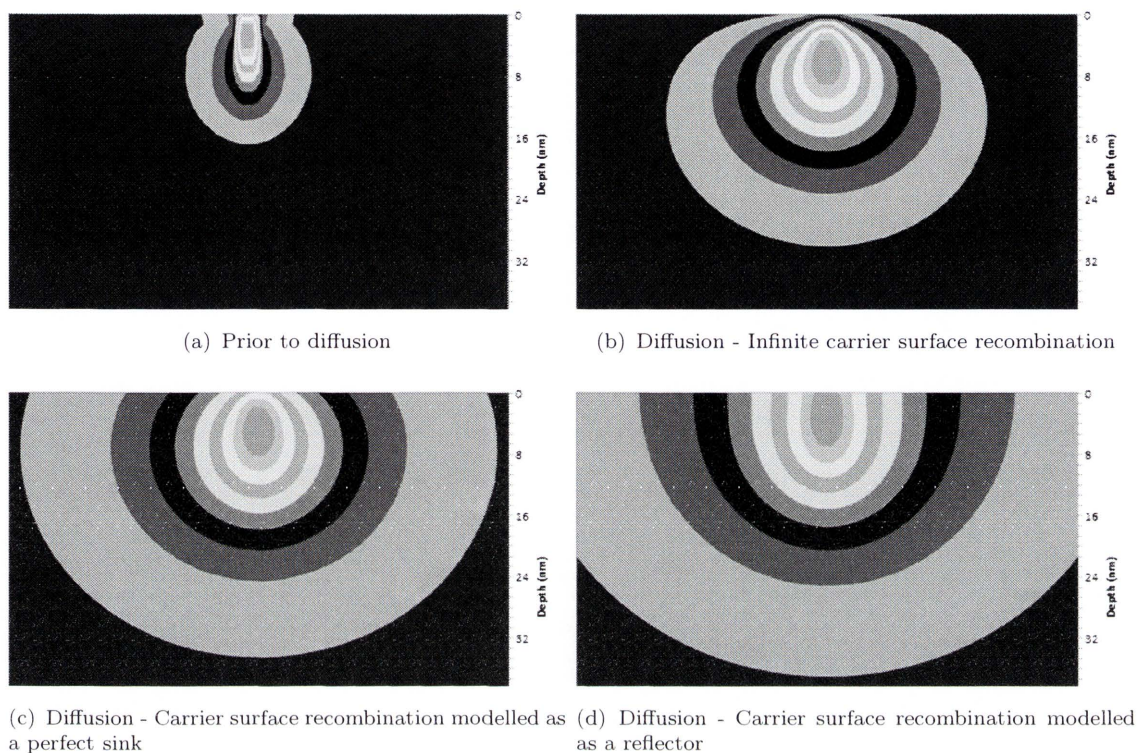


FIGURE 3.12: An example of the impact of different carrier diffusion models on the interaction volume in bulk ZnO. Beam energy was 1 kV, 500,000 electrons. Each grey band represents a 10% drop in electron energy distribution.

TABLE 3.2: CASINO simulation parameters for depth approximations

Parameter	Setting
Sample	ZnO substrate
Density	3.99838
Weight fraction	0.803397:0.196603
Accelerating Voltages	1-30 kV (1 kV stepsize)
Number of simulated electrons	50,000
Beam radius	1 nm
Total Cross Section	Mott by Interpolation
Partial Cross Section	Mott by Interpolation
Effective Section Ionization	Casnati
Ionisation Potential	Joy & Luo [1989]
Random Number Generator	Press et al. [1986]
Directing Cosin	Soum et al. [1979]
dE/dS Calculation	Joy & Luo [1989]

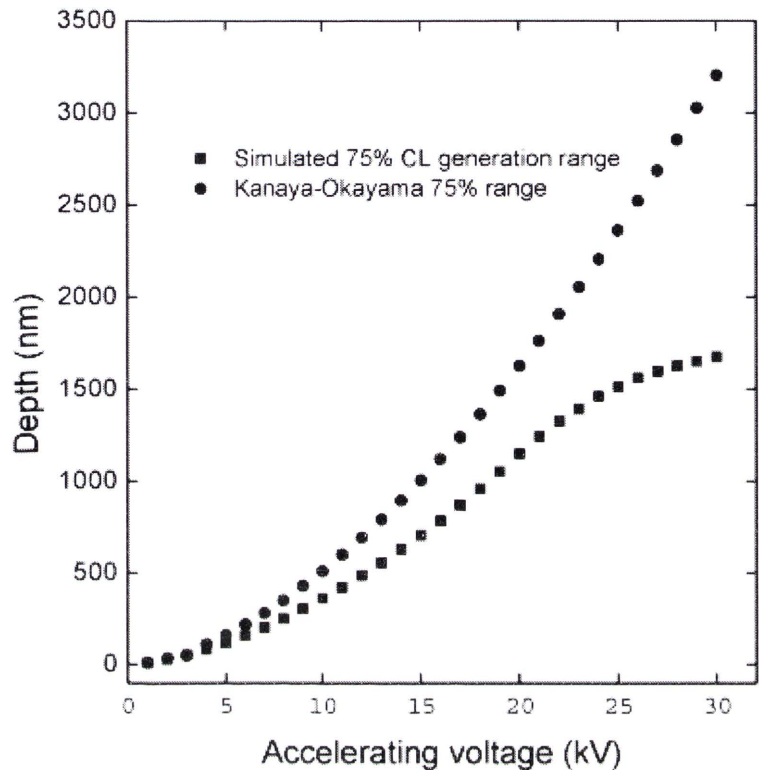


FIGURE 3.13: Accelerating voltage versus CL generation depth from Monte Carlo simulations compared to the expected penetration depth of the incident electrons from the Kanaya-Okayama equation. The KO range follows a power law relationship, while the CL generation range is more complex, highlighting the necessity of simulation to accurately interpret depth resolved CL.

than conventional sources (10^{5-6} times greater), along with the ability to tune the source. There are several techniques that can be utilised through the application of a synchrotron light source (SLS). The use of high intensity photons - with wavelengths ranging from the ultraviolet through to x-ray energies - induces a photoelectric response in a sample. This results in the emission of photoelectrons that have characteristics dependant on their original electronic states.

3.2.4.1 Angle resolved

Angle resolved photoemission spectroscopy (ARPES) is a synchrotron technique that is one of the most direct methods to study the electronic structure of solid surfaces. The SLS is directed at the sample at varying angles, inducing electron

emission near the surface, typically within a few nanometres. The collected electron return detailed information on the band structure and electron distribution within the solid.

3.2.4.2 X-ray absorption near edge structure

X-ray absorption near edge structure (XANES) is an analysis technique that measures the absorption of x-rays as a function of their energy. The absorption coefficient shows an oscillatory structure, extending over hundreds of electron volts beyond the absorption edge. This oscillation - the x-ray absorption fine structure - arises due to the wave-like photoelectrons. The part of the photoelectron scattering back from neighbouring atoms interferes with the part of the photoelectron being emitted. In the region where XANES is utilised, the elastic mean free path is long and the electron scattering factor typically quite large.

3.2.5 X-ray diffraction

X-ray diffractometry (XRD) is a highly versatile, non-destructive analysis technique that can be used for the qualitative and quantitative analysis of crystalline materials. It has been used to determine the lattice constants and overall structure of bulk solids, to identify unknown materials, and the investigate stress or strain in materials. In this study a Siemens D5000 X-ray diffractometer was used with a Cu-K α x-ray tube ($\lambda=1.54056\text{\AA}$), operating in $\theta - 2\theta$ mode.

As the atoms in a crystal are arranged periodically in a lattice, x-rays scattered from a crystalline solid can constructively interfere, producing diffraction patterns. In 1912, Bragg found what is now referred to as Bragg's Law, linking the angle of incidence to the planar spacing in the crystal,

$$n\lambda = 2d\sin\theta \tag{3.8}$$

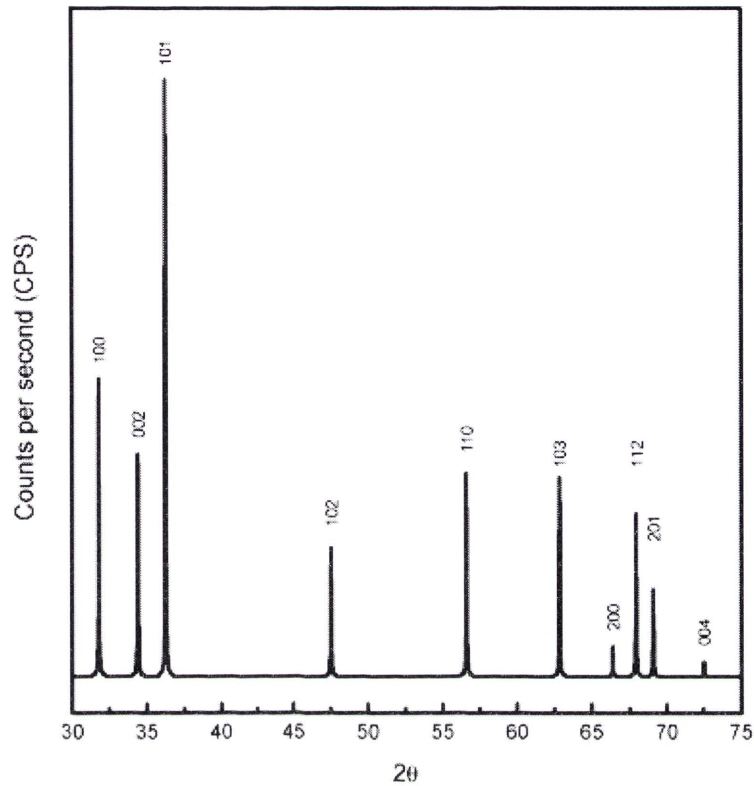


FIGURE 3.14: Generated XRD plot of ZnO powder with diffraction peaks identified. The relative peak areas are indicative of the number of planes contributing to each reflection. This diffractogram represents powdered ZnO with all planes contributing to the plot.

where λ is the wavelength of the incident x-ray beam (1.54056 \AA in this case), d is the interplanar spacing, θ is the incident angle of the beam, and n is an integer.

Through mathematical manipulation³, it is possible to correlate Bragg’s Law with Miller indices for an hexagonal system, and it is possible to identify peak positions in a diffractogram such as Figure 3.14. By comparing diffractograms for different samples, and observing variations in the θ peak values obtained, it is possible to determine changes in the lattice parameters within the crystal. These changes indicate a change in the composition of the material as a result of a defect or doping.

³Refer to Appendix B

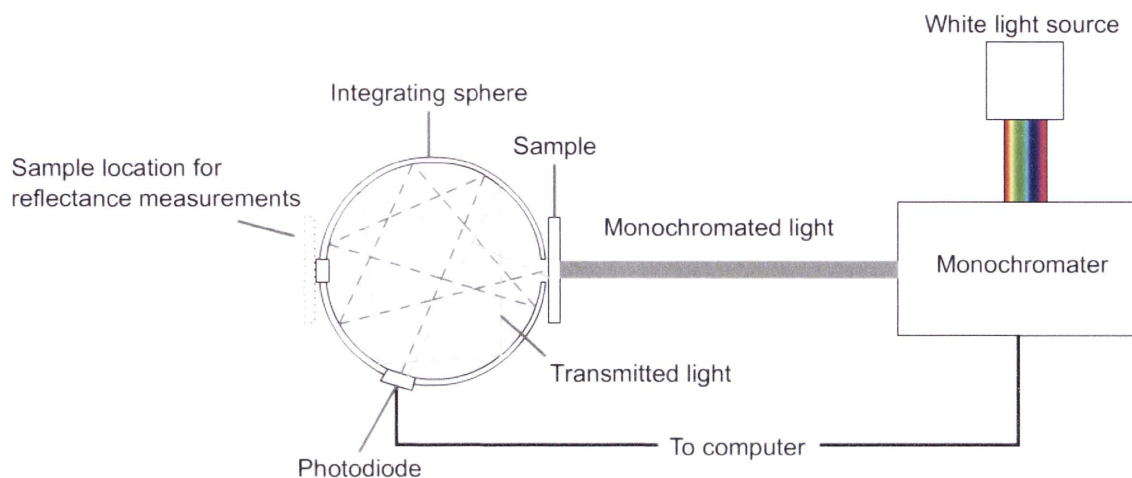


FIGURE 3.15: Simplified schematic showing the key components involved in UV-Vis spectroscopy

3.2.6 Ultraviolet-visible spectroscopy

Ultraviolet-visible spectroscopy (UV-Vis) is a spectroscopic technique utilised to determine absorbance and reflectance of a material in the UV and visible regions of the spectrum. A spectrometer measures the intensity of light alternately passing through and reflecting from a material and compares it to a reference material. In this work, a single beam Perkin-Elmer UV-Vis spectrophotometer with an integrating sphere was used to determine the transmittance and reflectance of the various samples. A schematic of the setup can be seen in Figure 3.15.

A white light source is passed through an Oriel Cornerstone 260 1/4 m monochromator to produce a monochromated light beam. For transmittance measurements, this beam is then passed through the sample into then integrating sphere with a highly reflective interior, after which the transmitted light is eventually collected by a photodiode. For reflectance measurements, the sample is located on the opposite side of the sphere. The absorbance, reflectance and transmittance of a sample are linked to each other as $\text{Absorbance}(\%) = 100\% - \text{Transmittance}(\%) - \text{Reflectance}(\%)$.

The optical absorption coefficient (α) can be calculated from the transmission spectra using the relationship

$$\alpha = -\frac{1}{d}\ln(T) \quad (3.9)$$

where d is the thickness of the ZnO powder layer and T is the transmittance.

For direct band gap semiconductors, the optical band gap can then be evaluated from the equation

$$(\alpha h\nu)^2 = A(h\nu - E_g) \quad (3.10)$$

where A is a constant, $h\nu$ the photon energy, and E_g is the band gap [143].

The band gap energy of a material can be derived from a UV-Vis spectral plot of $(\alpha(\lambda)h\nu)^2$ versus $h\nu$, where $\alpha(\lambda)$ is the wavelength dependant absorption coefficient and $h\nu$ is the photon energy [143]. If $(\alpha h\nu)^2$ is plotted as a function of photon energy $h\nu$, the energy gap can be estimated from the intercept of linear part of the curve with the x-axis.

For indirect semiconductors, a plot of $(\alpha h\nu)^{\frac{1}{2}}$ against $h\nu$ will also yield a linear section that can be extrapolated to find the band gap.

Samples of ZnO powder were prepared in the following manner for UV-Vis investigation.

- 0.1 gram of powder was dispersed in ethanol
- The suspension was sonicated for 10 minute to break up any aggregates to ensure a near uniform size distribution of particles
- 200 μL of the sonicated suspension was micropipetted onto a clean glass slide 2 cm x 2 cm
- Surface tension kept the ethanol and powder solution on the surface of the slide while the ethanol evaporated
- After complete evaporation, a thin semi-opaque layer of ZnO powder remained adhered to the slide

The ZnO slides were mounted against an integrating sphere for both transmission and reflection measurements.

Chapter 4

Growth and characterisation of ZnO nanowires

4.1 A review on ZnO growth

Understanding the role of defects and their spatial distribution throughout a ZnO nanowire is of critical importance when considering it as a potential material for use in optoelectronic devices. Surface defects such as hydroxyl groups have been shown to impact the intensity of UV emission [144], while other defects (such as V_O with NO_2) can affect charge transfer between adsorbed molecules and ZnO [145, 146].

Defects in ZnO can be influenced by growth mechanisms, growth conditions, impurities and irradiation effects induced by electron beam based characterisation methods. In this chapter the impact of growth conditions on the structural and optical properties of ZnO are presented. In addition, the importance of accurate analysis and interpretation are discussed.

The different surface structures of ZnO exhibit anisotropic growth [147]. When under thermodynamic equilibrium, facets with higher surface energies tend to have smaller surface areas while the lower energy facets are preferentially larger. In

ZnO, the highest growth rate can be found along the c-axis and the larger facets are typically $\{01\bar{1}0\}$ and $\{2\bar{1}\bar{1}0\}$. Consequently, it is possible to change the growth behaviour of ZnO by controlling the growth conditions. Growth of ZnO using vapour deposition methods can be affected by a variety of factors [121, 148–151], including but not limited to:

- Relative temperatures of the source and substrate,
- Heating rate,
- Gas flow rates,
- Tube diameters,
- and relative positioning of the source to substrate.

All of these factors can be varied easily in the growth process employed during this work, allowing for a systematic investigation of the parameters.

The tips of ZnO nanorods grown through vapour phase methods have been found to be dependant on the relative positioning of the source material to the substrate, resulting in morphologies such as needles and “bottles” [121], tetrapods [152], ribbons, wires and needle-like rods [16]. The growth temperatures have been tentatively identified as the likely cause for ZnO nanostructures varying from nanowires to belts and sheets [148, 149]. Increasing the precursor flow rate and reducing the source-substrate distance results in ZnO nanostructures with larger dimensions [153]. Temperatures significantly higher than the required 907°C for vapour-liquid-solid (VLS) growth tend to result longer, thinner nanostructures with no clear faceting, and Kumar et al. [149] have also reported secondary VS growth can be found as a result of the increased growth temperatures growing from the initial VLS grown structures, with substantially higher temperatures causing foamlike ZnO structures form. Furthermore, the temperature has been shown to influence the crystallinity of ZnO, with higher temperatures producing samples with XRD peaks indicating

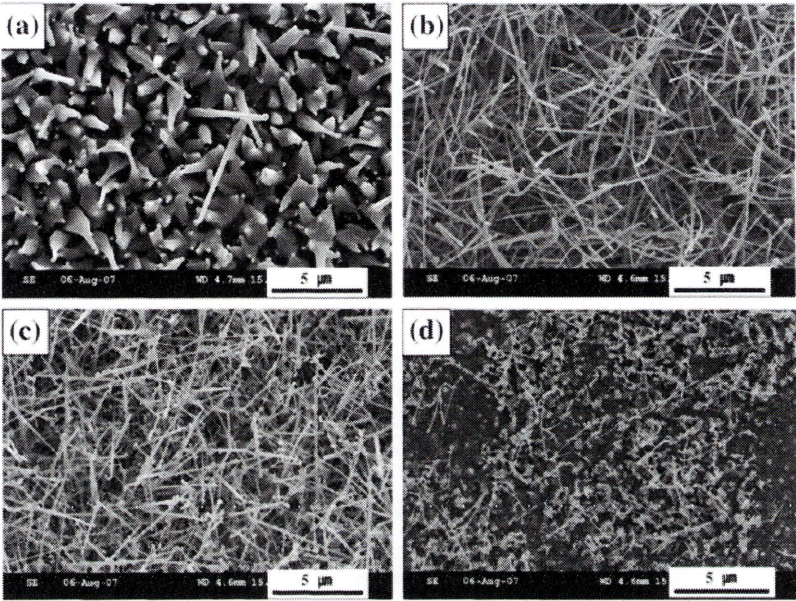
relaxation of tensile stress along the c axis to a comparable value to that of bulk ZnO [151].

In work performed by Kim *et al.* [154], the influence of temperature on the growth of ZnO nanowires has been shown to drastically impact on the nature of the structures. The different morphologies - as evidenced in Figure 4.1(a) - show variation from interconnected blobs at lower temperatures through to wires and near-isolated particles as the temperature increases. Their work also found that the diameter of the structures was dependant on the growth temperature, while the crystalline structure and tip morphology were not noticeably changed.

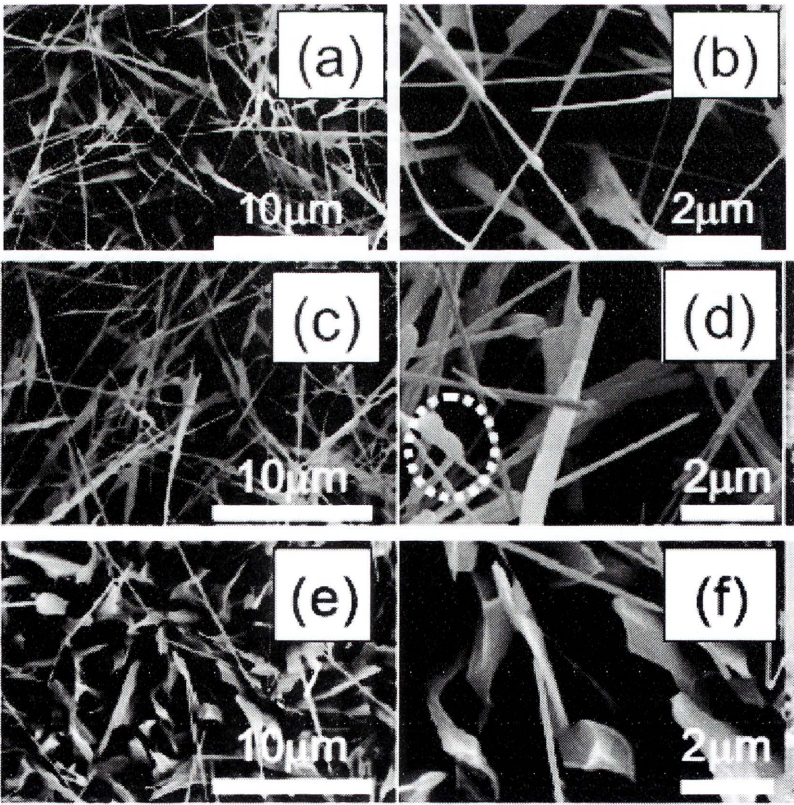
These results appear to contradict those of Kumar *et al.* - Figure 4.1(b) - who instead found that wires form best at temperatures at or below 1000°C [149]. Above this temperature, plate-like structures formed, similar to those observed at lower temperatures for Kim *et al.*. Furthermore, they found evidence of secondary vapour-solid (VS) growth on the produced nanostructures (dotted circle in Figure 4.1(b)(d)). It should be noted that the mechanism of growth proposed by Kumar *et al.* is that of a modified VS theory in which VLS growth occurs at the gold droplets, which then act as nucleation sites for further VS growth, rather than the standard VS growth observed by Kim *et al.* As both primary growth mechanisms are based on VS, the variation between the two experimental findings could be due to further variations not reported in the respective papers.

4.2 Effects of growth conditions on nanostructures in relation to temperature and precursor vapour composition

Several other factors determine the growth of ZnO nanostructures, and a number of studies have been performed in an attempt to identify their influence on the grown



(a) ZnO structures produced at (a) 900°C, (b) 950°C, (c) 1000°C, and 1050°C. From [154]



(b) ZnO structures produced at (a-b) 1000°C, (c-d) 1050°C, and (e-f) 1100°C. Adapted from [149].

FIGURE 4.1: Comparison of ZnO structures produced at different temperatures

structures [121, 148–151, 155]. For example, supersaturation of the gas-phase has been proposed as the growth rate control, while the temperature at the point of growth is suggested to be the primary morphological control. The temperature at the growth location needs to be sufficiently below the temperature at the source to allow for the precipitation of the solid ZnO.

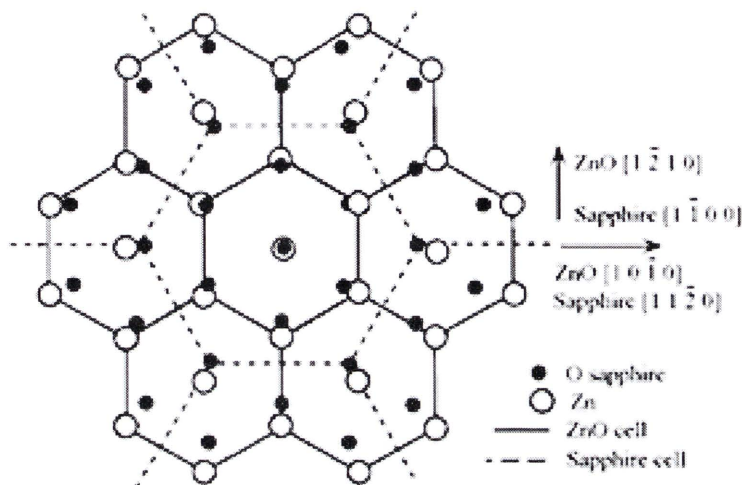
This section shows the influence of several of the controllable parameters in vapour phase ZnO growth in terms of the resulting nanostructure. The influence of varying these parameters on the morphological and optical properties of ZnO nanostructures will be demonstrated. These parameters include:

- Choice of substrate
- Carrier gas
- Growth seeds
- Growth time
- Distance between source and substrates

4.2.1 Effect of substrate type on growth quality and orientation

Controlling the growth orientation is important for many of the proposed applications of ZnO nanostructures. Through the application of conventional epitaxial growth techniques using chemical vapour deposition (CVD) processes, precise orientational control is possible owing to lattice matching between ZnO and the substrate. This results in a reduction in strain, producing a higher probability of producing aligned growth and reducing physical defects.

ZnO nanowires and structures have a growth preferentially along the $\langle 0001 \rangle$ direction. One strategy that is employed to grow vertically aligned structures is to ensure a suitable substrate is chosen so as to form an epitaxial lattice match with

FIGURE 4.2: Epitaxial relationship of ZnO on Al_2O_3 . From [156].

ZnO. As ZnO tends to form in the wurtzite phase with lattice parameters of $a = 3.249 \text{ \AA}$ and $c = 5.207 \text{ \AA}$, there are several substrates to choose from, as shown in Table 4.1.

Sapphire is one such potential substrate choice for epitaxial ZnO growth. The c surface of the sapphire is composed of alternating layers of three-fold symmetric aluminium and six-fold symmetric oxygen atoms. Wurtzite ZnO has six-fold symmetry around the c -axis, meaning that the a -axis of ZnO relates to the c -axis of the sapphire by almost exactly a factor of four with a lattice mismatch of less than 0.1% at room temperature¹. This can best be visualised through Figure 4.2. This means that ZnO nanowires can grow epitaxially from the a -plane surface of sapphire, giving rise to highly aligned growth. This can be seen in Figure 4.3(c), with the hexagonal facets of ZnO clearly observable. In comparison, the more random ZnO orientation grown on c -plane sapphire (Figure 4.3(b)) shows the importance of suitable epitaxial matching.

ZnO crystals can also be used as substrates and would provide a perfect lattice match to the nanowires; however there is difficulty in ensuring that the substrate is not used as a reactant in the vapour transport process, and as such it tends to

¹It should be noted that the thermal expansion coefficients for sapphire and ZnO are different, resulting in marginal perpendicular tensile and parallel compressive strain in ZnO. Thermal expansion is disregarded in this work and only considered here for completeness.

TABLE 4.1: Substrate lattice parameters

	Lattice parameter		Lattice mismatch to c-plane ZnO (%)
	\AA a	c	
a-plane Al_2O_3	4.757	12.983	0.1 [157]
c-plane Al_2O_3	4.757	8.239*	18 or 31.8 [157]
Si $\langle 001 \rangle$	5.430	-	40.1
ZnO	3.249	5.207	0

* value for m -parameter given

be used only in lower temperature growth methods or when regular nanostructured growth is not desired.

Silicon wafers were used as the primary substrate in this work when optimising growth parameters owing to their availability and the ease with which a clean surface can be obtained. Furthermore, silicon offers an exceedingly flat surface along the $\langle 001 \rangle$ face, and while the lattice mismatch is large, comparatively aligned nanostructures are able to grow only once a thin ZnO layer has formed over the surface of the silicon. It should be noted, however, that Si wafers rapidly oxidise on exposure to air to form SiO_2 , an amorphous structure with a variety of possible lattice parameters.

The crystalline quality of the samples produced can be difficult to quantify, as x-ray diffractometry (XRD) studies will only show reflections from planes parallel to the substrate. As such, the quality of the grown structures was qualified by the uniformity of growth direction and alignment. As can be seen in Figure 4.3(a), the growth of the ZnO nanonanostructures on Si are not significantly aligned, rather they branch out irregularly from random points. The wires themselves show considerable uniformity as they grow, which suggests that they are forming in a crystalline manner. As the lattice mismatch with silicon (or silicon oxide/s) is great, the crystallinity observed suggests the formation of a thin ZnO layer over the substrate. This layer can act as a buffer, reducing the lattice mismatch and strain between the growing structures and the substrate. Figure 4.3(b) shows the formation of more

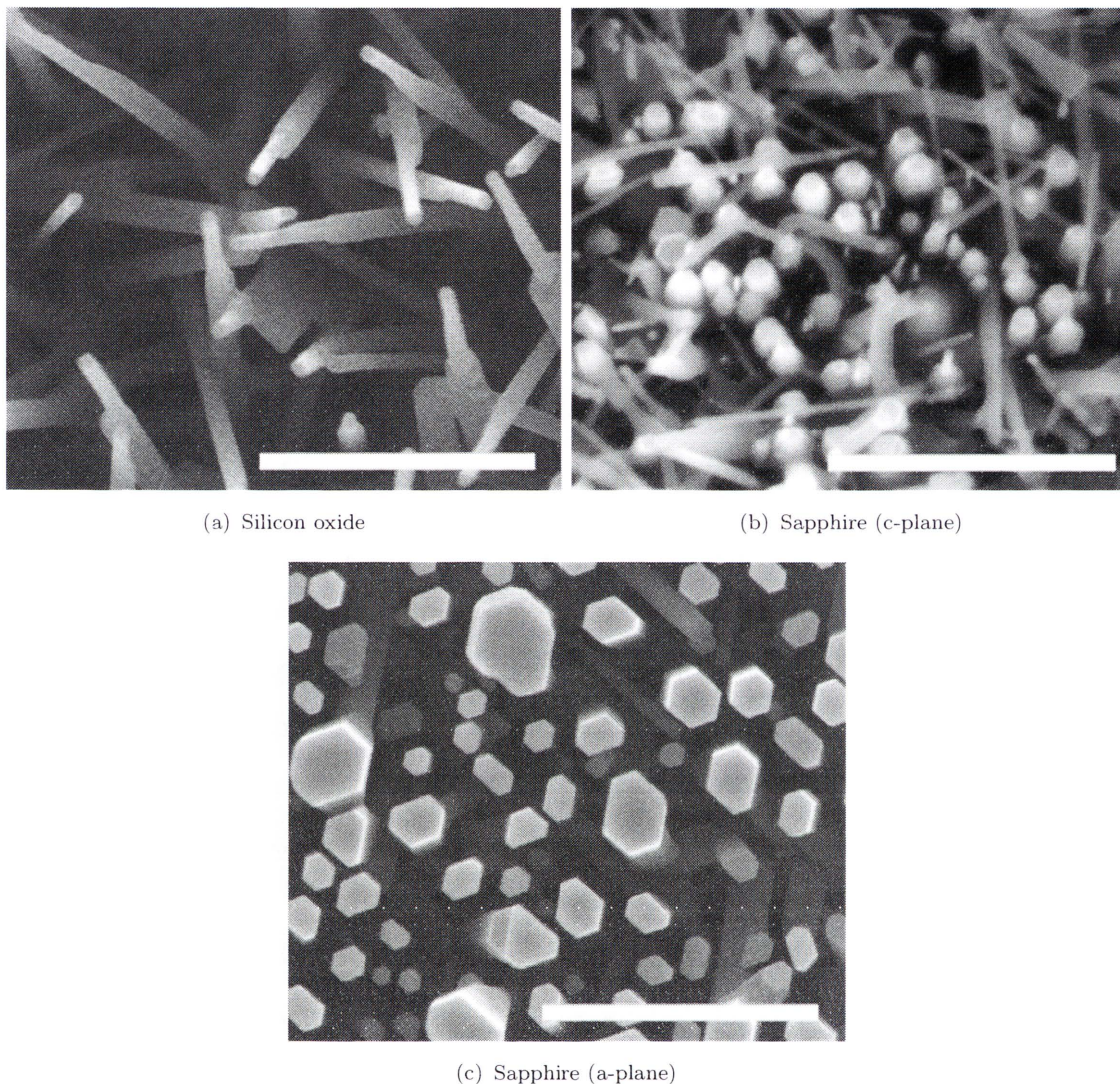


FIGURE 4.3: Comparison of 3 potential substrate choices for nanostructural growth. Scale bar represents $5\mu\text{m}$. Growth conditions other than substrate were kept identical (1 hour growth, 950°C substrate, 10% O_2/Ar at 20 sccm)

aligned, hexagonally faceted structures, along with unwanted plate-like formations, produced on c-plane sapphire. The structures do not, however, show the uniformity observed as found on the silicon substrate, and it is possible to find regions of bare substrate. This suggests that the ZnO layer found on the silicon does not tend to form on c-plane sapphire. As a result of the lack of this layer, the crystalline structures formed on the substrate are subject to significant lattice strain owing to the large lattice mismatch. The irregular plate-like structures that occur between the

hexagonal growths appear to be seeded by the hexagonal growths themselves. The structures grown on a-plane sapphire - Figure 4.3(c) - were produced in a highly aligned manner, along with near uniformity in vertical dimensions. Furthermore, the crystalline nature of the growth was found through XRD studies to be comparable to that of ZnO single crystals grown by hydrothermal methods (see Figure 4.12 on page 91 for a diffractogram).

4.2.2 Carrier gas

A key component in the vapour transport growth technique is the relocation of reactant vapour from one temperature zone to another, or to the desired location of growth. For zinc vapour produced through carbothermal reduction, as is the case in this work, a suitable carrier gas is one that remains inert relative to the chemical reactions, such as argon or nitrogen. Oxygen can also be a component of the carrier gas to aid the oxidation of the Zn vapour at the growth location, typically at lower concentrations relative to the nitrogen or argon. The rate at which the gas flows governs the rate at which the zinc vapour can be carried throughout the furnace tube, as well as influencing the growth locations of the nanostructures.

Flow rates and gas compositions were investigated during this work, ranging from 0 to 1,000 sccm and 0 to 100% respectively. Successful growth was found to be a factor of two components relating to carrier gas; flow rate and gas composition, along with tube pressure. Positive growth results were obtained with gas ratios ($O_2:Ar$) below 1:1, flow rates below 100 sccm, and pressures from 10-200 Torr. Experiments conducted outside of these ranges tended to show predominantly irreproducible nanostructures. In order to perform a systematic study of the influence of carrier gas conditions, the pressure and flow rate were set at 10 Torr and 30 sccm respectively², leaving gas composition as the variable of investigation.

²These parameter settings showed the greatest success rate

In most of the experiments, oxygen was added to the carrier gas. While oxygen is reactive with both the carbon and the Zn vapour present during the growth process, it was added to facilitate the reformation of the ZnO solid material at the growth sites. Typically, the addition of oxygen would necessitate an increase in the ratio of carbon to zinc oxide powder at the source location so as to ensure a sufficient ratio zinc oxide to carbon ratio when the temperature reaches the required level for carbothermal reduction. It was also found that the timing of the introduction of oxygen influenced the growth of the structures. A continuous flow of oxygen from the start can impede the growth of the nanostructures by offering the Zn vapour an opportunity to oxidise preemptively before reaching the gold droplet. By delaying the introduction of the oxygen until reaching higher temperatures, and thus producing enough Zn vapour to saturate the gold, a better quality of nanostructure can be produced. Waiting until source temperatures reached 800°C (heating rate approximately 0.75°C min⁻¹) showed an improvement to the morphological quality of the produced samples, as evidenced in Figure 4.4.

The significant variation in the morphology of the ZnO in relation to the addition of oxygen has been previously observed in literature [158–160], and there are a multitude of potential mechanisms used to explain these observations. Without the presence of added oxygen, zinc oxide nucleation clusters have difficulty forming [159], and for this experiment, it is likely that early introduction of oxygen gas preemptively reacts with the graphite at lower temperatures. This reduces the available graphite for the carbothermal reduction of the ZnO at higher temperatures, resulting in a lower Zn vapour production when the carbothermal temperature is achieved. With a lower ZnO vapour pressure, rather than forming isolated nucleation points and thus aligned columnar structures, when a nucleation point occurs it will preferentially absorb the Zn vapour, forming the less ordered structure observed in Figure 4.4(b).

In addition to morphological changes, the introduction of oxygen to the system has been observed to vary the optical properties of the grown ZnO. This is supported by evidence suggesting that the green defect emission of ZnO is related to oxygen

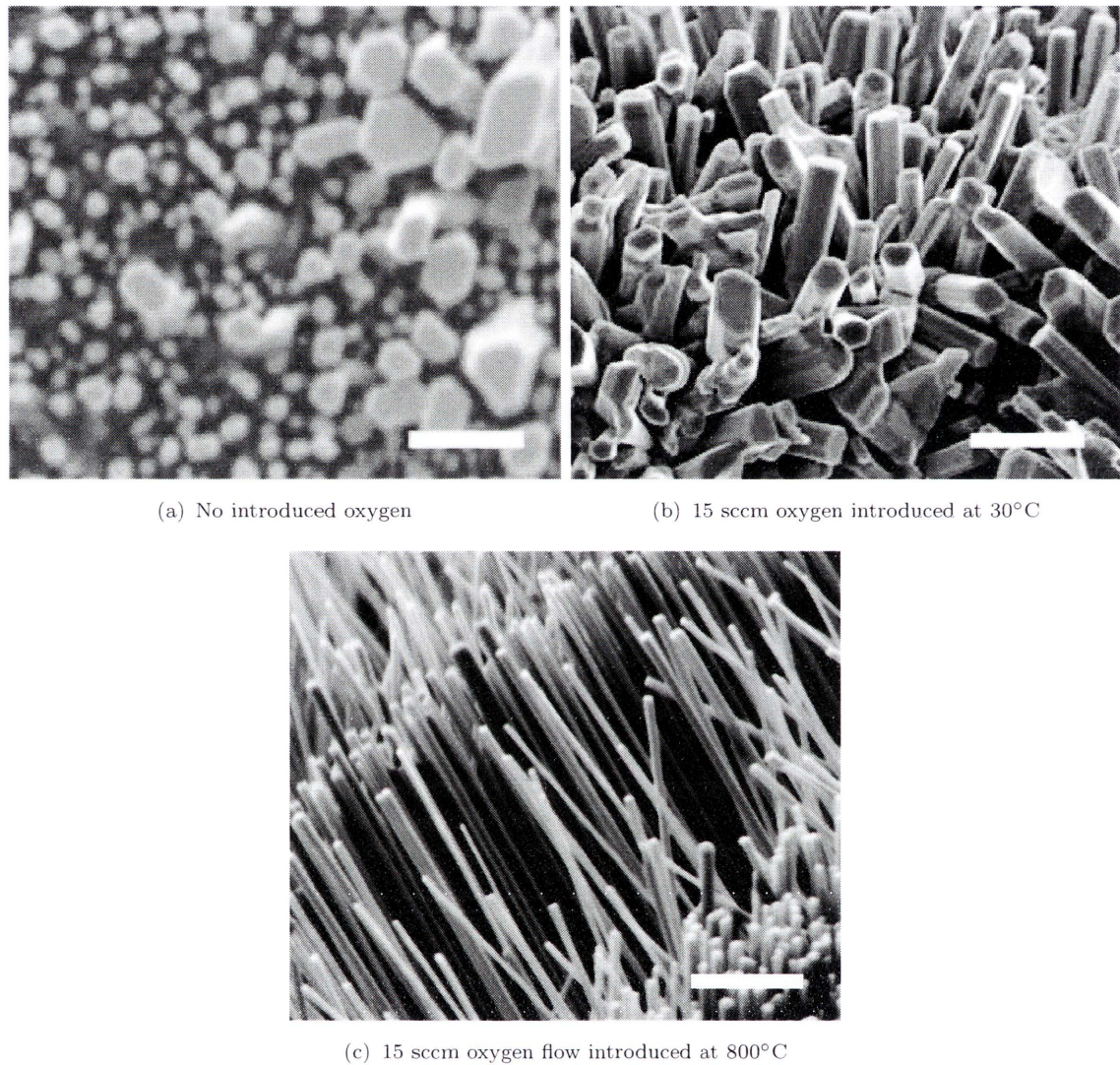


FIGURE 4.4: Comparison of gas flow conditions resulting in different qualities of growth on sapphire substrates. Overall flow rate was maintained at 30 sccm throughout growth with a balance of argon with all other parameters kept constant. Scale bar represents 5 μm .

deficiencies; however this does not completely explain the nature of the emission. The green defect present in ZnO and its oxygen influences will be examined in greater detail in the sections that follow.

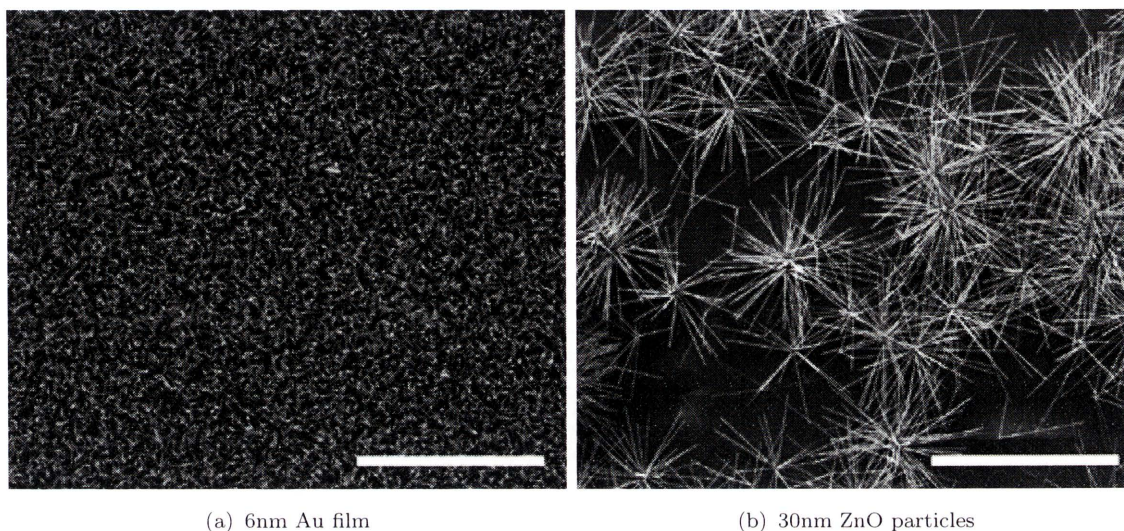


FIGURE 4.5: Examples of ZnO structures grown using different seed layers under identical growth conditions. Scale bars represent $50\text{ }\mu\text{m}$ and 100μ respectively

4.2.3 Growth seeds

The VLS growth mechanism typically uses a thin gold film to form the catalyst for the formation of the ZnO structures. It is possible, however, to utilise alternative seeds that act in a similar manner - a vapour-solid-solid (VSS) mechanism. In this method, the catalyst is a nanoparticle of ZnO that act as the preferential nucleation site for the growth. As the particles are typically not directly adhered to the substrate, this leads to a different growth appearance - spike balls - as shown in Figure 4.5. The benefit of using the nanoparticles is the dispersion of the growth locations, along with the uniformity of the grown structures. The gold film, however, gives a greater coverage and also allows for the growth of highly aligned structures, which is only possible if there is an epitaxial match with the substrate.

A slight shift in the emission properties of the different seed layer samples indicates that the optical properties are influenced either by the nature of the interface between the growth seed and the resulting structure or by the impact of gold during the early stages of structural development (see Figure 4.6)

ZnO nanostructures produced with the gold seed layer exhibits a considerably higher overall CL intensity, while the VSS ZnO seeded sample shows a lower band edge to

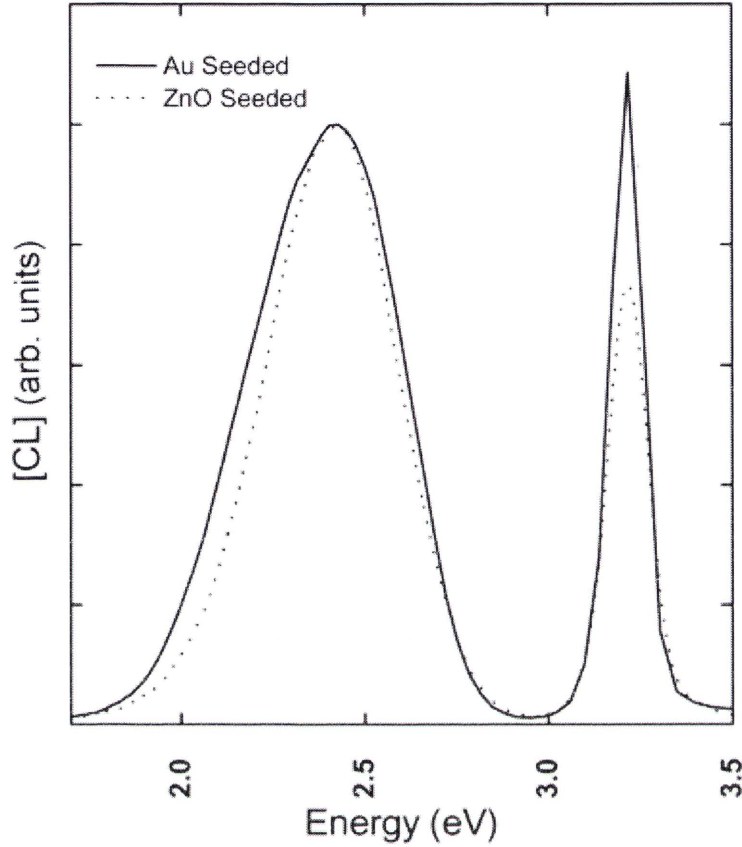


FIGURE 4.6: Comparison of CL spectra obtained from samples produced from different seed layers.

Spectra obtained at 10 kV, 30 μm field of view. Spectra were normalised to the DLE peak

deep level emission (I_{NBE}/I_{DL}) ratio, as evidenced in a representative normalised spectra . There is also a minor shift in the energy of the near band-edge (NBE) emission peak and change in the deep level (DL) line shape.

4.2.4 Growth time

One experimental parameter that is often used to control nanostructural growth is the length of time under which reactions occur. Increasing the growth time from 5 minutes to 2 hours produces significantly different ZnO nanostructure morphology (see Figures 4.7(c) and 4.7(a)). The longer growth time has produced an intricate network of fibrous ZnO wires over a mosaic layer, while the shorter growth time

yields only the lower layer. This lower layer has isolated islands of ZnO nanocrystals populated with small regions showing some evidence of vertical growth. These regions of vertical growth can then act as nucleation sites for the fibrous growth as seen in Figure 4.7(c). The longer growth time allows for a greater volume of Zn vapour to pass the growth region on the substrate surface, providing more material for growth. A growth time of 5 minutes (Figure 4.7(a)) shows greater lateral rather than vertical growth, indicative of the need to form a layer of ZnO prior to columnar formation. This result suggests that a minimum time period is required before growth occurs in the desired fashion. The growth would be expected to follow the maximum vertical (c-axial) growth rate of ZnO nanowires estimated at 3 nm s^{-1} as reported previously [161]. However, the 2 hour growth time (Figure 4.7(c)) does not produce wires $\approx 21 \text{ }\mu\text{m}$ in length, indicating that there is a limiting factor involved. The availability of the Zn vapour to the growth zone appears to be the likely cause of the local growth rates, which will be demonstrated through results obtained in Section 4.2.5. Source material examined after shorter growth times tends to remain grey, with minimal loss of material, while longer runs show an almost complete loss of source material, with the excess ZnO:C appearing as a fine orange powder. The volume loss of the source material for runs greater than ≈ 60 minutes appears similar, suggesting that extending the growth period beyond this length of time will not result in further growth. This observation is supported by results from several other groups [162, 163] who have shown that the longer the growth conditions remain favourable, the longer or larger the structures become. This work concurs with the findings of [162, 163] and suggests that the exposure of grown substrates to high temperatures for extended periods of time can give rise to fibrous ZnO - carpets of fine fibres, interlinked into a dense mat, as demonstrated in Figure 4.7(c). Furthermore, clearly identifiable stages of growth can be observed as a function of growth time [164].

Reducing the time of the reaction conditions also yields information about the early stages of ZnO growth - it would appear that prior to the strong columnar growth of

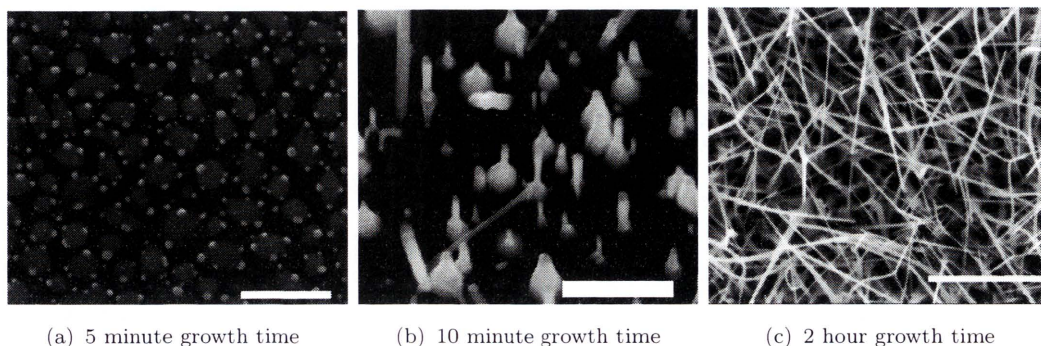


FIGURE 4.7: Influence of length of growth time on the ZnO structures formed. The islands observed in (a) can be seen to act as nucleation points (b) which then extend to form the fibrous network in (c) if growth conditions remain favourable. Scale bars represent $3\mu\text{m}$, $2\mu\text{m}$ and $2\mu\text{m}$ respectively.

aligned nanorods a mosaic wetting layer first forms [165]. These layers show limited vertical but strong lateral growth, with multiple primitive nanorod structures visible in each isolated “tile” of the mosaic (Figure 4.7(a)), as well as visible regions of the substrate. These islands show considerably reduced vertical growth when compared to samples produced under similar conditions with longer growth times.

4.2.5 Distance from source

Relative positioning of the source to the substrate has been found to have a major effect on the resulting structure [148] and optical properties [161] of ZnO growth. By controlling the growth parameters, substantial variations in the grown ZnO structures can occur across a single substrate - on the order of millimetres. In regions nearest to the source material, vertical nanowires form with a uniform distribution of diameters (Figure 4.8(a)), exhibiting clear hexagonal cross-sections. The morphology of the wires is similar ZnO structures produced by chemical vapour deposition in other works [165]. As distance from the source material increases, the ZnO does not form the columns as readily, instead a mosaic layer of pedestal bases is produced, acting as anchors for future growth (Figure 4.8(b)). These pedestals become

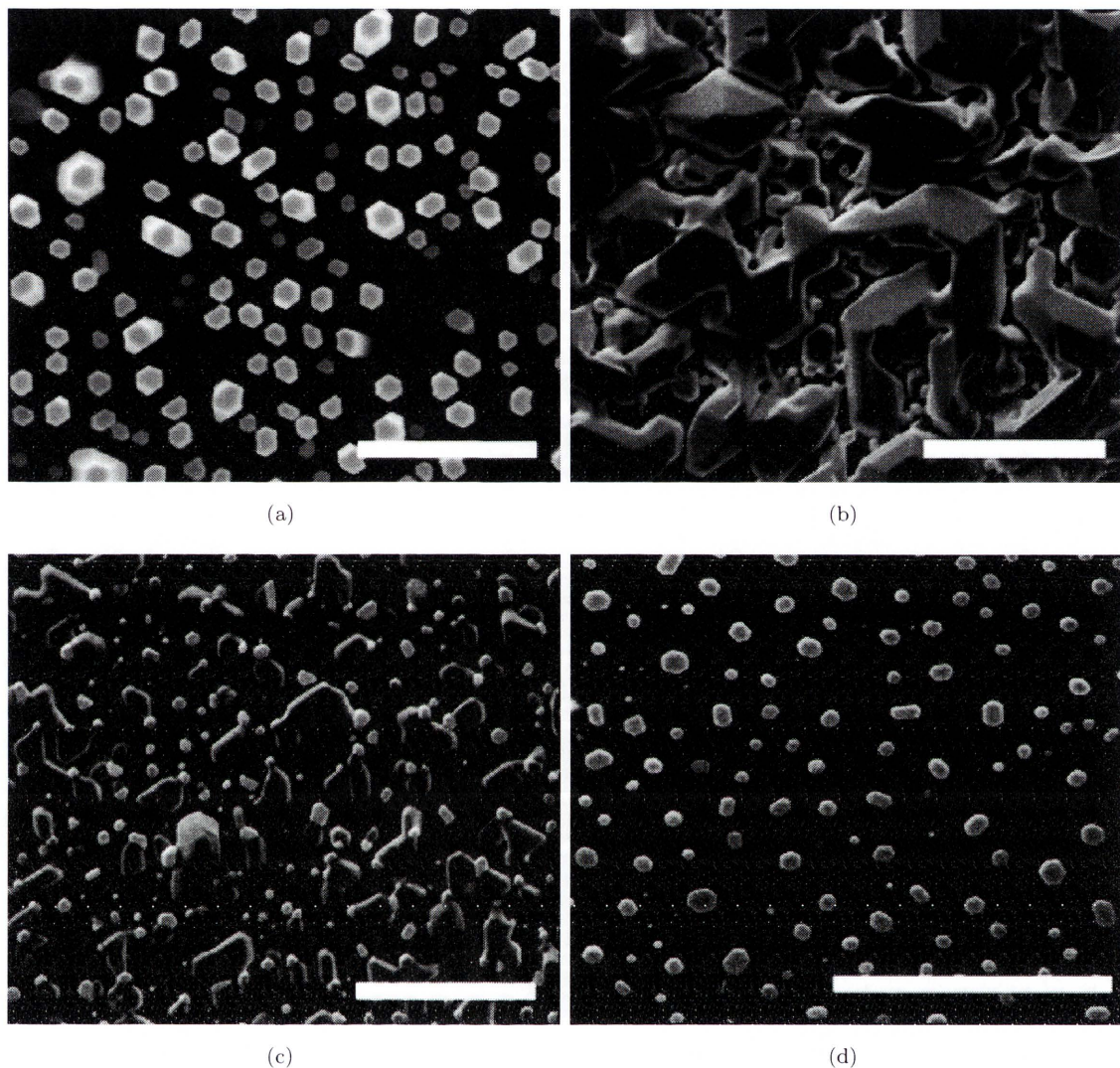


FIGURE 4.8: Relative positioning of growth relative to source from (a) nearest source to (d) furthest from source material. Scale bar represents $4\ \mu\text{m}$

more isolated further from the source until they form individual islands, (c) , and eventually singular ZnO nanodots(d).

The CL spectra for growth types (a)-(c) is shown below in Figure 4.9. Growth type (d) was not examined under CL as the interaction volume of the electron beam was substantially greater than the size of the structures. Reducing the accelerating voltage of the beam to account for this reduction in structure size resulted in a poor cathodoluminescence (CL) signal to noise ratio. The spectra were obtained under identical excitation conditions to allow for direct comparison. The intensity of the

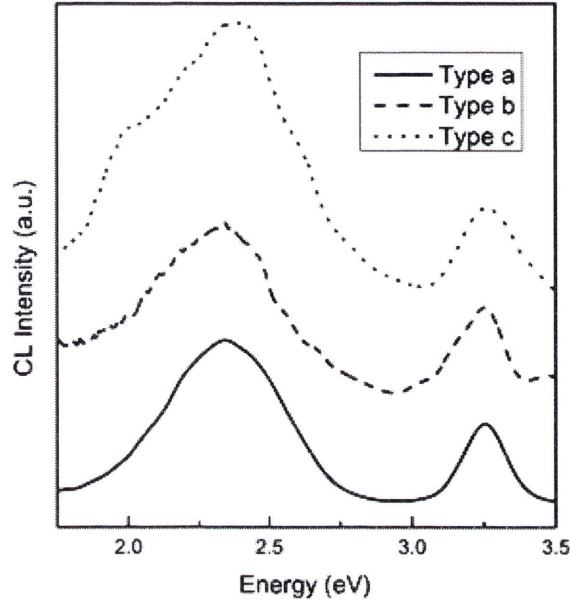


FIGURE 4.9: CL spectra for ZnO structures formed at a distance from the source material as identified in Figure 4.8, with a) being closest to the source material and c) being the furthest. Spectra collected at 10 kV, 0.6 nA, 30 μm field of view

green luminescence (or deep level (DL) luminescence), relative to the near band edge intensity, becomes progressively more intense as distance from the source material increases. The DL:NBE ratio was found to be 13.6, 14.6 and 15.8 for samples in Figure 4.8(a)-(c) in Figure 4.9 respectively.

An increase in the green defect emission is often attributed to oxygen vacancies in the ZnO structures. As the majority of the growth parameters are kept constant, the variation in the emission characteristics and structural formation is proposed to be due to variation in the vapour mixture along the substrate, following on from Song et al. [155] and their studies on relative O_2 partial pressures during growth. Oxygen is consumed rapidly in the growth zone by both Zn and C, and as such the oxygen concentration is expected to decrease rapidly with distance from the source material. The Zn vapour generated carbothermally, however, is continuously generated and varies insignificantly throughout the growth zone.

The rapid decrease of oxygen availability and subsequent increase in the $I_{\text{DL}}:I_{\text{NBE}}$ ratio would indicate that oxygen deficiency is a component of the green defect band.

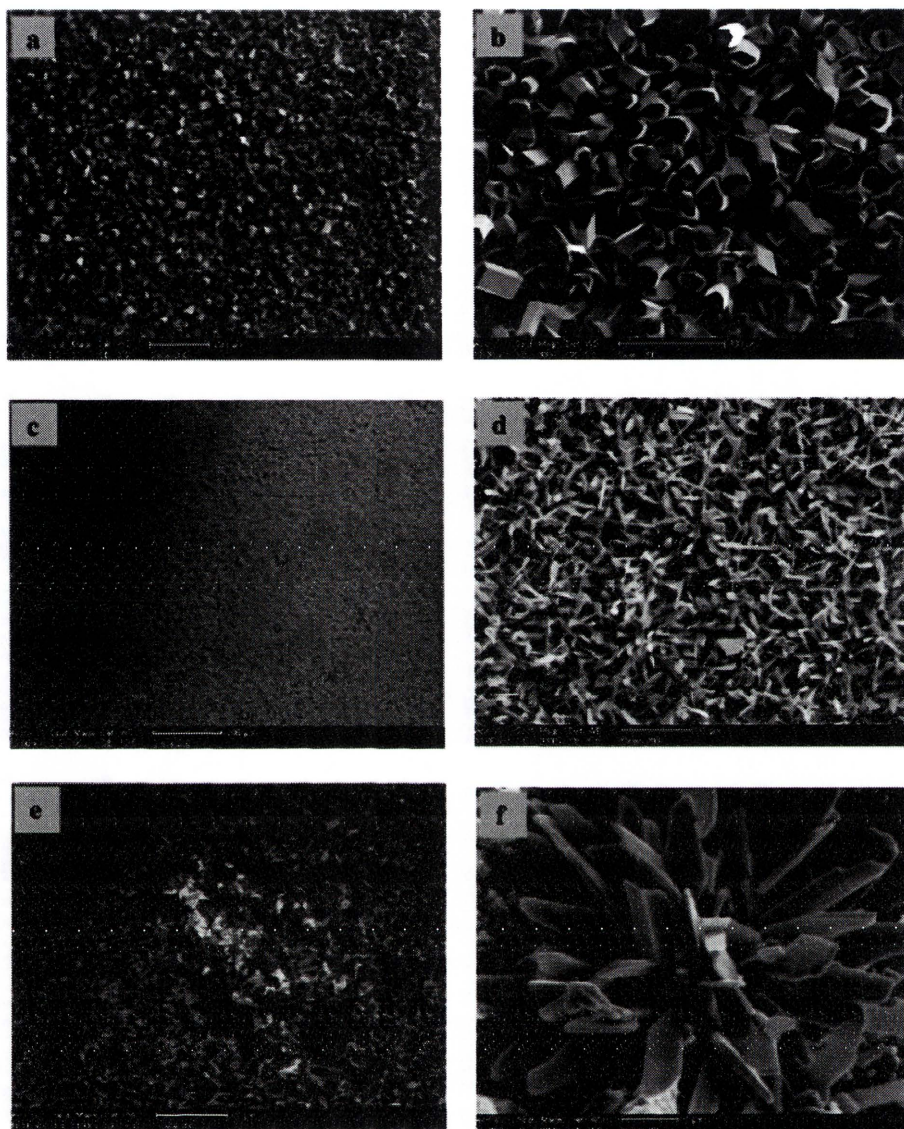


FIGURE 4.10: ZnO structures formed at increasing distances from source material. b), d), and f) are magnifications of a), c) and e) respectively. [148]

The structural findings are in contrast to the findings of Ye *et al.* [148]. In their work, the aspect ratio of the structures was found to correlate to the distance from the source material - as one increases so does the other. Their results produced a variety of structures of a very different nature to the ones found in this work (refer to Figure 4.10). While nanorods were produced in the region closest to the source in this work, the structures rapidly degrade to multifaceted crystalline films, while Ye *et al.* have irregular columnar structures that change through several morphologies.

It is suggested that the distance from the source material influences the structures by impacting the gas-phase saturation and relative temperature of the substrate to the source. The results obtained in this work would support this theory, however the influence of the vapour phase saturation and minor variations in the substrate temperature relative to the source on the resulting growth would appear to differ from previous reports.

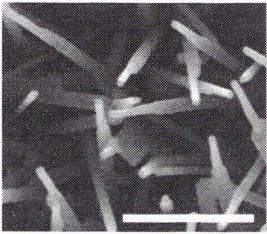
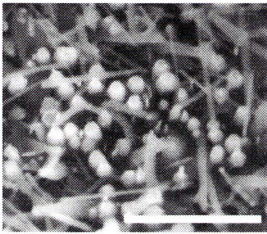
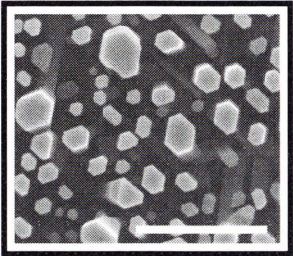
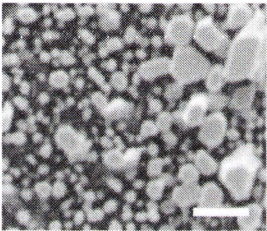
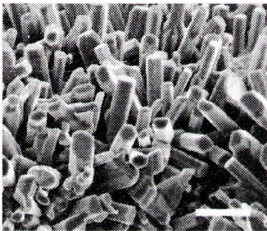
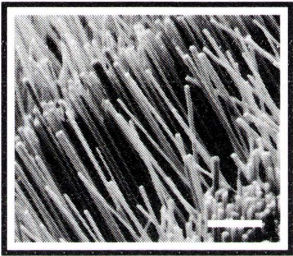
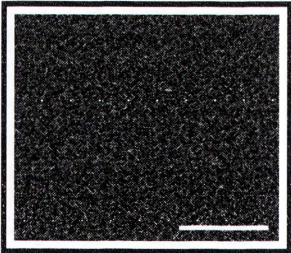
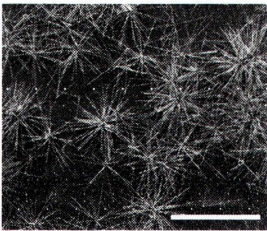
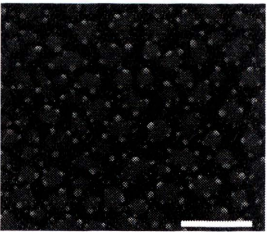
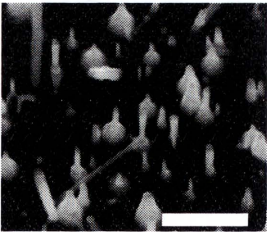
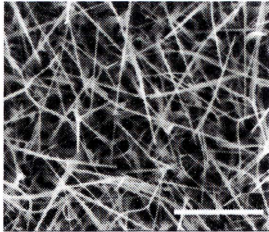
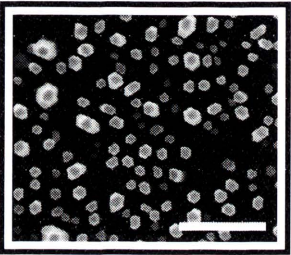
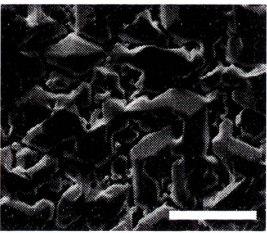
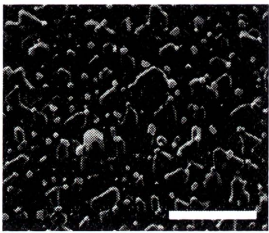
4.2.6 Summary of growth conditions on ZnO nanostructures

While the growth mechanism behind vapour phase growth of ZnO structures is still not fully understood, it appears that there are several conditions that need to be met to produce specific nanostructures. The controls that were investigated and their influence on the structures formed, as summarised in Table 4.2 indicate a narrow window of conditions to achieve successful nanorod or nanowire growth.

The successful parameter values³ are highlighted with a border. As can be seen from the results, the successful “recipe” for preparation of ZnO nanorods would be prepared on a-plane sapphire coated in a thin Au film, grown for 1 hour with the substrate as close to the source material as possible and oxygen only being introduced at temperatures approaching the critical temperature for carbothermal reduction of ZnO.

³Success was defined as reproducibly yielding nanostructures approaching an ideal aligned columnar nanorod array

TABLE 4.2: Summary of growth conditions and resulting nanostructures

Substrate choice		
		
Silicon	Sapphire (c-plane)	Sapphire (a-plane)
Oxygen introduction		
		
Not introduced	Present throughout	Introduced $T \geq 880^\circ\text{C}$
Growth seed		
		
7 nm Au film	30 nm ZnO powder	
Growth time		
		
5 minutes	10 minutes	2 hours
Distance from source		
		
—————→ Increasing distance from source —————→		

4.3 Relationship between structure and optical properties

Understanding the role of defects and their spatial distribution throughout ZnO is of critical importance when considering it as a potential material for use in optoelectronic devices. Surface defects such as hydroxyl groups have been shown to impact the performance of UV emission [144], while other defects can inhibit charge transfer between adsorbed molecules and ZnO [145].

The cathodoluminescent characteristics for ZnO can vary significantly depending on the size of the nanostructure and the depth and shape of the electron beam interaction volume. As this can occur in both pure and impure ZnO, these variations have been attributed to the influence of intrinsic defects occurring within the sample. The following section intends to explain the wide variation in the reported properties of ZnO structures in literature as a result of potentially inaccurate interpretation of results.

4.3.1 Inhomogeneity in optical properties of ZnO structures

Highly aligned ZnO nanorods were grown on *a*-plane sapphire as described in Chapter 3. Figure 4.11 shows that the rods grow perpendicular to the substrate with strong hexagonal symmetry over a large surface area. The ZnO nanorods have diameters between 100 and 800 nm and a height of approximately 5 μm . The hexagonal symmetry of the rods and degree of alignment are indicative of a high level of crystallinity. This was verified through conventional $\theta - 2\theta$ XRD, resulting in the diffractogram in Figure 4.12. The diffractogram reveals only two strong peak intensities at $2\theta = 34.42^\circ$ and 72.57° assigned to the (0002) and (0004) reflections of ZnO, which are both multiples of the [0001] preferential growth direction of ZnO. The epitaxial growth exhibited is consistent with the in-plane orientation relationship

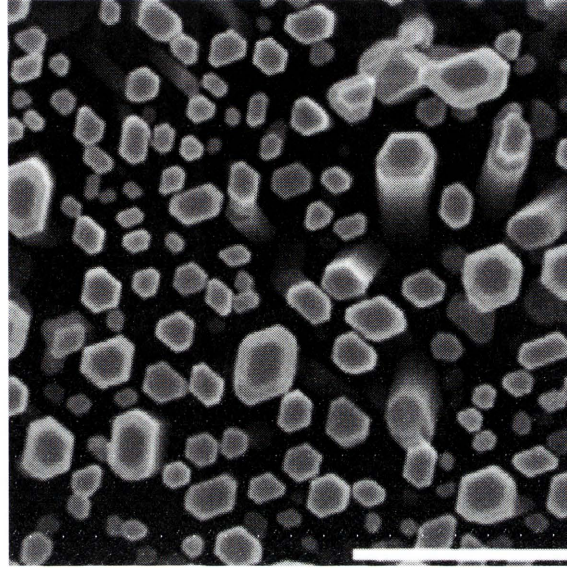


FIGURE 4.11: Highly aligned ZnO rods grown on sapphire substrate showing regular hexagonal faceting indicative of high crystallinity. Scale bar represents $4\mu\text{m}$

observed between ZnO and *a*-plane sapphire [166] while the body of the nanorods are bounded by six crystallographically equivalent $\{10\bar{1}0\}$ facets. Further evidence supporting the alignment of the nanorods can be found through a θ -rocking curve of the ZnO (0002) plane (Figure 4.13) which has a full width at half maximum (FWHM) of only 1.3° . This narrow FWHM implies that the *c*-axes of the ZnO nanorods are well aligned to the normal of the substrate.

The CL spectra obtained from ZnO nanorods display a NBE emission at 3.3 eV and a broad DL defect related band centred at approximately 2.3 eV (Figure 4.14). The CL exhibited by the vertically aligned nanorods is similar, however the $I_{\text{NBE}}:I_{\text{DL}}$ varies significantly with the location of the electron beam probe on the nanorod. Under identical acquisition parameters (5 kV, 2 nA, $12,000 \times$ magnification), the intensity of the green emission at the nanorod tip is considerably less than the green emission observable from the nanorod sidewalls. The NBE emission however appears to be found distributed relatively uniformly throughout the structure, with a slight anti-correlation to the green emission towards the sidewalls of the rods (see Figure 4.17. The penetration depth of the electron beam at 5 kV is approximately

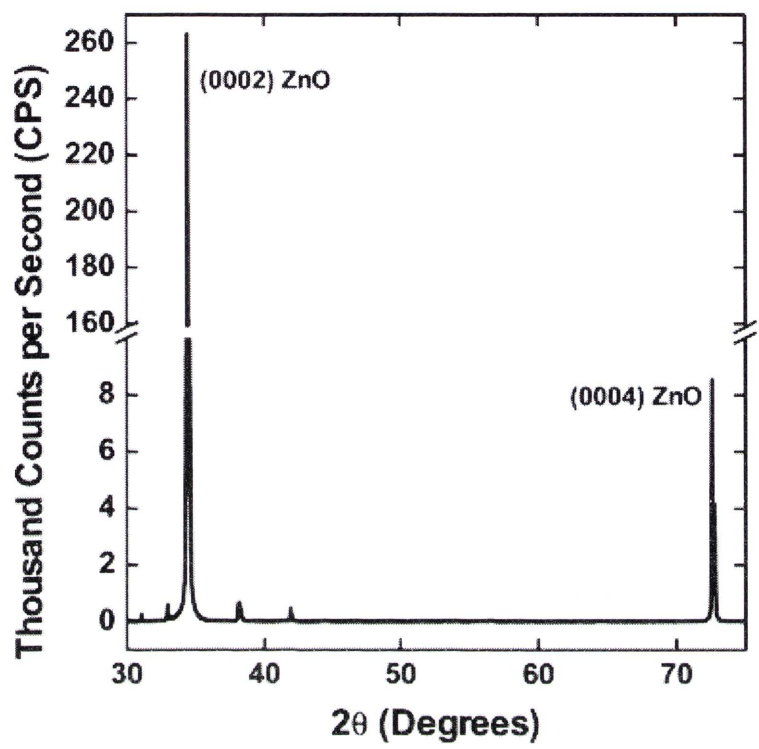


FIGURE 4.12: XRD $\theta-2\theta$ plot of ZnO nanorods shown in Figure 4.11 confirming the epitaxially matched growth to the sapphire substrate.

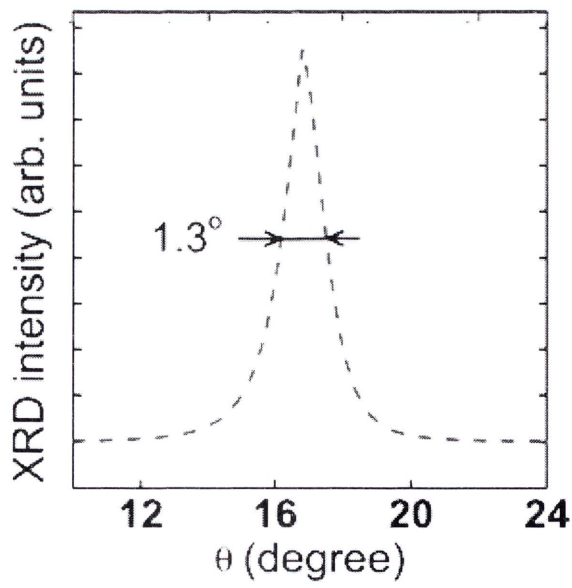


FIGURE 4.13: Rocking curve of (0002) plane from ZnO nanorods grown on *a*-plane sapphire. The narrow FWHM is indicative of a strongly crystalline material.

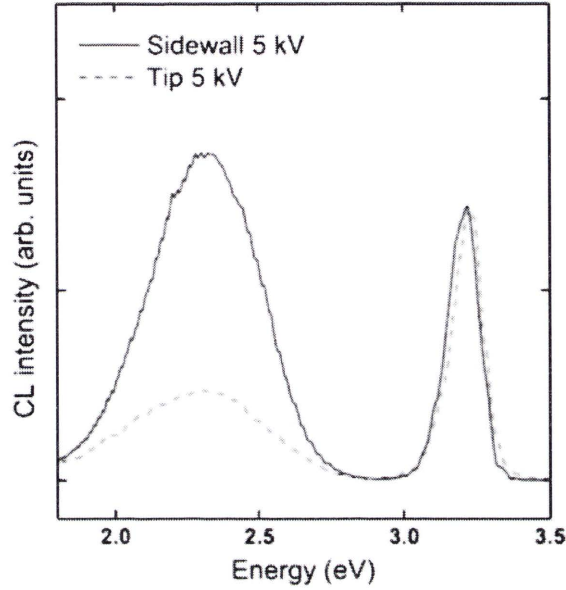


FIGURE 4.14: CL spectra (normalised to the NBE emission peak intensity) obtained from the tip and the sidewalls of grown ZnO nanorods at 5 kV, 2 nA at 300 K. The relative increase in the defect peak (centred at 2.2 eV) to the NBE peak indicates a difference in the defect distribution across the nanorod diameter.

180 ± 20 nm with a CASINO modelled CL generation depth of approximately 20 nm.

Reducing the electron beam accelerating voltage from 5 kV to 1 kV reduces the intensity of both the NBE and the DL emissions as expected owing to the reduction in electron-hole pair generation. However, the intensity ratio between the NBE and DL changes significantly with the DL green peak now dominating the NBE. Figure 4.15 shows the relative increase of the green emission to the NBE at the lower accelerating voltage. This increase in the relative green emission at low CL voltage operation (resulting in an effective CL excitation depth of ≈ 10 nm at 1 kV) supports the observation that green luminescence originates from the ZnO surface [167, 168].

The different emission characteristics can be emphasised through monochromatic CL imaging, as shown in Figure 4.16. The NBE emission is distributed uniformly over the nanorod while the defect distribution displays a significant inhomogeneity between the nanorod tip and sidewalls.

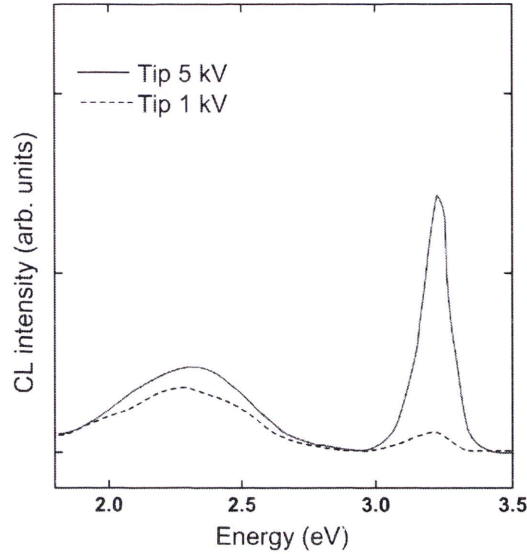


FIGURE 4.15: CL spectra obtained from the sidewalls of ZnO nanorods at different accelerating voltages. The increase in the NBE emission at 5 kV indicates the surface sensitivity of the CL emission - at 1 kV the penetration depth is less than 10 nm, while at 5 kV the beam penetrates closer to 200 nm. This suggests that the green emission is localised to the surface of the rods.

Spatially resolved cathodoluminescence spectra have been collected across single ZnO nanostructures previously that show this effect conclusively [169, 170] with the maximum DL emission intensity occurring at the sidewalls. A gray-scale line map through the monochromatic CL scans results in a plot similar to Figure 4.17, where the strong DL emission is observable inverse emission characteristic becomes apparent at the edge of each rod.

It has been shown that the deep level emission in ZnO nanostructures have a dependence on the surface crystal plane [171]. Emission in the green spectral region is considerably stronger from the nonpolar surfaces than that of the polar. The nonpolar surfaces are electrically neutral, and as such have a low count of defects at the surface, while the polar surfaces have surplus charge that needs to be compensated to form a stable surface. As the nanorods shown in Figure 4.16 have grown along the $\langle 0001 \rangle$ axis (as verified through XRD), the side surface of the rod is terminated by a nonpolar crystal plane. The green emission is notably greater at across this

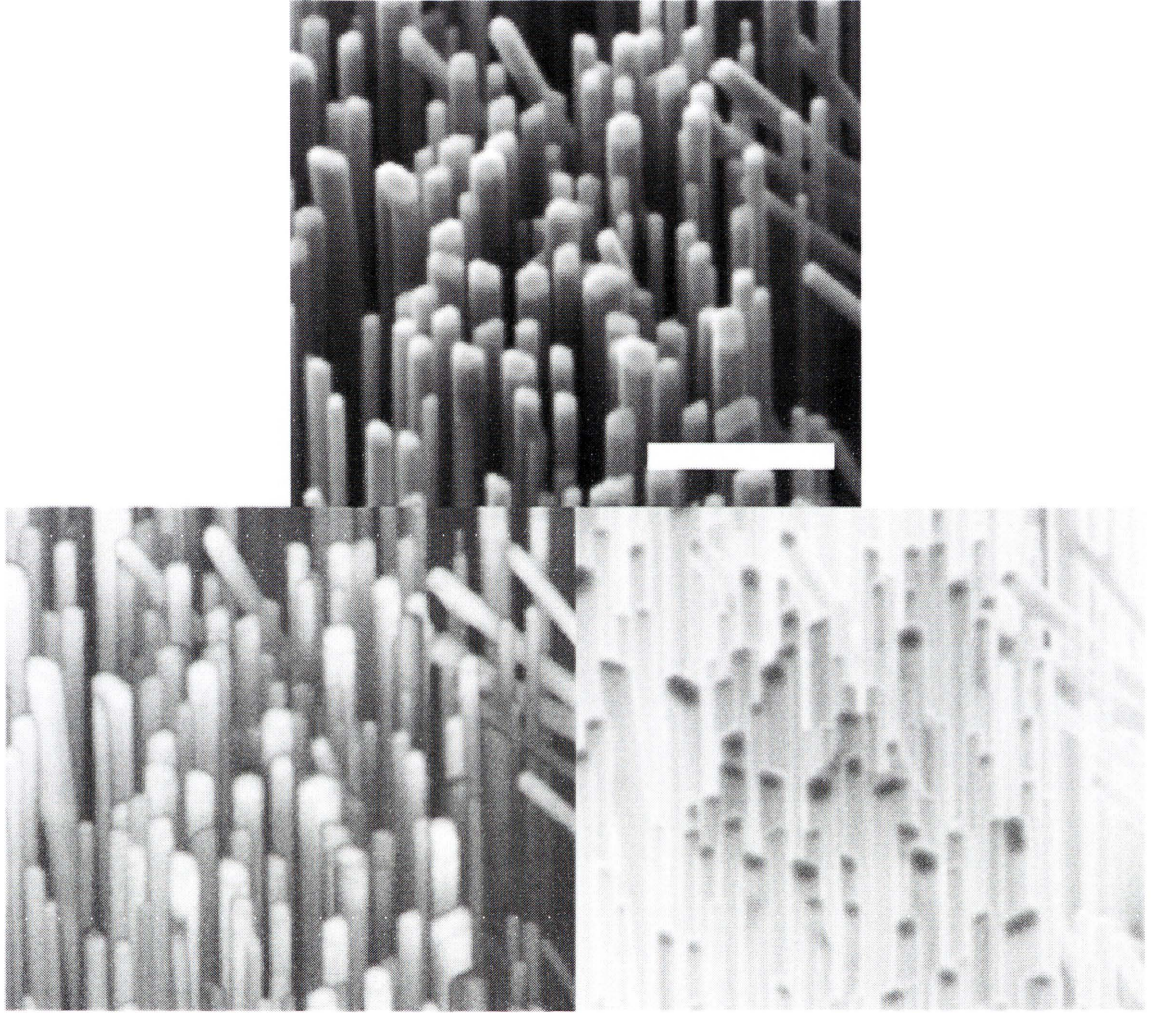


FIGURE 4.16: Monochromatic images of ZnO nanorods showing localisation of CL emission. Images were collected using a 10 nm band pass at 77 K. Scale bar represents 4 μm .

surface, and this increase in emission has been attributed to the defects formed on the surface during nonpolar surface stabilisation, such as oxygen vacancies.

Other possible explanations include surface band bending or competitive recombination mechanisms between the NBE and DL channels.

Band bending at the surface of ZnO will create an electron depletion layer of width W ;

$$W = \sqrt{\frac{2\epsilon_{\text{ZnO}}\epsilon_0\Phi_S}{e^2(N_D^+[\text{T}])}} \quad (4.1)$$

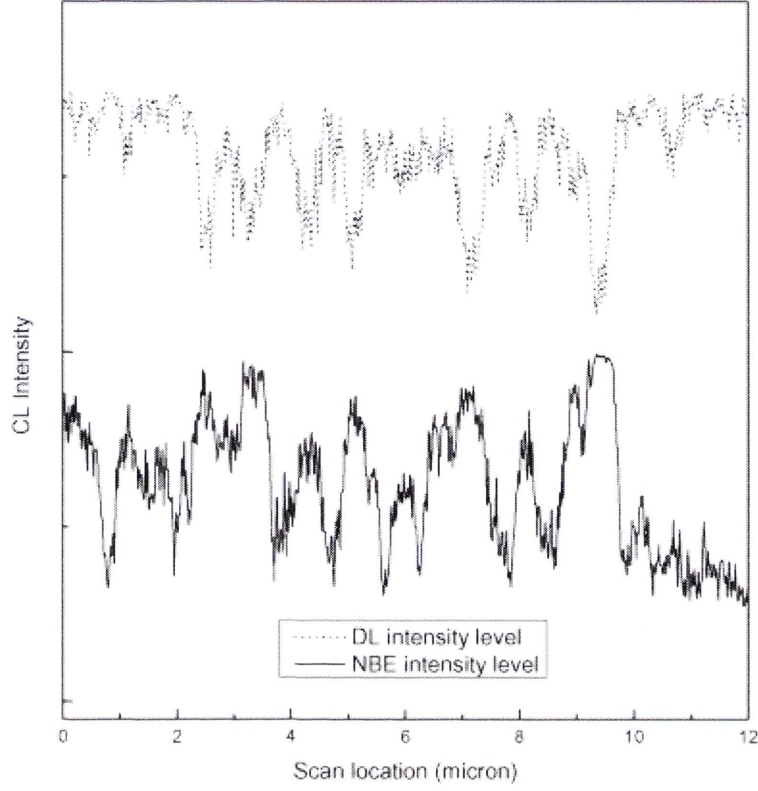


FIGURE 4.17: Monochromatic CL line scans of ZnO nanorods showing the inverse relationship between the NBE and DL emissions

where ϵ_{ZnO} is the relative dielectric constant of ZnO, ϵ_0 is the permittivity of vacuum, Φ_S is the height of potential barrier, e is the charge on an electron, and $N_D^+[T]$ is the temperature dependant activated donor concentration found from;

$$N_D^+[T] = \frac{N_D}{1 + 2e^{\frac{E_F - E_D}{k_b T}}} \quad (4.2)$$

If N_D is taken as approximately 10^{17}cm^{-3} at room temperature, $\epsilon_{\text{ZnO}} = 8.7$, and Φ is 0.5 eV [172], the depletion layer width in ZnO is calculated to be approximately 69 nm. As shown in Figure 4.18, if the dimensions of a ZnO nanostructure approach $2W$ then the structure will be fully depleted, with all V_O^x centres being converted to V_O^+ and V_O^{++} (4.18(a)), giving rise to emission from the singly and doubly ionised oxygen vacancies. If the dimensions exceed $2W$ however, then a depletion region can be expected to co-exist with a non-depletion region. In this

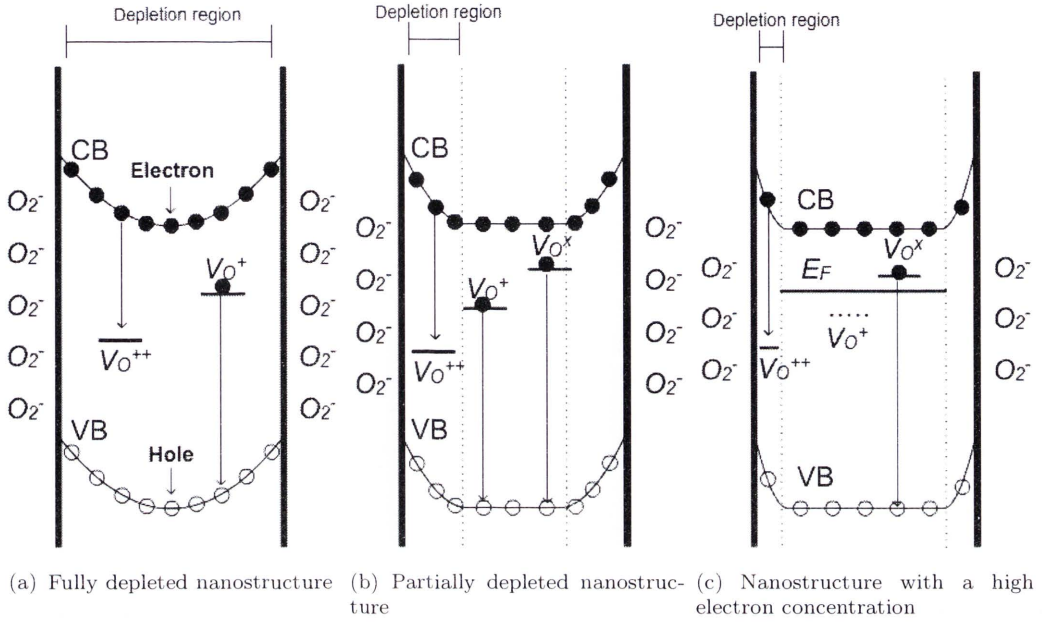


FIGURE 4.18: Diagrams of the energy band in ZnO nanostructures under three different surface depletion region types.

- (a) Full depletion has occurred, leaving V_O^+ and V_O^{++} centres.
- (b) Partial depletion - the V_O^{++} centres can only be found in the depletion region near the surface, while V_O^+ and V_O^x can co-exist in the non-depletion region.
- (c) The high electron concentration has reduced the width of the surface depletion region. Furthermore, the high carrier concentration raises the Fermi level higher than the V_O^+ level, resulting in a complete filling of all the V_O^+ centres. The V_O^x centres can still be found in the non-depletion region.

case, different emission properties can be expected from different locations within the structure. As the observed edge effect in the nanorods from Figure 4.16 are significantly larger than the proposed depletion layer width (approximately an order of magnitude greater), band bending effects cannot be solely employed to adequately explain this localised variation in the optical emission.

The competitive nature of recombination could also offer an explanation for the observed emission variation. As there are a finite number of electron-hole pairs being recombining at any given time, preference is given to the most efficient recombination channel. The introduction of alternative recombination pathways through defect centres could explain the anti-correlation between the band edge and defect optical

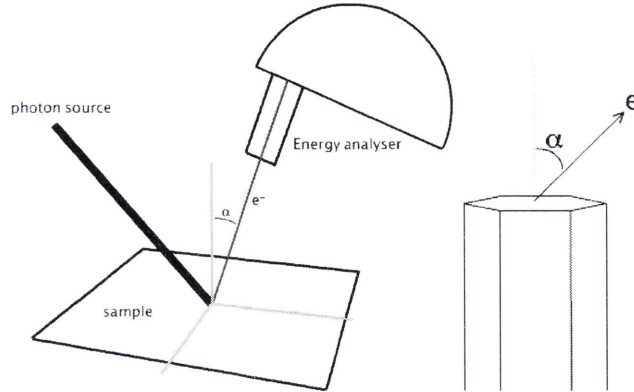


FIGURE 4.19: Schematic diagram of ARPES experiment. As the sample is tilted the incidence angle of the synchrotron light source changes, varying α . At $\alpha=0^\circ$, only the nanorod tips are probed, while as α increases the contributions from the sidewalls increase.

emissions. This would still rely on the presence of a inhomogeneous distribution of defect centres within the crystal however.

To investigate the defect distribution, angle resolved photoemission spectroscopy (ARPES) experiments were conducted on highly aligned ZnO nanorods. As photoemission spectroscopy (PES) is highly surface sensitive (within approximately 6 nm of the surface) technique, it is possible to identify the relative localised defect concentrations between different locations. ARPES is typically used to investigate the momentum of emitted electrons, however by varying the detection angle of the x-rays over a nanorod array different facets can be examined and compared. As shown in Figure 4.19, it is expected that any spectra obtained at normal incidence ($\alpha = 0^\circ$) will be dominated by the surface of the nanorod tip, while as α increases the contribution to the electron signal from the sidewalls increases.

If the O1s PES spectra of the nanorods at different α values are compared, as shown in Figure 4.20, it can be seen that the O1s line shape broadens on the higher binding energy side as α increases. This spectra can be resolved by a Voigt fitting distribution into two peaks - 529.9 eV and 531.3 eV - which have been attributed to O^{2-} ions surrounded by fully coordinated Zn atoms and O^{2-} ions in oxygen deficient ZnO respectively [173, 174]. It is clear from Figure 4.20 that the intensity

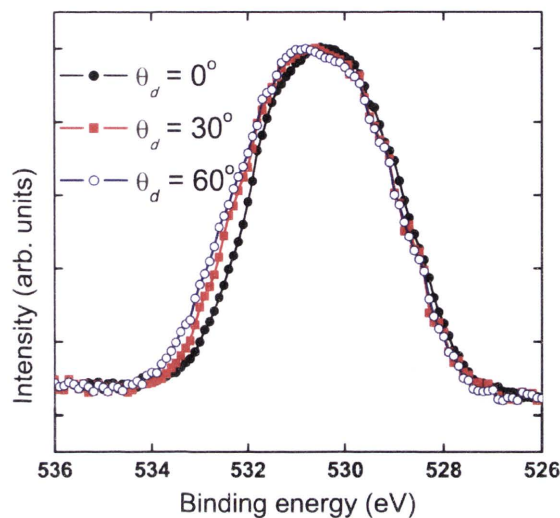
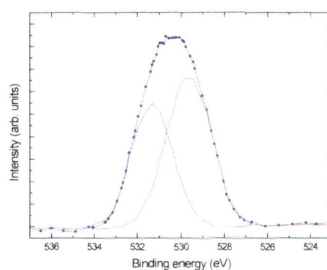
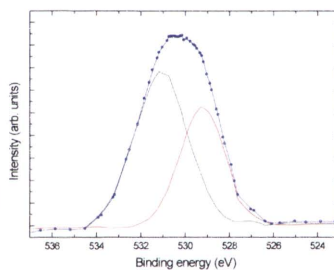
(a) Spectra for different α values(b) $\alpha=0^\circ$ (c) $\alpha=60^\circ$

FIGURE 4.20: Comparison of the O 1s XPS spectra of the nanorods acquired at different photoelectron detection angles. The spectrum is broadened to the high-binding-energy side as α is increased from 0° to 60° . (b)-(c) The O 1s spectra can be resolved using a Voigt fitting into two peaks corresponding to two chemically different environments.

of the non-stoichiometric component increases with α , corresponding to an increase in oxygen deficiency along the nanorod sidewalls.

4.3.2 Luminescent properties of individual wires and as-grown ensembles

The optical and electronic properties of ZnO nanostructures grown through CVD methods can be influenced by the substrate on which they are produced. The study

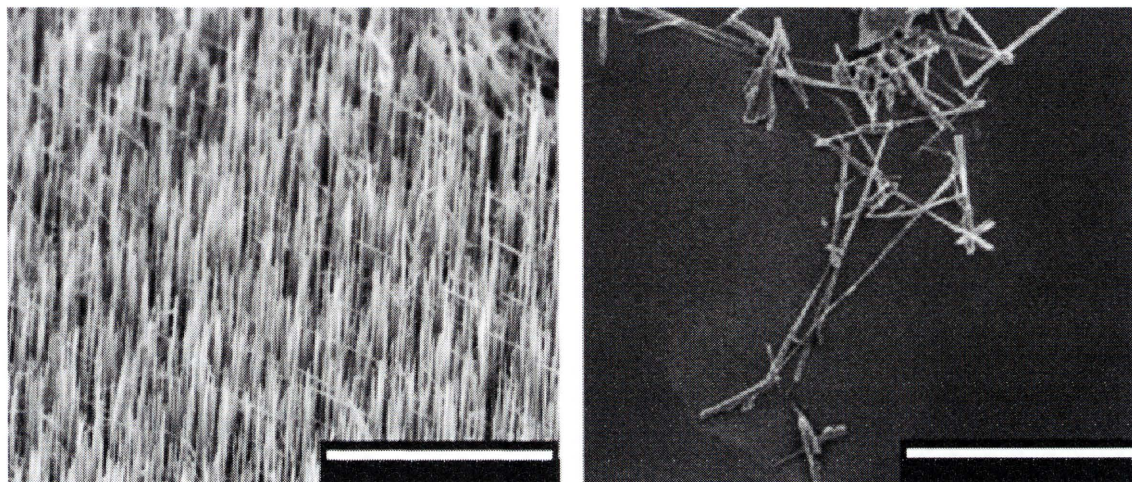


FIGURE 4.21: As grown (left) and extracted ZnO nanowires (right). Wires were extracted using ultrasonication and deposited onto clean Au coated silicon substrates for analysis. Scale bars represent 20 and 10 μm respectively.

of individual structures is of interest as the behaviour of a single nanostructure can vary substantially within a given sample. As the volume and depth of a CL probe can exceed the size of a nanostructure, resulting in the probing of more than one wire, rod or plate, for example, it is necessary to isolate individual wires for analysis. This is done by sonication of the as-grown samples in ethanol for 10-20 minutes, stripping the wires from the substrate. Nanowires were produced using the method as discussed in Chapter 3 on a sapphire ($11\bar{2}0$) substrate. X-ray photoemission spectroscopy (XPS) survey spectra of the as-grown nanowires showed only Zn and O signals with no evidence of impurities. These wires were then stripped through ultrasonication and drop cast onto a clean, gold coated silicon substrate. The as-grown wires produced show a large aspect ratio along with hexagonally faceted tips, with typical heights of 2-6 μm and diameters of 50-120 nm. The majority of the grown wires were aligned vertically to the substrate prior to removal, indicative of lattice matching and strong c-axial growth, but there were some wires growing irregularly, possibly indicative of secondary growth seeded off an existing wire.

As can be seen in Figure 4.21, attempting to isolate an individual wire from the as-grown sample to analyse using CL would require the wire to be separated from its neighbours by a significantly greater distance. However, by extracting and isolating

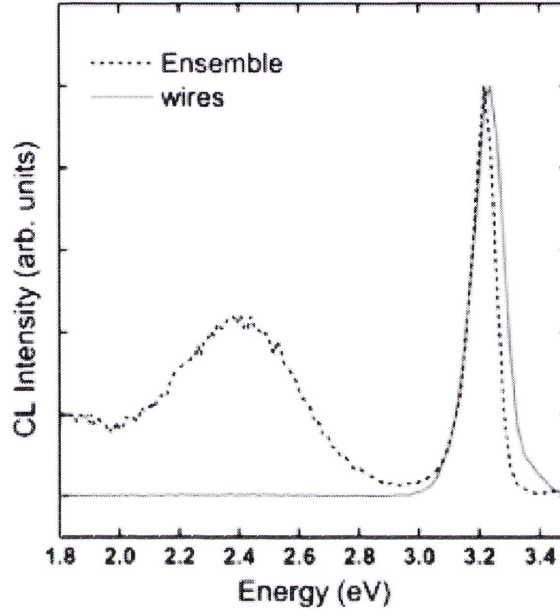


FIGURE 4.22: CL spectra of as-grown and extracted ZnO nanowires showing the absence of green emission for extracted wires along with a shift in the NBE peak intensity

the wires, the probe diameter becomes negligible when considering the separation of the wires following extraction.

Furthermore, by varying the concentration of the drop casted suspension, isolated nanowires can be separated from the mosaic layer found at the base of nanostructure growth. This allows for direct observations regarding the emission nature of these nanostructures.

Comparison of the CL from the as-grown to extracted wires show a considerable change in the optical properties (Figure 4.22)

There is a redshift in the peak of the NBE luminescence in the as-grown sample of 0.03 eV with respect to the extracted nanowires. This could be due to the presence of tensile strain within the mosaic film, which is highly polycrystalline in nature and contains a significant level of defects as evidenced by the intense observable green emission band. Conversely, the absence of the green emission in the individual nanowires suggests that they have a significantly lower level of defect concentration. These wires do not exhibit an ring or edge luminescence effects as observed in Section

4.3.1, suggesting that band-bending effects are not the dominant cause of green emission near the surface of ZnO nanostructures.

Verification of the origin of the green emission - and its absence in the extracted wires - in the CL was further investigated by reducing the excitation current by two orders of magnitude. The relative intensity of the green region to the NBE remained negligible, indicating that there are no deep-level emissions in the extracted nanowires as a decrease in excitation current would produce a signal if such levels were present. From this, it is possible to conclude that the green emission in this work originates predominantly from the mosaic layer, with the nanowires providing little to no defect emissions.

4.4 Conclusions

The growth of ZnO nanostructures is extremely sensitive to the experimental conditions, and preparing identical samples to a high degree of accuracy requires absolute control over the growth parameters. Minor variation in the growth conditions can have a major effect on the morphological and optical properties of the produced nanostructures.

The growth parameters investigated in this work included growth time, substrate choice, distance from source, carrier gas and seed layers. Of these, the critical conditions were the carrier gas and the relative position of the substrate to the source which are the key methods of controlling the Zn vapour, and growth temperatures respectively.

The optical properties of ZnO structures are dependant on the growth conditions, indicating that there is a relationship between the green defect emission band and the relative oxygen concentration during the growth process, as well as the nature of the seed utilised.

Discrepancies in observations made about the emission properties of ZnO could

be due to the variation in the methods of analysis. If depth is not taken into consideration when performing CL probing, it is highly likely that any data obtained is contaminated with data from a polycrystalline mosaic layer, not just the observed nanostructures.

To maximise reproducibility of growth, the ideal conditions would be under a VLS growth mechanism from an annealed gold film layer, with a carbothermal reduction of ZnO powder under an argon/oxygen gas at low pressures.

Chapter 5

Luminescence properties of plasma-treated ZnO

5.1 A comprehensive review of plasma treated ZnO

The luminescence efficiency of a semiconductor can be substantially affected by surface and bulk defects. Acting as competing recombination channels or non-radiative centres, defects are often undesirable in semiconductor materials destined for optoelectronic device applications. Defects can also prevent the development of suitably doped materials. In the case of ZnO, it is proposed that intrinsic defects are the primary cause of the n-type conductivity observed almost universally across all samples. A critical question often raised relates to the nature of dominant defects acting as donors. Possible defects include residual halogen impurities or Group V elements such as nitrogen in a substitutional role [175] through to intrinsic point defects such as Zn_i and V_O [7].

One method that can be used to investigate the role of defects in ZnO is plasma treatment. This introduces foreign gas dopants to the ZnO crystals, and by comparing the optical properties from samples subjected to different plasma conditions

it is possible to identify the nature of the defects resulting in the different optical emissions.

Plasma processing can functionalise semiconductor surfaces in a variety of ways to increase device performance and stability. One objective of plasma treatment is to remove contamination at the surface of a material by bombarding the area with reactive species, such as the case with a plasma scrubbing system utilised to break down carbon based contaminants into gases such as CO, H₂O, CO₂, O₂ and H₂, which can then be removed via vacuum. Plasma treatment under high radio frequency plasma (RF plasma) conditions can also etch the sample, causing physical modification to the surface. If plasma is being utilised to introduce or remove defects in a sample it is necessary to enhance the efficiency of the modification while minimising the physical impact of the plasma on the surface - structural defects can appear similar to chemically related defects and would thus not contribute significantly to the understanding of intrinsic behaviour.

For ZnO, there are several plasma treatments that could potentially modify the stoichiometric ratios in the material. For the purposes of this work, three were chosen for extended investigation - H₂, O₂, and N₂. Hydrogen, oxygen and nitrogen gases are utilised to generate the plasma environment in this experiment. Hydrogen plasma is expected to cause the incorporation of hydrogen ions into the ZnO lattice to act as donors while passivating deep level defects [176]. Oxygen plasma treatment is expected to neutralise V_O sites in the crystal, reducing the number of defects. Nitrogen was used to investigate the possibility of introducing N_O into ZnO [75, 76].

Each of the plasma treatments will impact the samples differently. As hydrogen behaves as a shallow donor in ZnO [177], rather than acting amphoterically as it does in most semiconductors, this donor-like behaviour of hydrogen in ZnO is considered one of the major hurdles in overcoming the intrinsic n-type nature of the material. Consequently, it is necessary to investigate the incorporation of hydrogen into ZnO so

as to achieve p-type conductivity. Hydrogen has also been shown to kill competitive deep level recombination channels, markedly decreasing green luminescence.

As V_O is one of the possible defects responsible for the green luminescence, oxygen plasma treatment is expected to reduce V_O near the surface of ZnO. The introduction of oxygen to oxygen deficient ZnO is expected to fill V_O and reduce the visible luminescence recombination channel, if the V_O is the origin of the emission.

Nitrogen has been proposed as a shallow acceptor in ZnO [75], but only when acting as a N_O point defect - $(N_2)_O$ (a nitrogen molecule found at an oxygen site in the lattice) has been shown to act as a double-shallow donor [76]. If the behaviour of the N_2 plasma treated ZnO shows the introduction of a stable shallow acceptor, this would suggest the possibility of developing *p*-type ZnO.

First principle calculations have indicated that hydrogen could be the cause of the naturally n-type doping [178] by acting as a donor. Electrical investigations typically report two shallow donors occurring at 30-40 meV and 60-71 meV [179, 180], while low temperature photoluminescence (PL) findings also indicate two shallow defects at 45-47 meV and 53-56 meV [61, 181].

Density functional theory (DFT) based first-principles calculations have shown that shallow donors formed by native defects in ZnO have a relatively high formation energy [51]. Furthermore, DFT theory shows that the only stable charge state of hydrogen in ZnO is as an interstitial non-amphoteric hydrogen donor (H^+) [178].

The location of this interstitial hydrogen has been proposed to occur in one of two locations - either anti-bonded to an oxygen atom or bond-centred between a zinc and oxygen atom. Figure 5.1 shows the possible lattice locations for interstitial hydrogen in ZnO investigated through computational analysis. Van de Walle [178] found that the thermodynamically favourable position for hydrogen in ZnO is at the bond-centred perpendicular location (BC_{\perp} in the figure), and showed that the host atoms of the lattice will relax to accommodate the hydrogen. Experimental work,

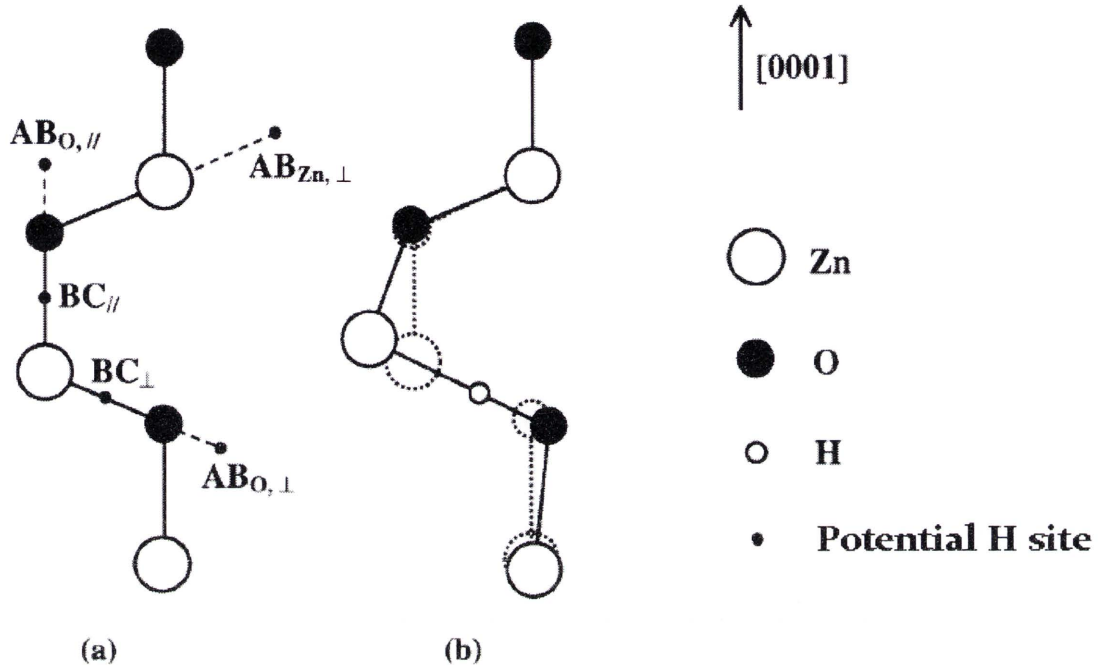


FIGURE 5.1: Schematic of interstitial hydrogen in ZnO. a) shows the possible locations for hydrogen with BC and AB indicating bond-centred and anti-bonded sites respectively, while b) shows the relaxed atomic positions for the host atoms with hydrogen in the BC_{\perp} configuration. Figure adapted from Van de Walle [178]

however, has indicated that the work from Van de Walle [178] may not necessarily be true in all samples. Using infrared spectroscopy, McCluskey et al. [182] concluded that hydrogen was being incorporated in an anti-bonding configuration at 110° to the c-axis ($AB_{O,\perp}$), while Lavrov et al. [183] shows multiple hydrogen bonds existing at BC_{\parallel} (bound to an impurity), $AB_{O,\parallel}$, and a similar result to McCluskey et al. [182] with $AB_{O,\perp}$ at approximately 100° .

As hydrogen is present during growth and processing of ZnO in most situations, the grown samples are exposed to the impurity in almost all preparation methods. Hydrogen is also a fast diffusing species (mobility of approximately $8 \times 10^{-10} \text{ cm}^2 \text{ V}^{-1} \text{ s}^{-1}$) in ZnO [180, 184], thus the understanding of the role of hydrogen in the luminescence properties of ZnO is important for future optoelectronic applications. Defects relating to O_2 and N_2 are also of considerable interest as optoelectronic devices would be exposed to the gases during use. As such, in order to fabricate reproducible stable

p-type ZnO the nature and origin of the intrinsic n-type conductivity first needs to be established and the influence of common impurities needs to be investigated.

The aims of this work are to;

- Develop a suitable methodology for plasma treating ZnO crystals and powders
- Investigate the optical properties of processed ZnO samples
- Identify the defects associated with optical emissions for each ZnO sample

Three different ZnO samples were also used to investigate size, inherent stoichiometry and production method influences on intrinsic defects: single ZnO crystal, 20 nm ZnO powder and ZnO:Zn (zinc doped ZnO) powder.

5.2 Plasma experimental details

Three ZnO products were investigated in the course of this work, as summarised in Table 5.1.

The ZnO single crystals were ultrasonically cleaned in successive washes of acetone, ethanol and deionised water to remove any residual surface contamination before being blow dried with high purity N₂ gas. These were then divided into approximately 2.5 x 2.5 mm squares with a diamond scribe and stored under vacuum until plasma treatment occurred. The ZnO and ZnO:Zn powders were prepared in a similar manner to that described in Section 3.2.6, whereby a suspension of the powder was deposited across a cleaned silicon substrate. As the solvent evaporated, a thin layer of powder was found to adhere to the surface allowing for ease of transport and loading in the plasma chamber.

The plasma parameters were systematically investigated to determine a suitable plasma treatment method by studying the effects of different treatment conditions on the defect emissions in the ZnO:Zn phosphor. Hydrogen was chosen as the

TABLE 5.1: ZnO samples utilised in plasma treatment experiments

Sample	Source	Fabrication method	Known impurity levels (wt%)
ZnO:Zn phosphor	Phosphor Technology, England	*	*
ZnO powder	Antaria Limited	Mechanochemical-processing	< 1% Mg: <0.0005 Al: <0.0030 Si: \approx 0.0030 Ti: \approx 0.0010 Cu: <0.0030 Fe: <0.0050 Ca: <0.0005 Ag: <0.0002
ZnO single crystal	MTI Corporation	Hydrothermal	

* Information not publicly available - trade secret

investigative plasma as it has been shown to readily modify the optical properties of ZnO.

The ZnO:Zn phosphor samples were subjected to several plasma treatment conditions as summarised in Table 5.2. Sample temperatures wer held at 200°C, and the H₂ flow was kept constant across all samples. The hydrogen is typically expected to act on the defects in ZnO in one of two ways; either passivating the green deep level emission (DLE) resulting in enhancement of the near band-edge (NBE) [185, 186], or as a reducing agent, inducing further V_O in the sample. Typical scans for each

TABLE 5.2: Summary of hydrogen plasma treatments for Zn doped ZnO

Sample	Treatment time	RF Power	
Sample A	10 minutes	N/A	H ₂ flowing but no plasma ignition
Sample B	10 minutes	15 W	
Sample C	20 minutes	15 W	
Sample D	20 minutes	30 W	

of the samples can be found in Figure 5.2. Increasing the plasma treatment time

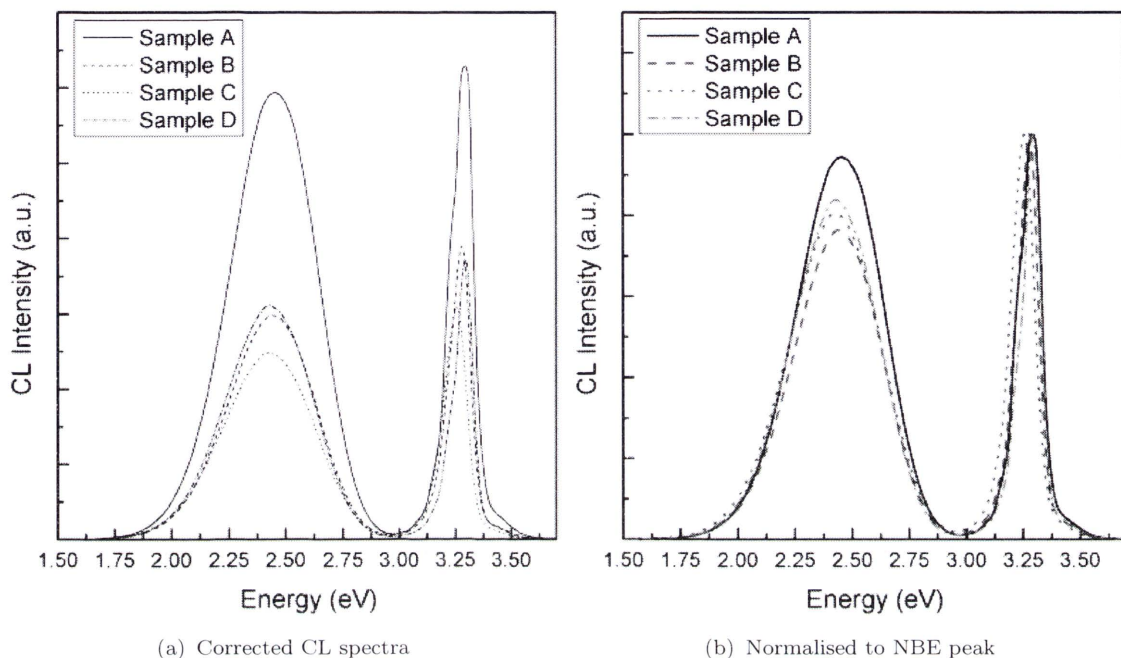


FIGURE 5.2: CL Spectra obtained from plasma treated ZnO:Zn phosphors A-D as described in Table 5.2. Accelerating voltage was held at 5 kV, current at 50 nA with a field of view of 120 μm

does not significantly influence the results, nor does increasing the RF power of the plasma, as evidence by the similarity of the results obtained utilising the methods for Sample B. As the results for Sample B are similar to those obtained from greater time periods or higher RF powers, there was no need to perform longer or more aggressive plasma treatments. Furthermore, by minimising the RF power and treatment time, the likelihood of surface damage through physical etching of the ZnO samples is reduced. The plasma operating parameters obtained for plasma treating ZnO in this manner are within the values reported in the literature, tending towards the less destructive plasma conditions.

The ideal plasma chamber operating parameters were established as:

- Sample temperature 200°C
- Gas flow rate 10 sccm

- Plasma RF power 15 W forward bias
- Treatment time 10 minutes

The plasma chamber used in this work can be seen in Figure 5.3.

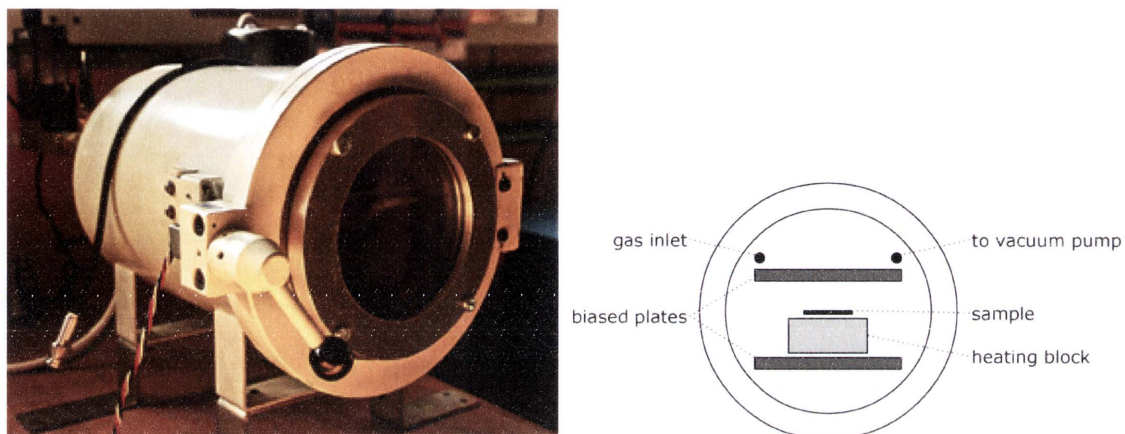


FIGURE 5.3: Image (left) and schematic (right) of plasma chamber used to treat ZnO identifying key features

During the treatment, the gas flow rate and sample temperature were kept constant. The reactant gas was leaked into the chamber through a mass flow controller, and temperature and chamber pressure were controlled and monitored by a computer running a custom LabView program.

As the temperature used throughout the plasma treatment process is maintained at 200°C or below, it is not expected that any intrinsic defects will form as the sample remains well below the temperature required for introduction of further intrinsic defects (see Table 2.2, noting that $k_B T \approx 0.041$ eV at 200°C).

5.3 Plasma treatment of ZnO:Zn phosphor

The ZnO:Zn phosphor was subjected to the three plasma conditions - H_2 , O_2 and N_2 plasmas. All conditions, other than gas, were kept constant throughout the

plasma treatments. The cathodoluminescence (CL) emission for each of the plasma treatments, as well as an untreated sample, can be seen in Figure 5.4.

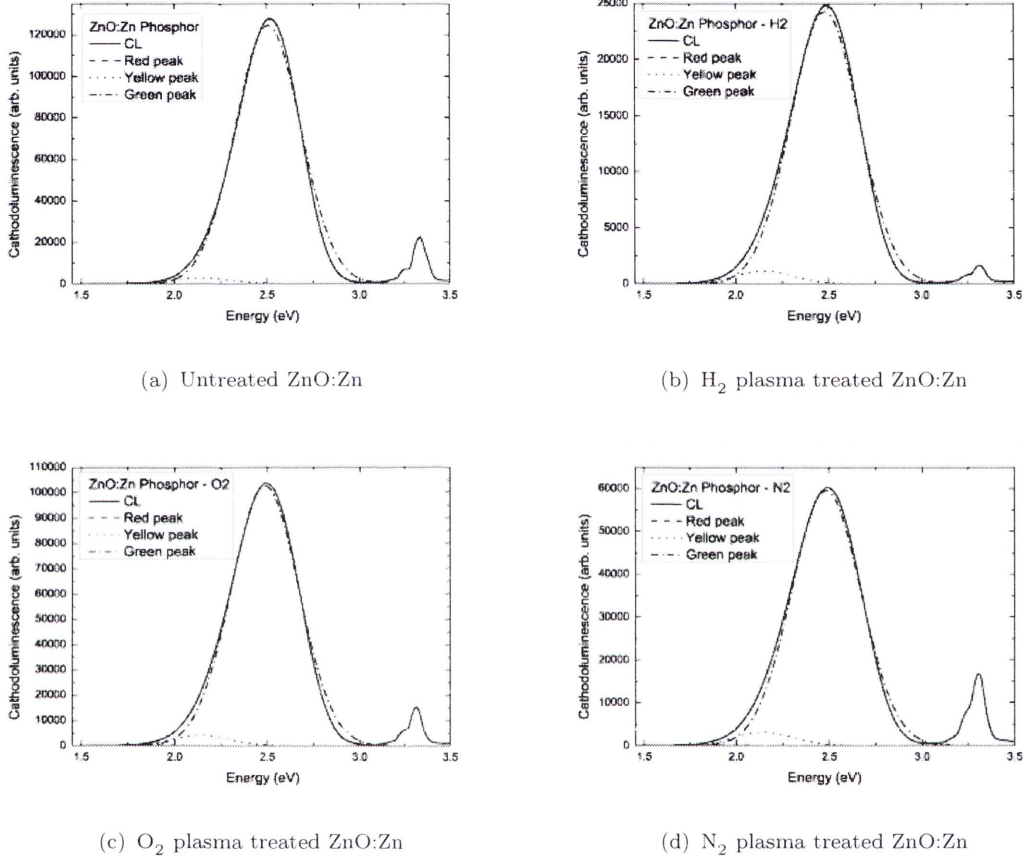


FIGURE 5.4: CL emissions from plasma treated ZnO:Zn. Accelerating voltage was held at 15 kV, beam current at 0.4 nA

The defect component of the CL spectra were fitted with three gaussian peaks centred at 1.7 eV, 2.15 eV and 2.48 eV with constrained full width at half maximum (FWHM) values (0.22-0.25 eV). These peaks have been chemically identified as corresponding to V_{Zn}^x [187], Li_{Zn} [88, 188] and V_O [56] respectively. As can be seen in the figures, the contribution from red 1.7 eV peak is negligible throughout the range of plasma treatments, while the 2.15 eV contribution varies only very slightly. The majority of the signal (in excess of 90% of the total defect emission) comes from the 2.48 eV V_O peak. The plasma treatment can change the ratio of the defect luminescence to the band edge significantly, as shown in Table 5.3, where treatment

TABLE 5.3: Fitted peak values for plasma treated ZnO:Zn phosphor

Conditions	Relative intensity (% total defect emission)			Approximate UV:Defect ratio
	V_{Zn}^x	Li_{Zn}	V_O	
Untreated	0.18	5.07	94.75	0.3
Hydrogen	0.16	4.46	95.38	0.1
Oxygen	0.26	5.58	94.16	0.2
Nitrogen	0.08	2.72	97.20	0.4

under hydrogen plasma will enhance the defect emission, reducing the UV:Defect ratio, while under nitrogen conditions the defect related emission will reduce slightly, improving the UV:Defect ratio. Plasma treating under oxygen conditions shows no significant variation in the relative peak intensities.

The ZnO:Zn phosphor is expected to contain a non-stoichiometric ratio of Zn to O, so it is unsurprising to observe a significant number of V_O present, as evidenced by the domination of the defect peak by the 2.48 eV emission. The significant overall reduction in the CL emission for the hydrogen treated sample, and the moderate reduction in the nitrogen sample, indicate a passivation of the defect responsible for the 2.48 eV peak, or the introduction of more efficient recombination channels as a result of the foreign species incorporation. The observation that the nitrogen changes both the defect and the band edge emission line shapes would suggest that the nitrogen has incorporated as either N_O or N_2O , and is acting as a shallow donor to offer a bound-excitonic recombination channel. The reduction of the defect peak as a result of hydrogen treatment agrees with literature, however this is usually accompanied by an subsequent enhancement of the near band edge emission, which does not occur in this case. The lack of impact from the oxygen plasma on the CL spectra indicates that the plasma species was either too reactive to adequately replenish the missing oxygen atoms in the phosphor, or that the defect at 2.48 eV is not affected by an introduction of oxygen atoms.

5.4 Plasma treatment of ZnO powder

Similar results were obtained for ZnO powder under identical treatment conditions. Two of the fitted gaussian peaks were the same as those from the ZnO:Zn phosphor, however the 2.48 eV peak was found to be replaced by a 2.55-2.6 eV peak. This peak has been identified as a V_{Zn} [187]. Fitted CL plots can be found in Figure 5.5 and summarised in Table 5.4 As can be seen from both the figures and the table, the

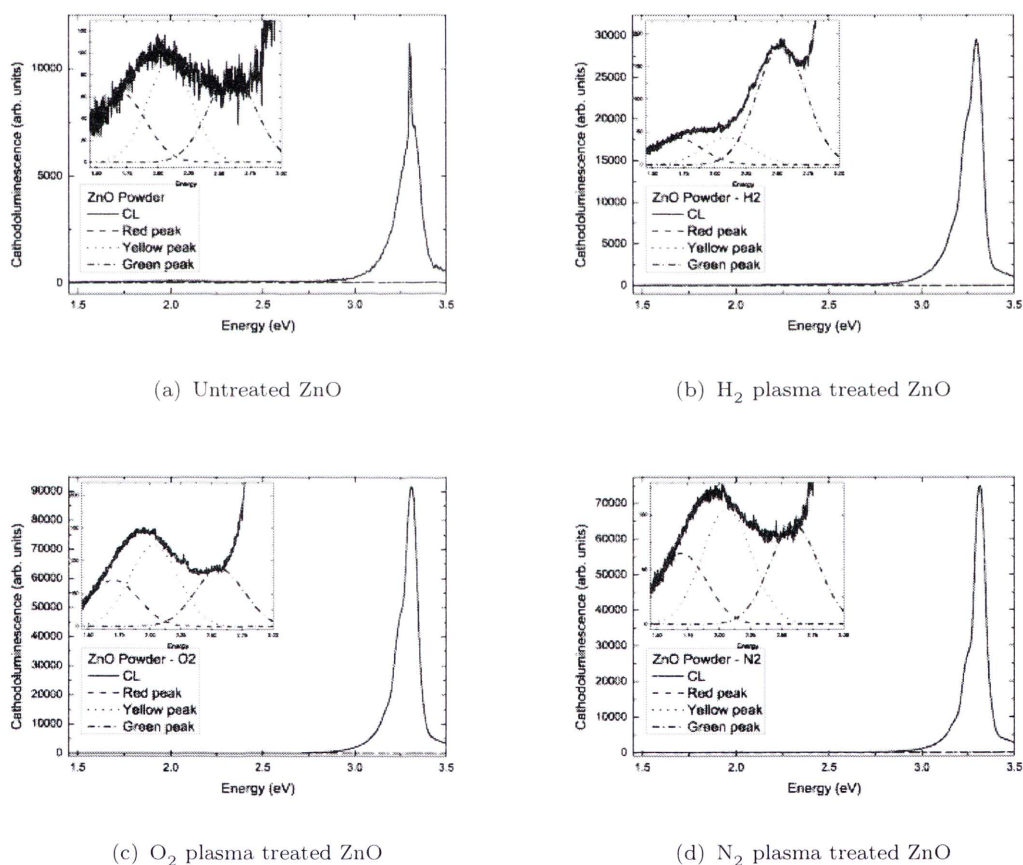


FIGURE 5.5: CL emissions from plasma treated ZnO powder. Accelerating voltage was held at 15 kV, beam current at 0.4 nA. Insets show rescaled defect regions for clarity.

CL line shape varies significantly depending on the nature of the plasma treatment. Furthermore, as the UV is now the dominant feature of the CL spectrum, it is more practical to use the UV:Defect ratio as a measure of variation between treatments.

TABLE 5.4: Fitted peak values for plasma treated ZnO powder

Conditions	Relative intensity (% total defect emission)			Approximate UV:Defect ratio
	V_{Zn}^x	Li_{Zn}	$V_{Zn'}$	
Untreated	39.55	40.00	20.46	34
Hydrogen	23.43	19.49	57.08	90
Oxygen	31.25	47.94	20.81	174
Nitrogen	32.25	44.64	23.11	160

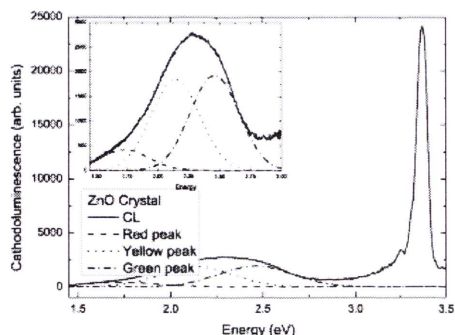
The plasma treatments all enhance the UV emission relative to the defect, with oxygen and nitrogen having similar results. The point of significant interest is in the hydrogen treated sample. The 2.55 eV peak is enhanced relative to the other defect components when compared to the other two treatments and the untreated samples. The oxygen and nitrogen also enhance the 2.15 eV peak slightly relative to the untreated sample.

5.5 Plasma treatment of ZnO crystals

ZnO crystals were treated in the same manner with the results presented in Figure 5.6 and Table 5.5. The peaks were again fitted with 3 gaussians, however the green peak was found to vary between 2.44 eV and 2.6 eV depending on the treatment of the sample, indicating the presence of two different defects, namely the V_O and $V_{Zn'}$ respectively.

TABLE 5.5: Fitted peak values for plasma treated ZnO crystal

Conditions	V_{Zn}^x	Relative intensity (% total defect emission)			Approximate UV:Defect ratio
		Li_{Zn}	V_O	$V_{Zn'}$	
Untreated	14.18	48.31	37.52		5
Hydrogen	30.55	62.09		7.36	9
Oxygen	14.03	48.42	37.55		3
Nitrogen	29.10	58.27		12.66	10



(a) Untreated crystal

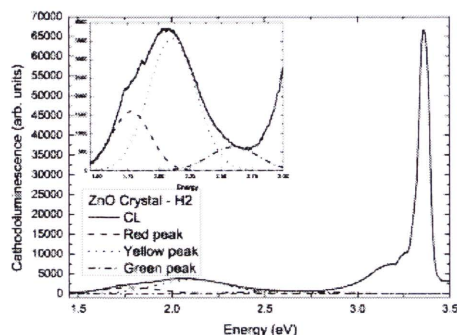
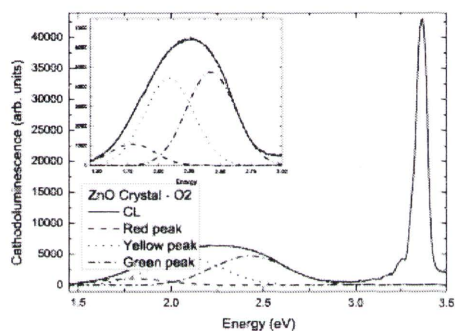
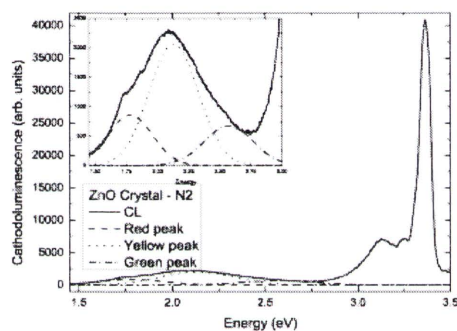

 (b) H_2 plasma treated crystal

 (c) O_2 plasma treated crystal

 (d) N_2 plasma treated crystal

FIGURE 5.6: Comparison of CL response for ZnO crystals subjected to different plasma treatment methods. Collected at 15 kV, 0.4 nA, 8,000x. Insets show rescaled defect regions for clarity.

The hydrogen sample shows a significant reduction in the green peak component of the defect emission when compared to the untreated sample, while enhancing the 1.7 eV peak. The nitrogen treated sample exhibits similar behaviour to the hydrogen, while the oxygen plasma treatment appears not to vary from the untreated sample.

One advantage of utilising a single crystal over the powder or phosphor in this experiment is the ability to perform depth resolved CL investigations. From depth-resolved cathodoluminescence (DCL), it is possible to calculate the penetration depth and influence the plasma treatments have on ZnO.

Typical depth resolved plots of the crystal under different plasma conditions can be seen in Figure 5.7.

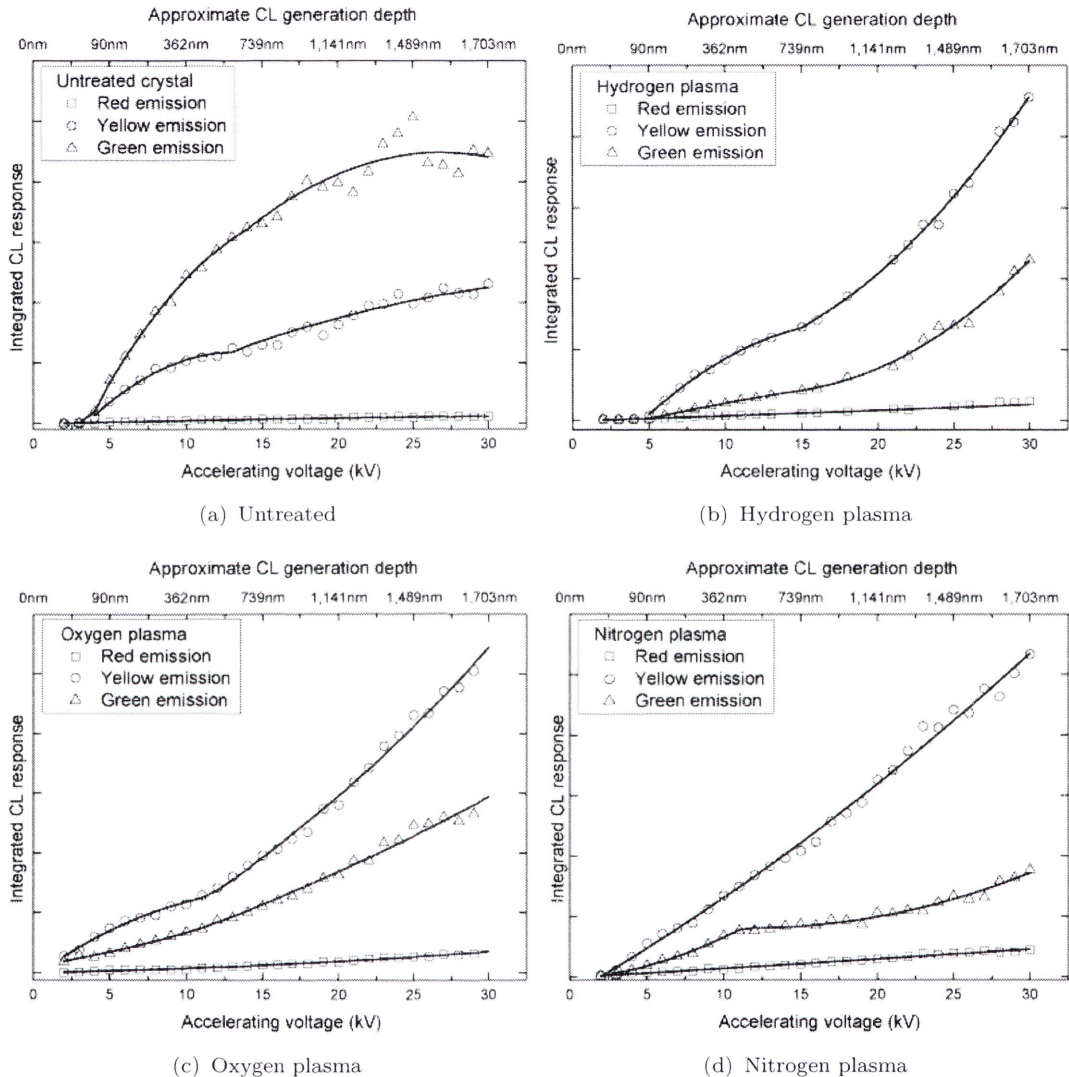


FIGURE 5.7: Depth resolved plots for ZnO crystal subjected to different plasma conditions. Each fitted curve was integrated to find the total CL intensity contribution to the defect emission peak; the Red emission represents the 1.7 eV peak, the Green the 2.4-2.6 eV peak and the Yellow is the 2.15 eV peak. Guide lines have been added to aid the reader.

An interesting point to note is the observation of a non-ideal CL signal. There is variation in the exciton density as higher accelerating voltages produce larger interaction volumes, but given that a constant power is being used to excite the crystal it is expected that an equal number of electron-hole pairs will be generated

at each scan. In this ideal scenario, a horizontal line for the integrated intensity is expected for each of the fitted curves, assuming a homogeneous distribution of the defect centres responsible for the luminescence. The non-linearity observed in the green emission for the untreated crystal in Figure 5.7 for voltages below 25 kV suggests that there is substantial variation in the crystal quality near the surface.

As can be seen in the figures, plasma treatment, regardless of the plasma choice, significantly alters the relative component intensities of the defect peak. The untreated crystal exhibits a small dead layer near the surface approximately 100 nm for all the peaks. After this dead layer, the non-linear increase in the yellow and green defects suggest the presence of polishing related defects or surface charge effects affecting the optical properties of the crystal up to 2 μm deep. The red emission does not increase significantly, irrespective of the penetration depth of the electron beam. The green emission initially increases rapidly before beginning to taper off approximately 2 μm into the crystal. The yellow peak shows a near linear increase with penetration depth after approximately 12 kV.

In comparison, the hydrogen plasma treated crystal shows a marked decrease in the green emission. The green peak is significantly suppressed up to a depth of approximately 2 μm , where it begins to increase again. The yellow peak has a similar line shape to that of the untreated sample, however also shows a slight suppression up to the 2 μm depth, after which it increases linearly. Again, the red peak showed little deviation from a linear fit.

The nitrogen plasma sample showed similar results to the hydrogen with the green peak being markedly suppressed. The difference however is that after 800 nm the green emission plateaus for approximately 1 μm , after which it resumes a linear increase. The yellow peak intensity can be fitted with a linear guide line, as can the red emission which shows no significant variation from the preceeding samples.

The oxygen sample is unique in that no dead layer is observed for any of the defect peaks. Again the green is suppressed below the yellow emission, however it exhibits

a near linear increase with greater penetration depth. The yellow emission has two distinct rates of increase - slow up to approximately 700 nm and then a rapid linear increase from there onwards. The red emission also shows a slight shift in rate of increase after the 700 nm depth.

The variation between the rate of increase in each peak emission can be used to confirm the identity of the governing defect centre that was previously assigned.

5.6 Summary of plasma results

5.6.1 ZnO:Zn phosphor

The key result observed from this sample is the prevalence of the strong 2.48 eV peak. As the stoichiometric ratio is weighted in favour of Zn (the phosphor is of the form Zn_xZnO , where $x > 0$), the likely intrinsic defects are either V_O or Zn_i . Literature reports place these defects at approximately 2.4 and 1.7 eV respectively. Given that there is no significant 1.7 eV peak in any of the ZnO:Zn phosphors, it can be concluded that the contribution from the excess zinc in the phosphor is forming V_O point defects, which in turn are causing the massive green emission at 2.48 eV. The CL line shape does not notably vary between the plasma treatments, suggesting that the excess zinc atoms, and thus excess V_O defects, are not reduced significantly by the comparatively low-level plasma modification. An interesting point of note is the reduction in the intensity of the defect related emission for the hydrogen treated sample in comparison to the two other plasma treatments. Literature reports show that hydrogen will drastically reduce, if not eliminate, the CL defect emission from ZnO samples, along with a significant enhancement of the UV emission. In this sample, only the reduction of the green is observed. This would indicate that while the hydrogen plasma is passivating a large number of otherwise efficient recombination channels, the large Zn:O imbalance requires more passivation

than mildly O deficient samples. Furthermore, hydrogen may not be able to act as a shallow donor in Zn rich crystals, thus preventing the UV recombination channel from becoming more preferable. The stability of the 2.15 eV contributions across the untreated and treated samples indicate that the corresponding defect responsible for the emission is not affected by the plasma treatments.

5.6.2 ZnO powder

In contrast to the 2.48 eV dominance in the ZnO:Zn results, the each of the three fitted peaks makes a noticable contribution to the overall defect emission. The first point of note is the relocation of the 2.48 eV peak to a 2.55-2.6 eV. This new location corresponds to a V_{Zn} rather than a V_O , suggesting that the defects observed in the ZnO powder has a different chemical origin to that of the ZnO:Zn. For the untreated sample, there is little contribution from the V_{Zn} peak, with roughly equal contributions from the 1.7 eV and 2.15 eV defects (1:2:2 approximate respective ratios). Following H_2 plasma treatment, the relative contributions between the three peaks is reversed (2:1:1 ratio), indicative of either passivation of the red and yellow components, or an enhancement of an efficient recombination channel at 2.55 eV. As hydrogen is the only plasma treated sample to show this effect, the enhancement of the 2.55 eV peak must be related to the nature of the plasma itself. This would contradict literature suggesting the formation of non-radiative hydrogen-zinc vacancy complex centres following hydrogen plasma treatment. A further interesting point of note is the relative enhancement of all the treated samples in terms of the UV:Defect ratio. Hydrogen is typically noted for its immense relative enhancement of the UV peak, however in this work the oxygen and nitrogen plasma samples have almost twice the relative enhancement. This could be due to the unexpected increase in the 2.55 eV peak for the hydrogen. The oxygen and nitrogen plasma treatments show similar line shapes to the untreated powder, however the nitrogen does show a slightly higher relative intensity in the 2.55 eV peak.

5.6.3 ZnO crystal

The crystal results suggest that the oxygen plasma treatment will have no significant effect on the overall CL defect emission when compared to the untreated sample. The hydrogen and nitrogen plasmas both enhance the 2.15 eV peak while suppressing the more green region of the defect emission. For the first time in this work, the hydrogen has behaved close to as expected, reducing the overall green intensity while enhancing the UV emission to a ratio similar to that of the nitrogen results.

The depth profiling achieved with the crystals also sheds light on the effectiveness of the different plasma conditions. From the untreated crystal, it is clear that the dominant peak throughout the crystal is the green ≈ 2.4 eV peak, with the yellow 2.15 eV peak contributing a similar component near the surface of the crystal, where its rate of increase drops after approximately 400 nm penetration. The red luminescence remains near constant, regardless of depth.

The introduction of the hydrogen plasma results in a dead layer of approximately 90 nm forming, and based on the variations in the rate of change of integrated intensities, it is possible to conclude that the hydrogen was able to incorporate into the ZnO to a depth of approximately 800 nm. This is in contrast to the oxygen plasma which shows an estimated incorporation depth of 400 nm, again based on the change in the line shapes obtained. The nitrogen plasma shows no obvious incorporation depth value, however the reduction of the green emission - observed in all three plasma treated samples - suggests that the nitrogen is altering the defects involved in radiative recombination in some manner.

5.7 Conclusions

The variance between the defect observations obtained in this work highlight the difficulties associated with presenting a single answer to defect identification within

ZnO samples. As different samples can be produced by different processes and subjected to different post-processing methods, variations in the defect structure and impurities can be expected.

Across the plasma treated undoped ZnO samples, hydrogen has shown an enhancement in the NBE relative to the defect peak. This is due to hydrogen acting as a shallow donor in ZnO, as well as forming non-radiative complexes with deep level defects. The expected enhancement for the ZnO:Zn phosphor is not observed. This could be due to the hydrogen forming a H-Zn complex that acts as a NBE luminescence killer.

The oxygen plasma treatments significantly enhanced the UV:Defect ratio for the powder, further supporting the observation that the primary defect causing green luminescence is an oxygen vacancy. For the crystal, there was no change in the ratios of the relative peaks, and a slight reduction in the UV:Defect ratio. This would indicate that the incorporation of an oxygen plasma into a bulk crystal is not as effective as incorporation into a powder, owing to the size of the oxygen ion. Interestingly, for the ZnO:Zn phosphor, there was no significant enhancement, which suggests that the excess Zn imbalance could not be rectified by the incorporation of oxygen through plasma treatment. In comparing the oxygen treated sample to the reference, the minor variations between the two can be attributed to variations between sample mounting and probing conditions.

The nitrogen plasma was the only treatment to show an overall UV:Defect ratio enhancement in all three samples. Nitrogen (N^-) can act as an acceptor, forming a donor-acceptor pair with V_O . This would produce another competitive recombination channel, and could explain the appearance of a new peak near the NBE emission observed in the crystal sample.

The assignment of the peaks as oxygen and zinc vacancies would appear to be valid based on the results obtained in this work. The non-involvement of the 2.15 eV peak is consistent with the assignment of an impurity - tentatively identified as Li -

as none of the plasma treatments would be likely to form a complex or replace the lithium under these treatment conditions. The suggestion that this peak could be assigned to a hydroxyl group at the surface [189] is possible, however as the yellow peak is observed in both the ZnO powder and crystal in my work and does not follow the behaviour observed by defect-emissions involving hydroxyl groups, it is possible to conclude that the hydroxyl emission origin does not apply to these samples. It is possible to enhance the UV emission properties of both ZnO powders and crystals using plasma treatment, however the ZnO:Zn phosphor shows minimal response to low power plasma irradiation.

Chapter 6

Transition metal doping of ZnO

6.1 An overview of transition metal doped ZnO

The introduction of an impurity into a semiconducting material is one of the key methods of controlling its properties, such as electrical conductivity. Bulk semiconductors are routinely subjected to doping and in recent times it has become more prevalent in nanoscale semiconductors as well. It has been found that the introduction of transition metals to semiconductors can result in the creation of a new class of materials commonly referred to as dilute magnetic semiconductors (DMSs). In these semiconductors, exchange interactions between the electrons in the semiconducting band and the localized electrons at the magnetic impurities lead to a number of interesting properties. Unfortunately, the initial DMSs were found to have low Curie-temperatures, resulting in a lack of reproducibility in their magnetic properties and significant controversy over their origin. It was in 1986 when Story et. al demonstrated that the ferromagnetic Curie temperature of Mn^{2+} doped $\text{Pb}_{1-x}\text{Sn}_x\text{Te}$ could be controlled through carrier concentration [190]. Out of all the transition metals (TMs), the Mn doping of ZnO is most favourable because Mn has the highest possible magnetic moment [191] and also the first half of the d-band

is full, creating a stable fully polarized state. Introducing Mn to binary semiconductors has resulted in extensive research on the ternary II-VI based DMSs that occur in the form $A_{1-x}^{II}Mn_xB^{VI}$. The ternary composition provides the possibility of tuning the structural and electronic parameters of the semiconductor, enabling band gap engineering [192]. In addition, the strong exchange interactions between the sp band electrons and the d electrons associated with the Mn give rise to giant Faraday rotation and magnetic field induced metal-insulator transitions [192].

A DMS based on ZnO would be of significant benefit owing to the widespread potential applications in spintronic devices. Theoretical work focussing on Mn-ZnO has also shown that it is theoretically possible to produce p-type ZnO with a T_c greater than 300K, but this is yet to be confirmed experimentally.

One aspect that remains uncertain is the mechanism behind the ferromagnetism in doped wide band gap semiconductors. Moreover, the magnetisation obtained experimentally is lower than that predicted theoretically for the majority of the literature.

Dietl [193] has developed a theory which suggests that charge carriers are required to mediate the magnetic coupling of manganese dopants in Mn_2^+ doped GaAs. If there is an insufficient hole concentration in the magnetic semiconductor, it would exhibit a low Curie temperature or paramagnetism. A higher hole concentration, however ($> 10^{20}cm^{-3}$) would result in a Curie temperature between 100 and 200K for GaAs, or above 300 K for ZnO and GaN.

As briefly mentioned before, the introduction of impurities does more than just produce changes in the magnetic properties for ZnO.

Band gap manipulation of ZnO can be achieved through doping with a TM such as cadmium or manganese, or alkaline metals such as beryllium or magnesium. Band gaps have been reported at ranges from 3.04 eV (9.1 atomic% Cd) to 3.99 eV (16.8 % Mg) [13].

TABLE 6.1: Oxidation and charge states of Mn and Fe

Charge state	3 d ³	3 d ⁴	3 d ⁵	3 d ⁶
Acceptor				Mn ¹⁺
Neutral			Mn ²⁺	Fe ²⁺
Donor		Mn ³⁺	Fe ³⁺	
Double donor	Mn ⁴⁺	Fe ⁴⁺		

Incorporation of metals with a different atomic radius to Zn into the crystal can also induce changes to the lattice parameters, and in some cases change ZnO from hexagonal wurtzite to a cubic or zincblende crystallographic system. A TM can also induce defects in ZnO as a result of the Zn lattice site substitution. Defects such as Zn_i and V_O can be formed as a result of the lattice strain, or in an effort to charge compensate for heterovalent dopants. These point defects can act as donors and are often incorrectly identified as directly related to TM impurities.

Transition metal impurities in ZnO typically occupy the Zn site and behave as donors. The possible oxidation and charge states of the two transition metals of interest in this work can be found in Table 6.1. The acceptor levels of Mn and Fe are found above the valence band edge in ZnO and thus do not contribute to p-type conductivity but can act as deep donors in optical transitions. Mn is typically considered the likely cause of deep electron traps in ZnO [194, 195], but also acts as a donor in its 3+ state. Typically, incorporation of TMs are accepted as existing in their 2+/3+ state, acting as neutral impurities and donors [196].

This chapter examines TM doped ZnO, specifically the effects of doping on the optical and structural properties of the host material.

6.2 Manganese doped ZnO

Studies have recently shown that the incorporation of Mn into ZnO offers a possible route to produce p-type ZnO [197], along with the potential to realise a multifunctional material with interesting semiconducting and optical properties, resulting in devices such as UV detectors and light emitters. Furthermore, it has been shown that Mn-doped ZnO could act as a DMS with a transition temperature (T_c) greater than 300 K [193, 198], which is a vital property for the production of various room temperature electromagnetic devices. Mn^{2+} has the highest solubility of any transition metal in bulk ZnO, and reaches approximately 25% at 800° [199], with reports of levels up to 35% through the use of nonequilibrium pulsed laser deposition film growth processes [200].

6.2.1 Manganese doped ZnO crystal

Mn impurities can be introduced into ZnO crystals in a variety of methods, either during growth or as a post growth treatment. Successful incorporation of Mn into ZnO has been achieved during growth through pulsed laser deposition, hydrothermal [201], electron spin resonance, or vapour phase transport methods [202]. Post growth treatments include ion implantation and the method chosen for this work - in-diffusion. ZnO nanorods have been successfully doped with TMs through thermal diffusion, and the results show that the TM ions incorporate into the ZnO host lattice sites [132]. In-diffusion has been selected for this work as it offers highly reproducible experimental conditions, and the doping concentration can be adjusted easily by altering the length of time of diffusion and thickness of the TM thin film.

Samples were prepared using the method in Section 3.1.4.1 for diffusion times between 0 and 40 hours. Verification of the diffusion of the TM into the crystal was obtained using EDX as shown in Figure 6.1. The EDX results show no detectable

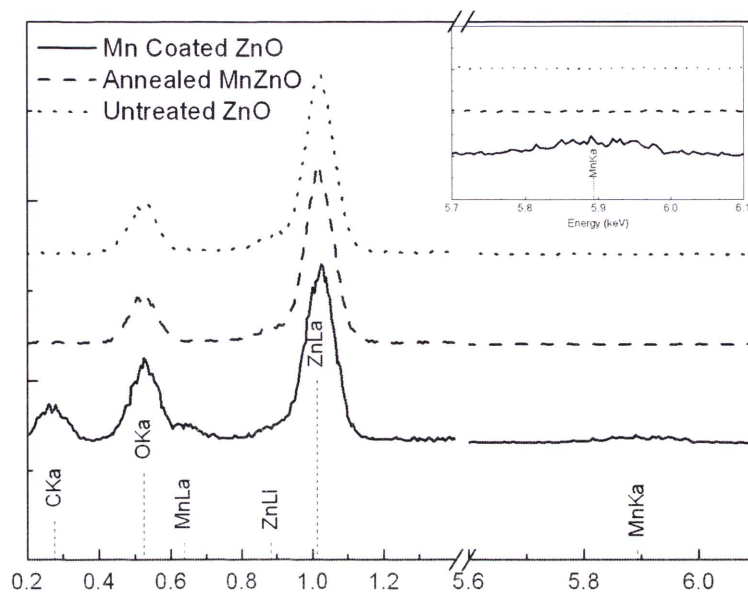


FIGURE 6.1: EDX plot of pre- and post- annealed Mn-coated ZnO along with as received ZnO and label markers. Inset shows annealing the Mn coated ZnO causes the $K\alpha$ peak associated with Mn to disappear. Carbon impurities occurred during preparation but were reduced during annealing.

residual Mn on the surface of the ZnO crystal following annealing as the Mn $K\alpha$ peak is no longer visible.

Previous studies have shown the incorporation of Fe into ZnO crystals without the formation of metallic clusters [131], and it is expected that Mn will substitutionally replace Zn atoms in the lattice in a similar manner. As the cathodoluminescence (CL) signals generated across the surface of the annealed crystals is uniform, this supports the hypothesis that Mn clustering does not occur during this doping process.

A similar annealing treatment was used to produce ZnO crystals without Mn in-diffused to act as a reference for the different annealing times.

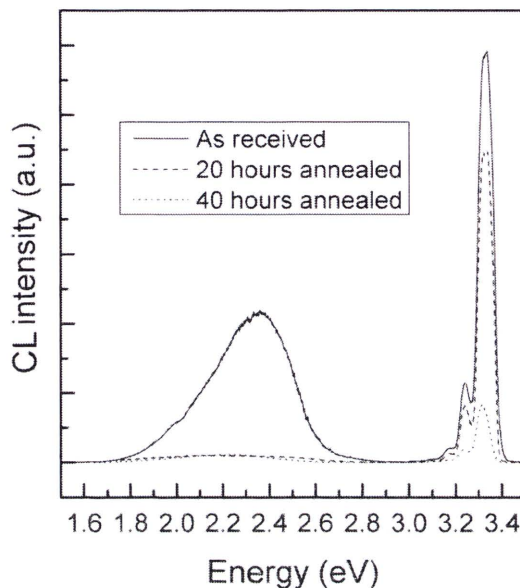


FIGURE 6.2: CL spectra of Mn doped ZnO single crystals annealed for 0, 20 and 40 hours. Spectra obtained at 30 kV accelerating voltage, 15 nA beam current, 30 μm field of view

6.2.1.1 Analysis of Manganese in-diffused ZnO

Manganese in-diffused ZnO was examined using CL techniques, namely depth-resolved cathodoluminescence (DCL) and power-density resolved cathodoluminescence (PDCL) (for further details see Sections 3.2.1.2 and 3.2.1.3 respectively), which show that the incorporation of Mn into the crystal changed the luminescence properties when compared to that of the reference annealed ZnO crystal. The room temperature CL comparison spectra of the different annealing times can be seen in Figure 6.2. It can be seen that annealing of the coated ZnO crystal initially results in a significant quenching of the CL emission in both the near band-edge (NBE) and deep level (DL) regions, supporting the suggestion that Mn acts as an effective luminescence killer [203–205] by providing an alternative recombination path through the formation of a complex with intrinsic non-radiative centres. At higher concentrations, Mn also has been shown to strongly quench band-edge luminescence in ZnO [206, 207].

It should be noted, however, as CL does not provide an absolute value for the Mn

TABLE 6.2: Integrated areas of the NBE and deep level peaks for Mn doped ZnO at different annealing times. 30 kV accelerating voltage, 3.3 nA beam current

Annealing time (hours)		NBE integrated area (a.u.)	DL integrated area (a.u.)	$\frac{I_{NBE}}{I_{DL}}$
0	Uncoated	2,500	29,000	0.085
20	Uncoated	68,000	204,000	0.332
	Coated	20,000	13,000	1.582
40	Uncoated	1,100	32,000	0.035
	Coated	53,000	42,000	1.252

concentration from the emission intensities obtained, it is only possible to produce qualitative rather than quantitative observations between the samples.

To compare the relative intensities of the NBE to the DL emission, the area under each peak is integrated, with the resolvable peaks defined as 1.8 to 3.0 eV for the DL and 3.0 to 3.5 eV for the NBE. The broad DL peak is composed of several components, namely the 2.5 eV green and 2.2 eV yellow peaks, and occasionally the 1.75 eV orange-red peak. These peaks are normally assigned to V_O , Li_{Zn} and V_{Zn} respectively. The integrated intensities of components for the different samples can be seen in Table 6.2. The results shown in Table 6.2 indicate that the coating of Mn on ZnO significantly enhances the NBE:DL intensity ratio for emissions from deep traps within the crystal. Results from near the surface of the crystal serve to illustrate the influence of Mn on ZnO emission. While there is some enhancement of the ratio due to annealing out of structural defects (as evidenced in the emission improvement from that of the uncoated crystals), there is significant change in the near-surface emission as a result of Mn incorporation. Table 6.3 shows that Mn diffusion into the crystal for 20 hours will quench both the NBE and DL emission, but the DL is reduced by a far greater level. The initial relative increase in the $I_{NBE}:I_{DL}$ ratio can be attributed to the increase in the incorporation of the Mn ions into the ZnO crystal as a function of annealing time, prior to acting as a luminescence killer when its concentration exceeds a critical level. This is best visualised through Figure 6.3, showing the reduction in defect emission (and thus increase in the NBE:DL ratio) following 20

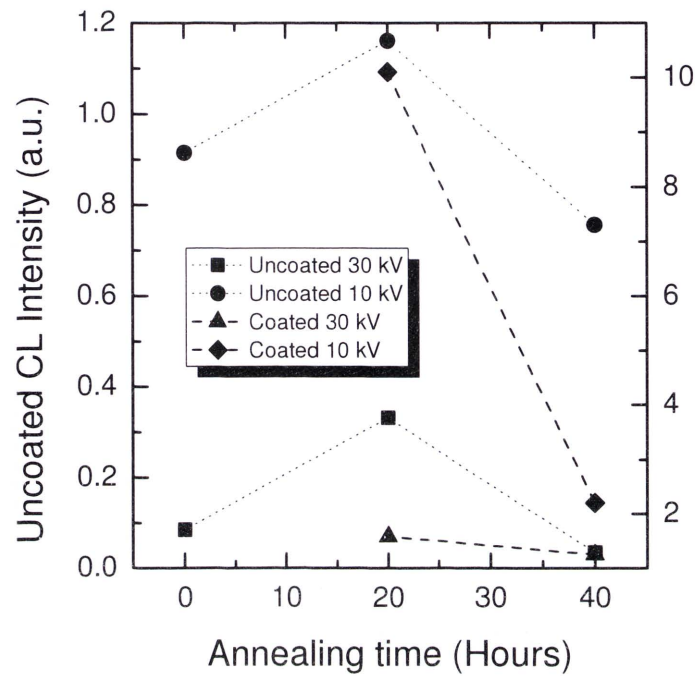


FIGURE 6.3: Relative intensity ratios of NBE and DL for Mn coated and uncoated ZnO crystals as a function of annealing time

TABLE 6.3: Integrated areas of the NBE and deep level peaks for Mn doped ZnO at different annealing times. 10 kV accelerating voltage, 10 nA beam current

Annealing time (hours)		NBE integrated area (a.u.)	DL integrated area (a.u.)	$\frac{I_{NBE}}{I_{DL}}$
0	Uncoated	6,700	7,200	0.915
	Coated	64,000	55,000	1.161
20	Uncoated	27,000	2,600	10.105
	Coated	5,500	7,300	0.757
40	Uncoated	21,000	9,600	2.202
	Coated			

hours annealing for the uncoated sample. Both the coated and the uncoated samples show a reduction in the ratio following further annealing, suggesting that different defects are being produced through extended thermal treatment. The significant reduction in the NBE:DL ratio observed in the 10 kV coated sample suggests that the Mn diffusion through the crystal had not reached deep enough into the crystal to act as a luminescence quencher. This is supported in the observation of the subsequent decrease in the ratio obtained following further annealing.

6.2.2 Manganese doped nanoparticles

Doped ZnO powders were produced via wet chemistry methods (provided by Dr. Takuya Tsuzuki, Centre for Material and Fibre Innovation, Deakin University, Victoria) with nominal Mn atomic percentages ranging from 0 to 3 atomic %. The powders consisted of 100-200 nm aggregates of the primary particles and exhibited a visible change in colour from white to beige with increasing Mn concentration.

The synthesis of the undoped ZnO particles was conducted via:



The sodium carbonate was added to hydrated zinc acetate to form a white precipitate. These were extrated from the supernatant using a centrifuge and washed with deionised water. The precipitates were then air dried at 60°C before heat treatment at 350°C for one hour. This reduces the zinc carbonate to ZnO with the CO₂ dispersing to the atmosphere. Mn-doped ZnO particles were prepared in a similar manner, adding up to 3 mol% of Mn(CH₃COO)₂·4H₂O to the zinc acetate prior to addition of the sodium carbonate.

6.2.2.1 XANES analysis

To confirm the presence of incorporated Mn in the ZnO powders, x-ray absorption near edge structure (XANES) was performed, specifically looking at the Mn L edge.

As can be seen in Figure 6.4, the Mn L edge is observable in the doped powders. Furthermore, the coordination state of the Mn in doped ZnO powders prepared using the sol-gel process described previously is confirmed as exclusively Mn²⁺. This supports Mn acting as an isovalent substitution at a Zn site.

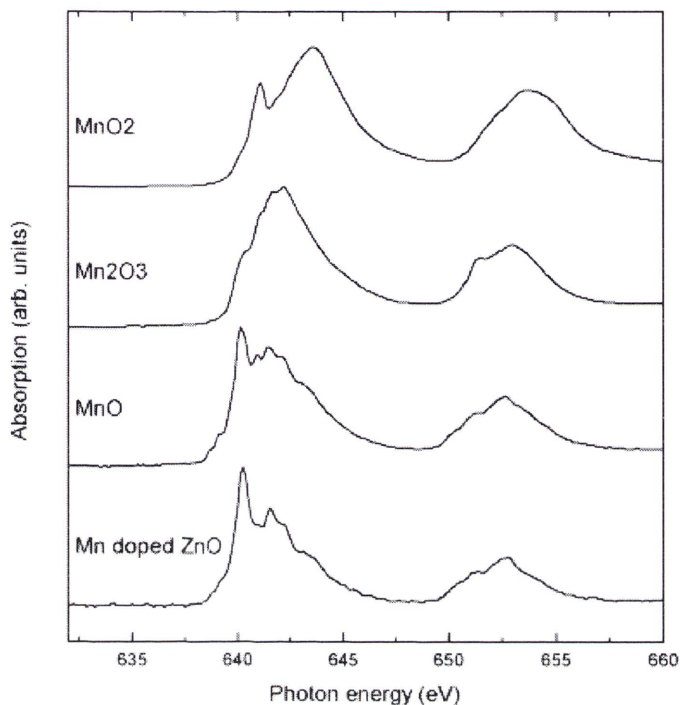


FIGURE 6.4: XANES spectra for Mn doped ZnO powder as compared to reference Mn compounds

6.2.2.2 X-ray diffraction

The powders were examined using x-ray diffractometry (XRD) operating in $\theta - 2\theta$ mode. The XRD scans showed peaks only relating to ZnO, indicating that the Mn doping had resulted in Mn incorporation into the ZnO particles. A typical XRD pattern can be seen in Figure 6.5. The broadening in the peaks, as well as the shift in the peak location, indicates the possible presence of lattice strain to to this incorporation of the Mn ions into the ZnO lattice, or a variation in the particle size.

The lattice parameters for the powders were calculated using Bragg's Law for a hexagonal structure (see Appendix B). Literature reports suggest that the incorporation of Mn into the ZnO lattice will result in an increase in both a and c lattice parameters [208, 209], as the ionic radius of Mn^{2+} (0.66\AA) is larger than that of Zn^{2+} (0.60\AA).

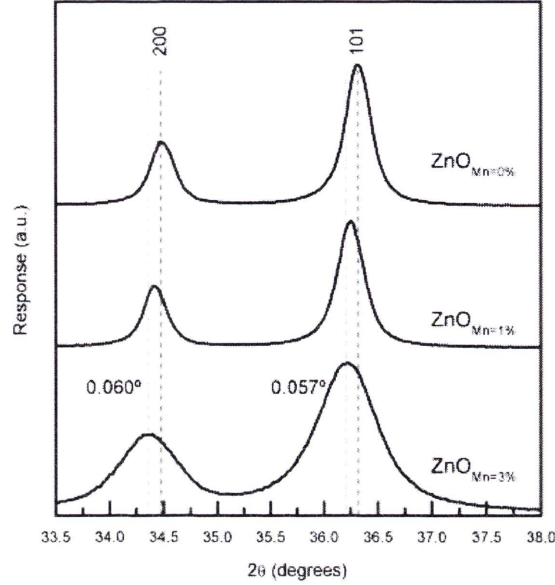


FIGURE 6.5: XRD pattern for Mn doped ZnO of different atomic concentrations of Mn. Peak shifts of 0.060° and 0.057° for the (002) and (101) peaks can be seen.

The lattice parameters (found in Table 6.4 and shown in Figure 6.6) initially show that there is no clear pattern between nominal atomic concentration of Mn and the change in the lattice constants. It should be noted that the samples were prepared in two batches - (0,1,2%) and (0.25, 0.50, 3%). If the Mn is incorporated slightly differently dependant on the synthesis conditions, then it is possible that comparison between batches produced under different conditions is not feasible. If the assumption is made that the incorporation of the Mn into the ZnO occurs differently depending on the preparation method, it is useful to consider the comparison of the change in the c/a ratio as the independent variable for further investigatory measurements. There is also an observable broadening of the diffraction peaks for the ZnO powders as represented in Figure 6.5. This broadening could be the result of a number of factors, in particular instrumental effects [210], crystallite size and strain within the crystal lattice [211, 212]. Using the Williamson-Hall method¹, it is possible to deconvolve the diffraction peaks to establish the contributions from the particle sizes and crystalline strain to the line broadening as a function of 2θ [213]. The instrumental broadening can be established as a function of 2θ through the use

¹Also referred to as Hall-Williamson method

TABLE 6.4: Calculated lattice constants for Mn doped ZnO from experimental data

Mn concentration (nominal at. %)	Lattice constant		
	a (Å)	c (Å)	c/a ratio ($\pm 0.5\%$)
Pure ZnO (Lit.)	3.296	5.207	1.5798
0.00	3.244	5.196	1.6017
0.25	3.252	5.210	1.6021
0.50	3.252	5.210	1.6021
1.00	3.250	5.207	1.6022
2.00	3.251	5.208	1.6019
3.00	3.254	5.214	1.6023

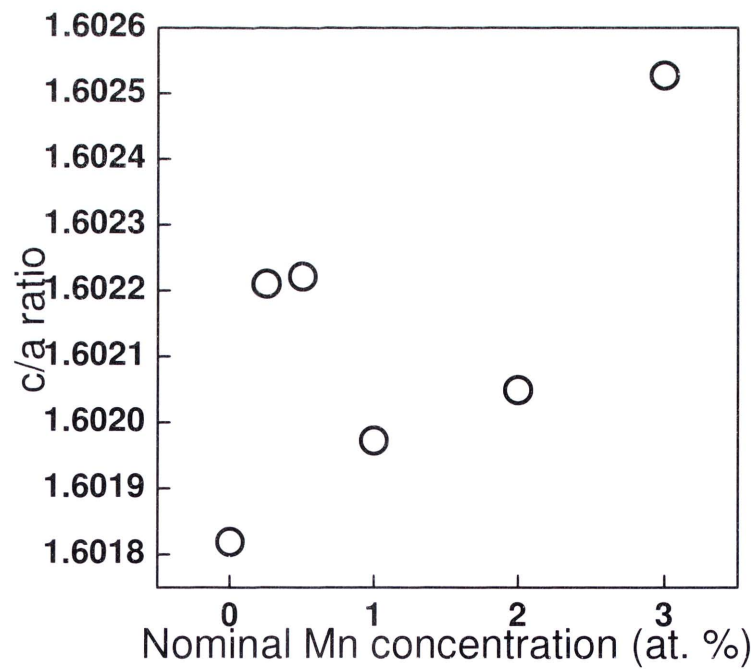


FIGURE 6.6: c/a ratio as a function of Mn nominal concentration in Mn-ZnO powders

of a standard reference material with well-defined peaks. For this work, LaB₆ was used, and a function was fitted to estimate the instrumental broadening for ZnO reflections between that of LaB₆. The Williamson-Hall method plots the full width at half maximum (FWHM) (β) as a function of θ in the following manner:

$$\sqrt{(\beta_{\text{Observed}}^2 - \beta_{\text{Instrumental}}^2)} \times \text{Cos}\theta = 4\eta\text{Sin}\theta + \frac{k\lambda}{D} \quad (6.1)$$

where the β_{Observed} is the FWHM at each indexed reflection the ZnO powder, $\beta_{\text{Instrumental}}$ is calculated from the LaB₆ function, θ is the angle of reflection, η is the strain in the crystallites, and D represents the size of the crystallites. The constant k is typically close to unity, but ranges from 0.8-1.39, while λ is the x-ray wavelength.

Plotting $\beta\text{Cos}\theta$ vs. $4\text{Sin}\theta$ should yield a straight line with a slope η and an intercept related to $\frac{1}{D}$. From the Williamson-Hall plots in Figure 6.7, it is possible to summarise the results obtained and categorise the powders into two groups based on differences between strain and crystallite sizes. These groups reflect the preparation batch (see Table 6.5), suggesting that the two groups were prepared under non-identical conditions. This was confirmed with the synthesis chemists who ad-

TABLE 6.5: Summary of results from Williamson-Hall calculations on Mn doped ZnO powders

Nominal Mn %	4η	$\frac{k\lambda}{D}$	Tentative grouping
0	0.16	0.14	A
0.25	0.35	0.42	B
0.5	0.24	0.43	B
1	0.26	0.12	A
2	0.17	0.16	A
3	0.30	0.41	B

vised that the samples supplied were prepared in two separate sessions following the same recipe, however variations between samples are expected owing to unintentional minor deviations from the ideal recipe. It is likely that these deviations result

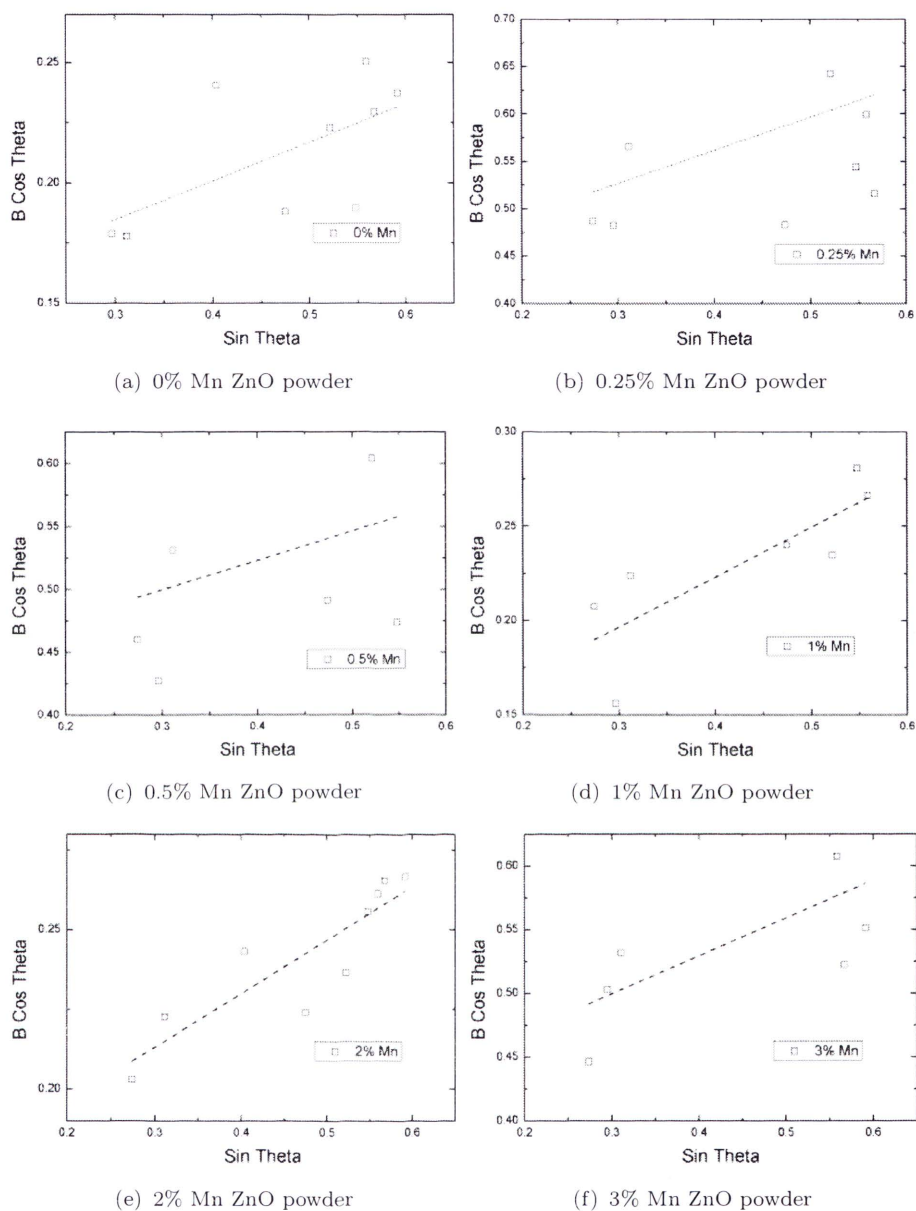


FIGURE 6.7: Williamson-Hall plots for ZnO powders with different atomic concentrations of Mn doping

in different incorporation of the Mn atoms into the ZnO, which would explain the non-linearity observed in Figure 6.6.

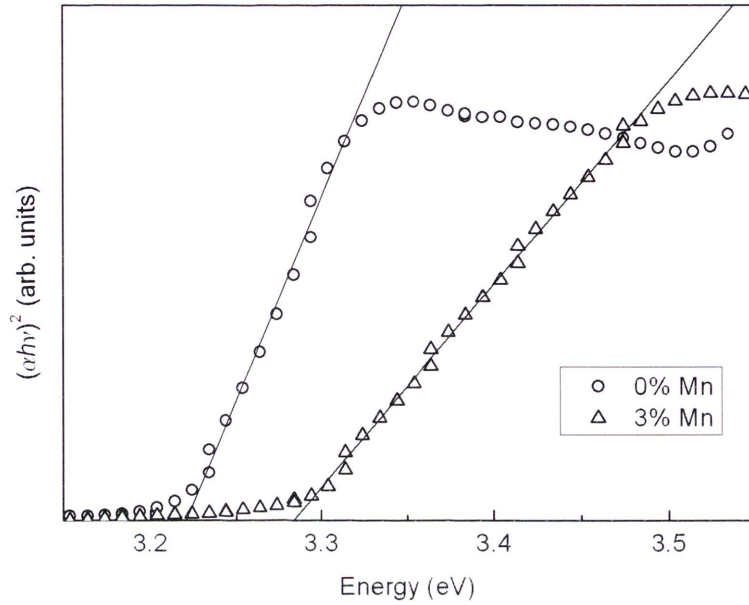


FIGURE 6.8: UV-Vis absorption edge for Mn doped ZnO with different Mn concentrations

6.2.2.3 Ultraviolet-Visible spectroscopy

The properties of the doped ZnO powders were also investigated using ultraviolet-visible spectroscopy (UV-Vis). The powders were prepared as outlined in Section 3.2.6.

The optical band gap of the powders were determined based on Equation 3.10, plotting $(\alpha h\nu)^2$ against $h\nu$ and extrapolating the linear section of the plot, as seen in Figure 6.8. The rapid shift between 3.2 and 3.5 eV relates to the absorption edge and thus the band gap of the ZnO. By extrapolating the linear region of this plot, it is possible to estimate the band gap of the doped powders to be between 3.2 and 3.3 eV, depending on the concentration of the Mn.

A red shift in the band gap is observed as Mn concentration is increased which is attributed to the s-d and p-d interactions resulting in to band gap bowing. This has been theoretically explained using second-order perturbation theory [214] for ternary semiconductors. This red shift is also visible in the CL band gap observations (Figure 6.9). This suggests that the shift observed from the UV-Vis is not a result of

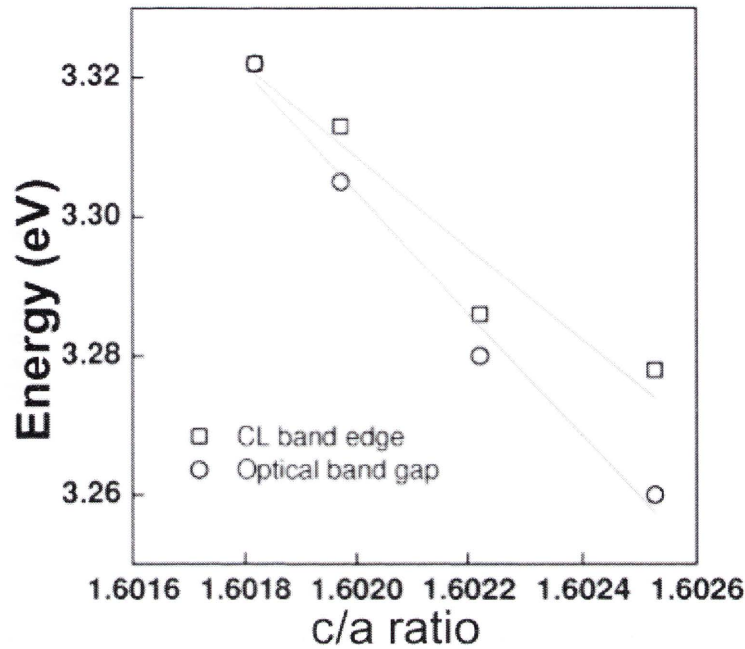


FIGURE 6.9: Band gap obtained for Mn-ZnO powders from UV-Vis and CL as a function of c/a ratio

instrumental offsets in the UV Vis equipment and is due to a shift in the electronic band structure of the ZnO.

6.3 Iron doped ZnO

Hydrothermally grown ZnO crystals (MTI Corporation) were coated with 200 nm thick Fe films by vapour phase deposition and annealed for 70 hours at 880°C in a manner similar to the methodology used in Section 3.1.4.1. An uncoated sample was also annealed under identical conditions to act as a reference.

X-ray photoemission spectroscopy (XPS) of the Fe coated crystals revealed signals from only Zn and O, indicating that any residual iron on the surface was below the detection limit of XPS. If the maximum solubility of the Fe in the ZnO is achieved, it is expected that an iron concentration of approximately 10^{16}cm^{-3} can be obtained.

6.3.1 Analysis of Iron in-diffused ZnO

The samples were examined using CL techniques similar to the Mn samples in Section 6.2.1.1. Further analysis was performed using XANES and photoemission spectroscopy (PES) on the Soft X-ray Spectroscopy beamline at the Australian Synchrotron.

6.3.1.1 Synchrotron light analysis of Fe doped ZnO

The XANES spectrum for an indiffused crystal is shown in Figure 6.10 with comparisons to reference iron oxides and Fe metal. The spectrum concurs with previous reports of chemically synthesised Fe-doped ZnO indicating incorporation of the Fe in the lattice [215]. The separation of the L_2 and L_3 maxima is known to be ~ 13 eV for Fe oxide compounds [216] and this value remains the same for the Fe dopants within the ZnO crystal. As the adsorption edge from the doped crystal is significantly different from that of the Fe metal, it is unlikely that the diffused Fe has formed metallic Fe rich phases within the ZnO and is instead dispersed throughout the matrix. The Fe $L_{2,3}$ spectra from divalent and trivalent Fe display different edge profiles, indicating the sensitivity of the L -edge absorption to the Fe valence state. The L_3 edge in FeO is found at 708.5 eV, while in Fe_2O_3 the L_3 edge has two clear peaks at energies of 708.5 and 710.4 eV. These peaks have been explained and assigned to the t_{2g} and e_g orbitals through a crystal field model [217]. The maxima at the L_3 edge are assigned to electronic transitions based on theoretical calculations [216]: for the Fe^{2+} edge in FeO it is $2p^63d^6 \rightarrow 2p^53d^7$ in a configuration of $(t_{2g} \uparrow)^3(e_g \uparrow)^2(t_{2g} \uparrow)^1$, and for the Fe^{3+} edge in Fe_2O_3 the transition is $2p^63d^5 \rightarrow 2p^53d^6$ in a configuration of $(t_{2g} \uparrow)^3(e_g \uparrow)^2$.

The presence of both Fe^{2+} and Fe^{3+} in the doped ZnO crystal is clear from the double-peak in the L_3 structure. The higher intensity peak on the low-energy side

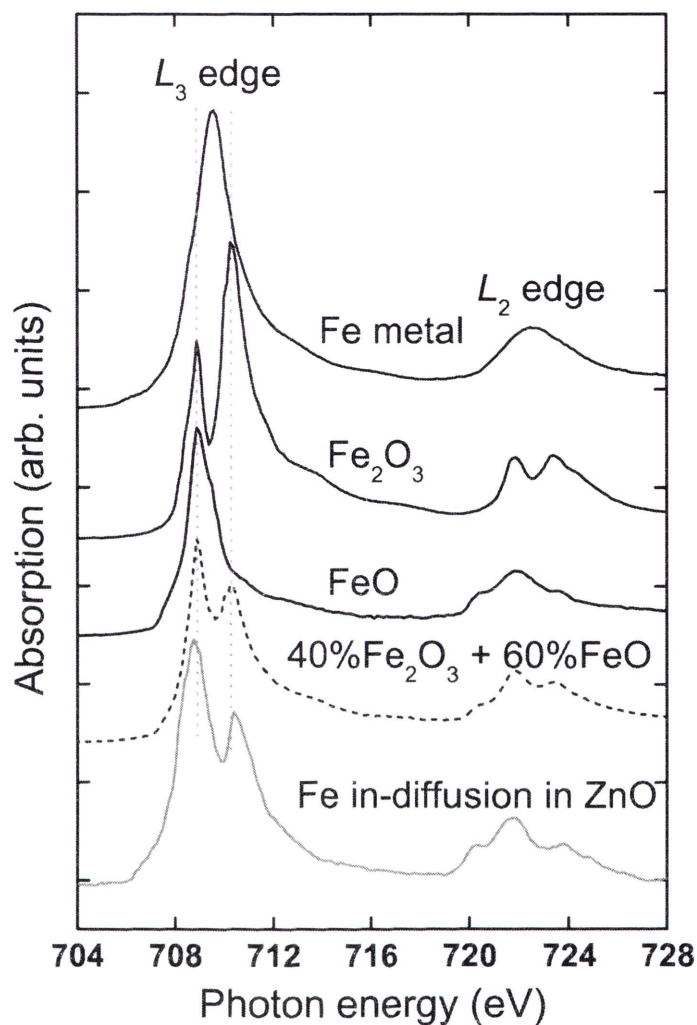


FIGURE 6.10: Fe L-edge XANES spectra of in-diffused ZnO crystal as compared to reference materials and a 2:3 weighted sum of Fe_2O_3 :FeO

indicates that there is an uneven distribution of $\text{Fe}^{2+}/\text{Fe}^{3+}$ within the crystal. Comparing the spectral line shape of with a 40% Fe_2O_3 + 60% FeO L_3 edge weighted sum clearly indicates the mixed Fe valence states², and that they are incorporated as substitutional impurities in ZnO on the Zn sites [131].

The valence-band PES for annealed crystals both with and without Fe diffusion is shown in Figure 6.11. There are three main features in the valence band of the undoped crystal - a sharp peak at 10.5 eV and weaker states centred at 4.2 and

²A similar material - magnetite - is ostensibly Fe_3O_4 but usually formulated as $\text{FeO}\cdot\text{Fe}_2\text{O}_3$ to reflect the mixed valence states present

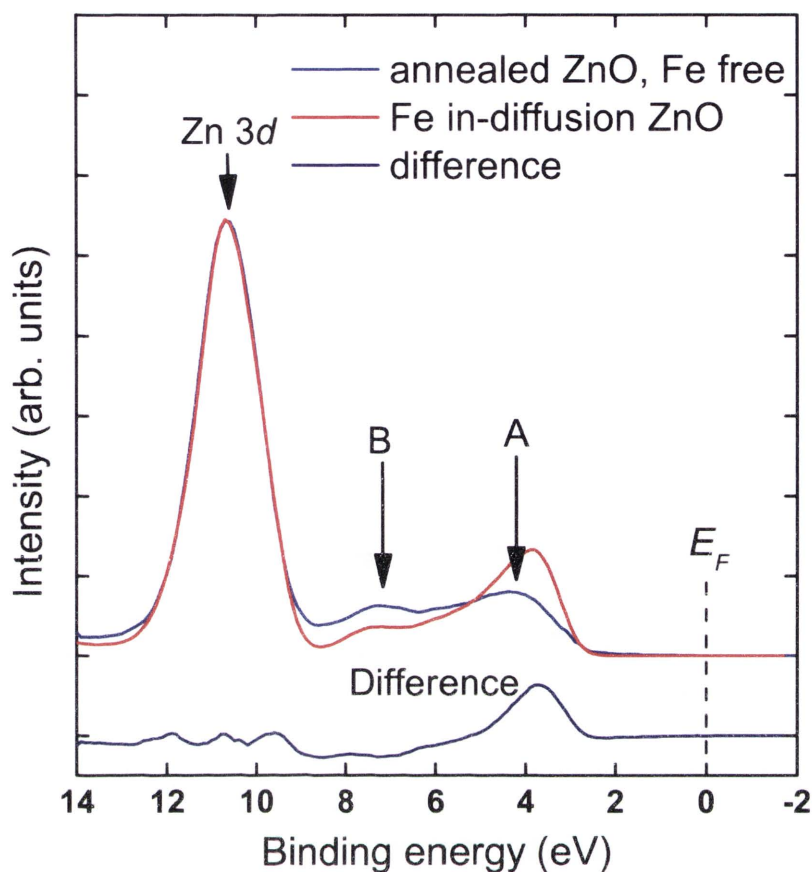


FIGURE 6.11: Valence-band photoemission spectra of annealed α -plane ZnO crystals with and without Fe in-diffusion. Spectra were collected at $h\nu=93$ eV and normalised to the Zn 3d peak.

7.1 eV. The sharp 10.5 eV peak has been assigned to Zn 3d while the weaker peaks have been identified as O 2p and mixed Zn 4s-O 2p states respectively[167, 218]. By comparison, the doped crystal shows significant enhancement of the valence-band region between 2.8-5.0 eV, representing the effect of the introduced Fe 3d states. Furthermore, the decrease in intensity near the O 2p binding energy suggests a possible hybridisation of O 2p-Fe 3d states. The valence band onsets, as determined by the intersection of a linear fit to the leading edge of the valence spectrum and the background, are found to be 2.4 and 2.7 eV below the Fermi level for the undoped and doped crystals respectively. This implies that the introduction of Fe to ZnO will produce an n-doping effect, consistent with the mixed $\text{Fe}^{2+/3+}$ charge states from XANES measurements.

6.3.1.2 Cathodoluminescence analysis of Fe doped ZnO

As discussed in Section 3.2.1.1, an electron beam operating at a low accelerating voltage will give a reduced excitation depth. It was observed that the in-diffused crystals required an accelerating voltage of at least 1.2 kV to produce a CL signal with a suitable signal-to-noise ratio. This corresponds to a depth of approximately 35 nm in ZnO, suggesting that either the incorporation of the Fe has induced a greater number of non-radiative centres in the near surface region, possibly due to band bending effects. As V_O^* is a shallow donor in ZnO, it is expected that an upward bend will shift the Fermi level below the V_O^+/V_O^{2+} energy level, causing most oxygen vacancies near the surface to exist in the non-radiative V_O^{2+} state. The introduction of $Fe^{2+/3+}$ to the near surface region will move the Fermi level towards the conduction band, converting some of the V_O^{2+} centres to the singly ionised state and creating an efficient recombination channel. As a result of this competitive behaviour, the NBE rate of recombination is expected to decrease as the green luminescence (GL) emission increases. The CL spectra of the annealed ZnO crystals with and without Fe diffusion can be seen in Figure 6.12. The ZnO without the Fe incorporation shows only the NBE peak, while the in-diffused sample shows a significant reduction in the NBE emission and subsequent substantial increase in the DL.

To investigate the diffusion penetration, monochromatic CL images were produced across a cleaved Fe in-diffused ZnO crystal. A region of the cleaved crystal was systematically mapped using monochromatic CL imaging at wavelengths corresponding to the NBE and DL peaks. These were then stitched together to form a single image of approximately 9,216 x 5,120 pixels, a section of which is shown in Figure 6.13

These images were then simplified to give colour maps for emission regions as shown in Figure 6.14. These show a ring of green luminescence around the surface of the crystal surrounding a central core of NBE emission. The uniformity of the emission spectra, coupled with the sharp emission boundary between the NBE and DL regions

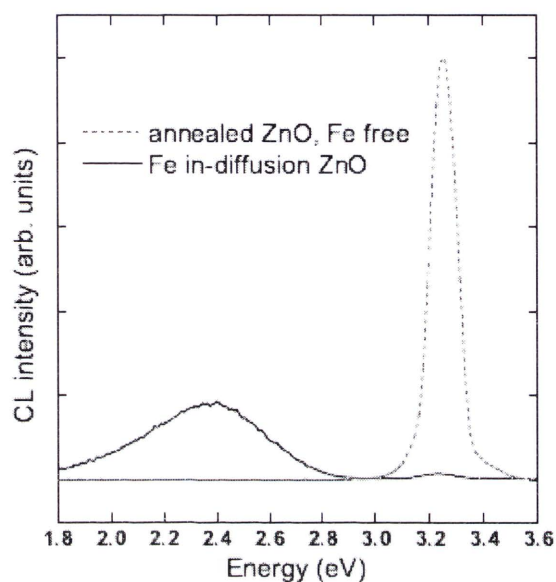


FIGURE 6.12: CL comparison between ZnO with and without Fe in-diffusion

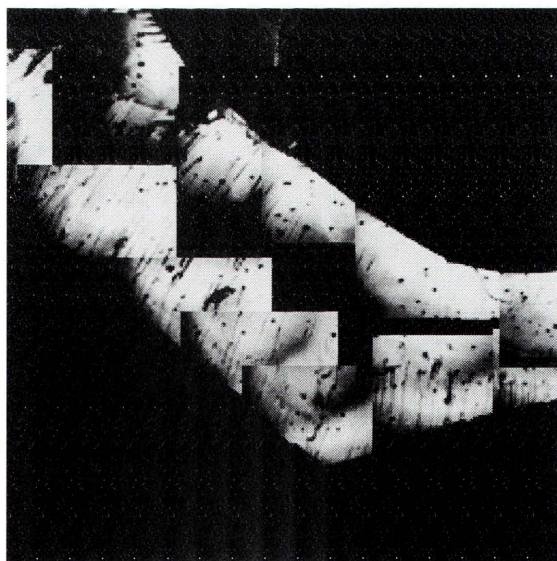


FIGURE 6.13: An example of a section of the stitched monochromatic CL image of cleaved iron in-diffused ZnO crystal. The monochromator was fixed at 2.5 eV, corresponding to the defect emission. The individual frames have been assembled over a secondary electron image of the same region. The clear boundary of the defect emission can be observed, indicating the iron diffusion depth. Mirror induced artifacts can also be seen near the edges of the individual frames.

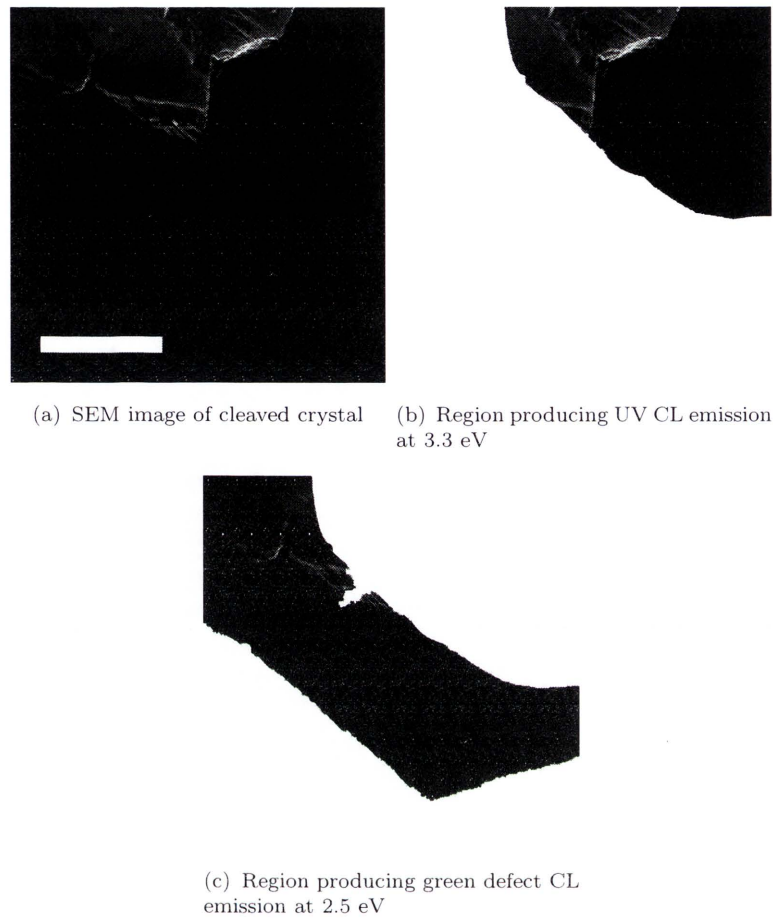


FIGURE 6.14: Cleaved ZnO crystal showing the impact of Fe incorporation on the CL emission. Scale bar represents $500\mu\text{m}$.

suggests that the iron requires a minimum concentration to produce the observed band-bent CL emissions.

6.4 Summaries

A successful method for the doping of transition metals in ZnO crystals has developed using thermal in-diffusion in a glass ampoule under vacuum. Both the Mn and Fe doped crystals showed changes to the optical properties, with the Mn quenching the green emission and the Fe enhancing it significantly.

6.4.1 Mn-doped ZnO

In-diffusion of Mn into ZnO crystals results in a significant reduction in the overall CL intensity, supporting literature observations that Mn acts as a luminescence killer in ZnO. The Mn preferentially reduces the DL green emissions when at low concentration, before quenching the NBE emission when Mn reaches a high enough level. XRD measurements indicate that the Mn atoms substitute for Zn sites in ZnO powders without changing the wurtzite structure, with lattice parameters varying slightly to allow for the incorporation of the larger Mn^{2+} ions. The UV-VIS measurements show the reduction in the band-gap for Mn-ZnO of nominal doping ≤ 3 at. %.

6.4.2 Iron doped

The iron in diffused crystals show that iron incorporates into ZnO in a mixed valence state of $\text{Fe}^{2+/3+}$ and can be found homogeneously distributed throughout the diffused region. This incorporation was found to enhance the green luminescence while changing the charge state of the oxygen vacancies, as determined by PES and XANES measurements. This further supports the conclusion that the primary defect responsible for green luminescence in ZnO is an oxygen vacancy.

Chapter 7

Conclusions and future directions

7.1 Conclusions

The aims of this work were to:

- A comprehensive investigation into the effects of growth conditions on the formation of defects in ZnO and their influence on the optical properties
- Identify the spatial distribution of point defect related emissions in ZnO
- Investigate the influence of postprocessing on optical emission in bulk and nano- ZnO
- Investigate the influence of transition metal dopants on the physical, chemical and electronic properties of both bulk and nano- ZnO

The preceeding chapters have addressed these points, and can be summarised as follows.

The reproducible production of ZnO nanowires was achieved through the development of a carbothermally driven vapour-liquid-solid (VLS) growth process in a three stage furnace on epitaxially matched sapphire substrates. This method is comparatively simple in its design and implementation, as well as being relatively low cost

in comparison to other possible growth methods (such as MOCVD). Furthermore, it shows promise in the development of larger scale areas of growth which would be of considerable interest for future applications and investigations.

The defect luminescence commonly found in ZnO, typically referred to as the green or yellow-green luminescence, was observed to be localised to the surface of ZnO nanostructures. Band bending effects alone do not adequately explain this variation in optical emission between the bulk and surface regions of ZnO, as the growth tips of the nanowires and nanorods can show no defect luminescence. It was found that a significant variation in the oxygen co-ordination, and thus oxygen concentration, can be seen between the sidewalls and tips of the nanostructures. As a result of this work, the green luminescence observed in grown ZnO nanostructures has been assigned to oxygen vacancies, concurring with previous literature reports.

Post processing in various plasma environments has been shown to vary the composition of the defect peak by altering ratio of the constituent defect centres found between 1.7 and 2.6 eV. There is significant variation between bulk and powdered ZnO, indicating a relationship between defect concentration and sample size. Investigations into heavily oxygen deficient ZnO through the use of a ZnO:Zn phosphor have shown that low power plasma processing will not alter the overall emission properties significantly, suggesting the significant presence of defects within the phosphor that cannot be quenched at low plasma intensities. The assignment of V_O to the 2.4-2.5 eV peak is confirmed through these plasma results, along with the confirmation of the 2.15 eV peak as a non-intrinsic point defect owing to its lack of variation between treatment conditions. Penetration depths of the plasma treatments were estimated from depth-resolved cathodoluminescence (DCL) plots showing significant differences in peak intensities with increasing accelerating voltage. Hydrogen was found to penetrate twice as deep into the crystal as the oxygen plasma, to depths of 800 and 400 nm respectively.

The introduction of transition metals can alter not only the band gap of ZnO, following a band bending relationship, but also change the lattice dimensions and suppress defect emissions. This would suggest that the defects responsible for the yellow-green emission are highly sensitive to passivation from the presence of transition metals, or that the metals form a defect-metal complex upon incorporation into the ZnO matrix.

The enhancement of the green luminescence in the iron doped sample, along with a change in the oxygen vacancy charge state, supports the theory that oxygen vacancies are a primary cause of green luminescence in ZnO. The shift in the band edge observed for the Mn doped ZnO, along with a suppression in the defect emission, suggests that Mn is a true luminescence killer, introducing competitive non-radiative recombination channels in ZnO.

7.2 Future directions

There are several areas touched on during the course of this work that could be the focus for further research. The continued development of controlling nanostructure growth and properties, as examined during Chapter 4, is of particular interest, especially in the possibility of the production of single nanostructure optical devices. By controlling the growth conditions, it has been shown in literature that single nanowires consisting of alternating semiconductor layers can be produced through vapour based growth methods. The production of alternating doped and undoped ZnO structures could be of considerable interest, but would require revisiting the growth methodology developed in this study.

Modification of the optical properties through post-growth processing of ZnO is another opportunity. This work focused on bulk crystal or powder samples, however as evidenced in Chapter 4, nanostructures have highly localised optical properties. As

plasma treatment is primarily a surface modification technique, it could be interesting looking at the changes in optical emissions from ZnO nanostructures subjected to different plasma conditions. An issue that would need to be addressed is the propensity of the nanostructures to physically deform under moderate plasma treatment conditions, something not significantly observed in the powders or bulk crystals.

While the incorporation of transition metals into ZnO crystals was presented here, only variations to optical and electronic properties were investigated. A correlation between the optical, electronic and magnetic changes as a result of the doping would certainly be an interesting study, further developing ZnO as an optoelectronically active material. It would also be interesting to perform carrier density studies on the materials studied during this work to see how the different growth and modification conditions change the carrier properties to further investigate surface band bending effects.

From an experimental stand point, the VLS method requires more investigation. While a suitable growth process was developed for this work, the exact mechanisms that govern growth are still yet to be determined. One proposed method for future work is to develop an *in situ* furnace within an electron microscope to observe all stages of growth. There are several issues associated with this proposal, however the process is still considered possible. If the governing mechanisms behind the growth are found, then it becomes possible to produce specific reproducible structures on demand - a key requirement for large scale manufacturing of optoelectronic systems.

7.3 Closing remarks

In summation, ZnO remains a fascinating material with potential applications across a wide range of optoelectronic devices. Of course, the end goal of almost any scientific endeavour today is to eventually produce a commercially viable product. To this end, I believe that a suitable aim for ZnO is for the development of high efficiency lighting.

The key hurdle preventing this is of course the lack of stable p-type ZnO, which is likely due to a lack of understanding of the inherent defects found within ZnO. While significant challenges relating to the production of p-type ZnO remain, continued research should provide us with the necessary understanding to successfully overcome these issues. It is only a matter of time before a breakthrough is found which will propel ZnO to the top of the solid state lighting class, and I hope that the work presented in this thesis has in some way contributed to the greater understanding of the inherent defects that are currently holding it back.

Appendix A

Determination of circularity of a droplet

An adaptation from documentation supplied with ImageJ software [124].

The spread of the droplets obtained through annealing a gold film can contain a wide variety of droplet morphologies when examined through either atomic force microscope (AFM) or scanning electron microscope (SEM). As we are interested only in droplets that form hemispherical or near-hemispherical shapes it becomes necessary to mathematically identify valid droplets. One such method is to assign a circularity value to the droplet.

In this technique, the area and perimeter are compared, giving rise to a value between 0 and 1, where 0 represents an infinite line and 1 a perfect circle.

As the area of a perfect circle is πr^2 and the perimeter is $2\pi r$, the circularity relationship is found to be $4\pi \times \frac{Area}{Perimeter^2}$.

By limiting the 'acceptable' droplets to have a circularity of 0.8 or greater, droplets that form as lines or irregular patterns can be successfully removed from the analysis.

A successfull cleaning can be seen in Figure A.1 below, showing the effective removal of several long droplets.

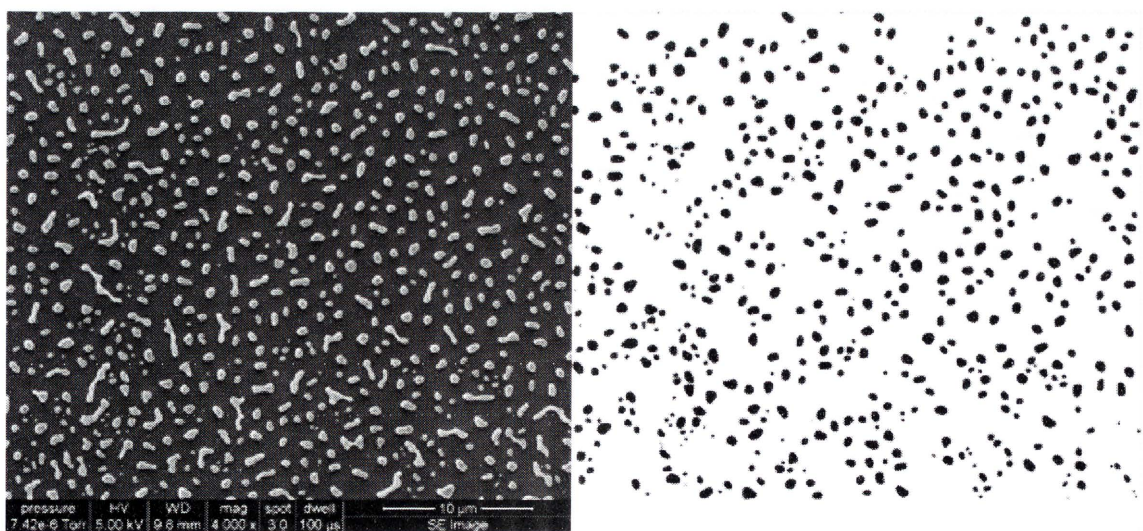


FIGURE A.1: Comparison of as obtained (left) and processed (right) annealed gold film

Appendix B

Derivation of Bragg's Law for a hexagonal unit cell

The crystallographic relationship between the interplanar spacing values obtained from x-ray diffractometry measurements and the lattice constants in a material with a hexagonal unit cell can be obtained through a manipulation of the spacing relationship inherent in a simple cubic system.

A hexagonal system is defined as: $a = b \neq c$, $\alpha = \beta = 90^\circ$ and $\gamma = 120^\circ$

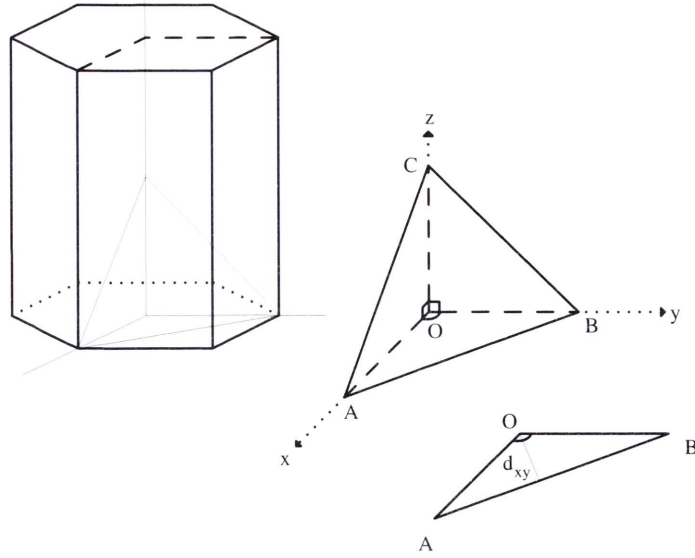


FIGURE B.1: Schematic for manipulation of Bragg's Law for hexagonal unit cell

The interplanar spacing can be calculated for the x-y and z planes independently.
For the x-y plane;

$$\begin{aligned}
 OA &= \frac{a}{h} \\
 OB &= \frac{a}{k} \\
 AOB &= \gamma \\
 &= 120^\circ \\
 AB^2 &= \frac{a^2}{h^2} + \frac{a^2}{k^2} - 2\frac{a}{h}\frac{a}{k}\cos(120^\circ) \\
 &= a^2\left(\frac{1}{h^2} + \frac{1}{k^2} + \frac{1}{hk}\right) \\
 &= a^2\epsilon^2 \\
 \frac{\sin(OAB)}{OB} &= \frac{\sin(AOB)}{AB} \\
 \sin(OAB) &= OB \frac{\sin(120^\circ)}{AB} \\
 &= \frac{\sqrt{3}}{2} \frac{\frac{a}{h}}{AB} \\
 &= \frac{\sqrt{3}}{2h} \frac{1}{\epsilon} \\
 \frac{d_{xy}}{\sin(OAB)} &= \frac{\frac{a}{k}}{\sin(OCA)} \\
 &= \frac{a}{k} \\
 d_{xy} &= \frac{a^2}{h} \frac{\sqrt{3}}{2k\epsilon} \\
 &= \frac{\sqrt{3}a}{2hk} \frac{1}{\sqrt{\frac{1}{h^2} + \frac{1}{k^2} + \frac{1}{hk}}} \\
 d_{xy}^2 &= \frac{3a^2}{4} \frac{1}{h^2k^2\left(\frac{1}{h^2} + \frac{1}{k^2} + \frac{1}{hk}\right)} \\
 \frac{1}{d_{xy}^2} &= \frac{4}{3a^2} (h^2 + k^2 + hk)
 \end{aligned}$$

whereas the z-plane spacing is

$$\frac{1}{d_l^2} = \frac{l^2}{c^2}$$

thus the interplane distance for a given hkl can be calculated from

$$\frac{1}{d^2} = \frac{4}{3a^2}(h^2 + k^2 + hk) + \frac{l^2}{c^2}$$

As Bragg's Law relates θ to d

$$2d\sin\theta = \lambda$$

or

$$d = \frac{\lambda}{2\sin\theta}$$

it is possible to equate the two relationships yielding

$$\begin{aligned} d^2 &= \frac{\lambda^2}{4\sin^2\theta} \\ &= \frac{3a^2}{4(h^2+k^2+hk)} + \frac{c^2}{l^2} \end{aligned}$$

$$\frac{\sin^2\theta}{\lambda^2} = \frac{(h^2+k^2+hk)}{3a^2} + \frac{l^2}{4c^2}$$

Appendix C

Datasheets

TABLE C.1: ZnO single crystal substrate supplied by MTI Corporation

Purity: wt%	> 99.99
Impurity: wt%	Mg: <0.0005 Al: <0.0030 Si: 0.0030 Ti: .0010 Cu: <0.0030 Fe: <0.005 Ca: <0.0005 Ag: <0.0002
Crystal Structure	Hexagonal: a= 3.252 Å, c = 5.313 Å
Growth Method	Hydrothermal
Hardness	4 moh scale
Density	5.7 g/cm3
Melt Point	1975°C
Specific heat	0.125 cal/gm
Thermoelectric Constant	1200 μV/cK @ 300 °C
Thermal conductivity	0.006 cal/cm/K
Thermal expansion	2.90 x 10 ⁻⁶ K
Transmission range	0.4 - 0.6 μ > 50% at 2 mm
Dislocation Density	<0001> plane: < 100 / cm ²

TABLE C.2: Zn doped ZnO phosphor supplied by Phosphor Technology

Chemical composition	Zn:ZnO
Median particle size	3.5 μm
CIE colour coordinates	(0.245, 0.442)
RGB equivalent	(49,204,131)
Emission peak	505 nm

TABLE C.3: 20 nm ZnO supplied by Nanostructured & Amorphous Materials

Purity: wt%	99.5
Impurity: ppm	Cu: ≤ 3 Cd: ≤ 8 Mn: ≤ 5 Pd: ≤ 9 As: ≤ 5
Particle size:	20 nm
Surface area:	50 m^2g^{-1}
Bulk density:	0.3-0.45 gcm^{-3}

TABLE C.4: ZnO powder supplied by Antaria (formerly Advanced Nanotechnology Ltd.)

Purity: wt%	>99
Particle size:	25 nm (XRD)
	30 nm (Electron micrograph)
	31 nm (Photon correlation spectroscopy)
	30 nm (From surface area calculations)

References

- [1] M. Luther Fuller. A method of determining the axial ratio of a crystal from x-ray diffraction data: The axial ratio and lattice constants of Zinc Oxide. *Science*, 23:196–198, 1929.
- [2] C.W. Bunn. The lattice-dimensions of Zinc Oxide. *P. Phys. Soc.*, 47(5): 835–842, September 1935.
- [3] T.J. Gray. Sintering of Zinc Oxide. *J. Am. Chem. Soc.*, 37:534, 1954.
- [4] R.R. Reeber. Lattice parameters of ZnO from 4.2K to 296K. *J. Appl. Phys.*, 41(13):5063–5066, 1970.
- [5] H. Yan *et al.* ZnO nanoribbon microcavity lasers. *Adv. Mater.*, 15(22), 2003.
- [6] M.H. Huang *et al.* Room-temperature ultraviolet nanowire nanolasers. *Science*, 292:1897, 2001.
- [7] D.C. Look and J.W. Hemsky. Residual native shallow donor in ZnO. *Phys. Rev. Lett.*, 82(12):2552–2555, 1999.
- [8] A.Y. Polyakov *et al.* Proton implantation effects on electrical and recombination properties of undoped ZnO. *J. Appl. Phys.*, 94(5):2895–2900, 2003.
- [9] S.O. Kucheyev *et al.* Ion-beam-produced structural defects in ZnO. *Phys. Rev. B*, 67(9):094115, 2003.
- [10] D.C. Look. Recent advances in ZnO materials and devices. *Mater. Sci. Eng. B*, 80:383– 387, 2001.
- [11] F. Hamdani *et al.* Microstructure and optical properties of epitaxial GaN on ZnO (0001) grown by reactive molecular beam epitaxy. *J. Appl. Phys.*, 83(2): 983–990, 1998.

- [12] X. Gu *et al.* GaN epitaxy on thermally treated c-plane bulk ZnO substrates with O and Zn faces. *Appl. Phys. Lett.*, 84(13):2268–2270, 2004.
- [13] M.K. Yadav *et al.* Band-gap variation in Mg- and Cd-doped ZnO nanostructures and molecular clusters. *Phys. Rev. B*, 76(19):195450, 2007.
- [14] U. Özgür *et al.* A comprehensive review of ZnO materials and devices. *J. Appl. Phys.*, 98(4):041301, 2005.
- [15] D.G. Thomas. The exciton spectrum of Zinc Oxide. *J. Phys. Chem. Solids*, 15(1-2):8696, 1960.
- [16] B.D. Yao, Y.F. Chan, and N. Wang. Formation of ZnO nanostructures by a simple way of thermal evaporation. *Appl. Phys. Lett.*, 81(4):757, 2002.
- [17] L.E. Greene *et al.* General route to vertical ZnO nanowire arrays using textured ZnO seeds. *Nano*, 2005.
- [18] C.H. Liu *et al.* High-density, ordered ultraviolet light-emitting ZnO nanowire arrays. *Adv. Mater.*, 15(10):838–841, 2003.
- [19] W.I. Park, Y.H. Jun, S.W. Jung, and G.C. Yi. Excitonic emissions observed in ZnO single crystal nanorods. *Appl. Phys. Lett.*, 82(6):964, 2003.
- [20] J.E. Jaffe and A.C. Hess. Hartree-fock study of phase changes in ZnO at high pressure. *Phys. Rev. B*, 48(11):7903–7909, Sep 1993.
- [21] T.M. Parker, N.G. Condon, R. Lindsay, F.M. Leibsle, and G. Thornton. Imaging the polar and non-polar surfaces of ZnO with STM. *Surf. Sci.*, 415(3): L1046 – L1050, 1998.
- [22] L. Fiermans, E. Arijs, J. Vennik, and W.M.V.D. Vorst. A combined LEED, AES and XPS study of the ZnO 0001 polar surfaces: I. LEED, AES and XPS of contaminated surfaces. *Surf. Sci.*, 39(2):357 – 367, 1973.
- [23] A. B. M. Almamun Ashrafi *et al.* Growth and characterization of hypothetical Zinc-blende ZnO films on gaas(001) substrates with zns buffer layers. *Appl. Phys. Lett.*, 76(5):550–552, 2000.
- [24] S. Saib and N. Bouarissa. Structural parameters and transition pressures of ZnO: ab-initio calculations. *Phys. Status Solidi B*, 244:1063–1069, March 2007.

- [25] S. Desgreniers. High-density phases of ZnO: Structural and compressive parameters. *Phys. Rev. B*, 58(21):14102–14105, Dec 1998.
- [26] J.E. Jaffe, J.A. Snyder, Z. Lin, and A.C. Hess. LDA and GGA calculations for high-pressure phase transitions in ZnO and MgO. *Phys. Rev. B*, 62(3):1660–1665, Jul 2000.
- [27] D.I. Florescu *et al.* High spatial resolution thermal conductivity of bulk ZnO (0001). *J. Appl. Phys.*, 91(2):890–892, 2002.
- [28] U. Rössler. Energy bands of hexagonal II-VI semiconductors. *Phys. Rev.*, 184(3):733–738, 1969.
- [29] D. Langer, R. Euwema, K. Era, and T. Koda. Spin exchange in excitons, the quasicubic model and deformation potentials in II-VI compounds. *Phys. Rev. B*, 2(10):4005–4022, 1970.
- [30] R. Powell, W. Spicer, and J. McMenamin. Location of the Zn 3d States in ZnO. *Phys. Rev. Lett.*, 27(2):97100, 1971.
- [31] R. Powell, W. Spicer, and J. McMenamin. Photoemission studies of wurtzite Zinc Oxide. *Phys. Rev. B*, 6(8):3056–3065, 1972.
- [32] L. Ley, R.A. Pollak, F.R. McFeely, S.P. Kowalczyk, and D.A. Shirley. Total valence-band densities of states of III-V and II-VI compounds from x-ray photoemission spectroscopy. *Phys. Rev. B*, 9(2):600–621, Jan 1974.
- [33] C.J. Vesely, R.L. Hengehold, and D.W. Langer. UV photoemission measurements of the upper *d* levels in the IIB-VIA compounds. *Phys. Rev. B*, 5(6):2296–2301, Mar 1972.
- [34] R. Girard. Electronic structure of ZnO(0001) studied by angle-resolved photoelectron spectroscopy. *Surf. Sci.*, 373(2-3):409–417, March 1997.
- [35] P. Schröer, P. Krüger, and J. Pollmann. First-principles calculation of the electronic structure of the wurtzite semiconductors ZnO and ZnS. *Phys. Rev. B*, 47(12):6971–6980, Mar 1993.
- [36] H.J. Ko *et al.* Photoluminescence properties of ZnO epilayers grown on CaF₂(111) by plasma assisted molecular beam epitaxy. *Appl. Phys. Lett.*, 76(14):1905–1907, 2000.

- [37] A.R. Denton and N.W. Ashcroft. Vegard's Law. *Phys. Rev. A*, 43(6):3161–3164, 1991.
- [38] N. Izyumskaya, V. Avrutin, U. Özgür, Y.I. Alivov, and H. Morkoç. Preparation and properties of ZnO and devices. *Phys. Status Solidi B*, 244(5):1439–1450, May 2007.
- [39] V. Celli, M. Kabler, T. Ninomiya, and R. Thomson. Theory of dislocation mobility in semiconductors. *Phys. Rev.*, 131(1):58–72, Jul 1963.
- [40] T.R. Paudel and W.R.L. Lambrecht. First-principles calculation of the oxygen vacancy in ZnO: A self-consistent gap-corrected approach. *Phys. Rev. B*, 77(20):205202, May 2008.
- [41] P. Erhart, A. Klein, and K. Albe. First-principles study of the structure and stability of oxygen defects in zinc oxide. *Phys. Rev. B*, 72(8):085213, Aug 2005.
- [42] F. Oba, S.R. Nishitani, S. Isotani, H. Adachi, and I. Tanaka. Energetics of native defects in ZnO. *J. Appl. Phys.*, 90(2):824–828, 2001.
- [43] P. Erhart, K. Albe, and A. Klein. First-principles study of intrinsic point defects in ZnO: Role of band structure, volume relaxation, and finite-size effects. *Phys. Rev. B*, 73(20):1–9, 2006.
- [44] F. Oba, A. Togo, I. Tanaka, J. Paier, and G. Kresse. Defect energetics in ZnO: A hybrid hartree-fock density functional study. *Phys. Rev. B*, 77(24):245202, Jun 2008.
- [45] S. Lany and A. Zunger. Dopability, intrinsic conductivity, and nonstoichiometry of transparent conducting oxides. *Phys. Rev. Lett.*, 98(4):045501, Jan 2007.
- [46] A. Janotti and C.G. Van de Walle. Hydrogen multicentre bonds. *Nat. Mater.*, 6(1):44–47, 2007.
- [47] J. Carrasco, N. Lopez, and F. Illas. First principles analysis of the stability and diffusion of oxygen vacancies in metal oxides. *Phys. Rev. Lett.*, 93(22), Nove 26 2004.
- [48] A. Janotti and C.G. Van de Walle. Native point defects in ZnO. *Phys. Rev. B*, 76(16):1–22, 2007.

- [49] L. Kappers, O. Gilliam, S. Evans, L. Halliburton, and N. Giles. EPR and optical study of oxygen and zinc vacancies in electron-irradiated ZnO. *Nucl. Instrum. Meth. B*, 266(12-13):2953 – 2957, 2008.
- [50] L.S. Vlasenko and G.D. Watkins. Optical detection of electron paramagnetic resonance in room-temperature electron-irradiated ZnO. *Phys. Rev. B*, 71(12):125210, Mar 2005.
- [51] A.F. Kohan, G. Ceder, and D. Morgan. First-principles study of native point defects in ZnO. *Phys. Rev. B*, 61(22):19–27, 2000.
- [52] M.G. Wardle, J.P. Goss, and P.R. Briddon. Theory of fe, co, ni, cu, and their complexes with hydrogen in ZnO. *Phys. Rev. B*, 72(15):155108, Oct 2005.
- [53] S.M. Evans, N.C. Giles, L.E. Halliburton, and L.A. Kappers. Further characterization of oxygen vacancies and zinc vacancies in electron-irradiated ZnO. *J. Appl. Phys.*, 103(4):043710, 2008.
- [54] T. Sekiguchi, N. Ohashi, and Y. Terada. Effect of hydrogenation on ZnO luminescence. *Jpn. J. Appl. Phys.*, 36(Part 2, No. 3A):L289–L291, 1997.
- [55] K. Vanheusden *et al.* Mechanisms behind green photoluminescence in ZnO phosphor powders. *J. Appl. Phys.*, 79(10):7983, 1996.
- [56] A. Janotti and G.D. Watkins. Oxygen vacancies in ZnO. *Appl. Phys. Lett.*, 87(12):122102, 2005.
- [57] D.M. Hofmann *et al.* Properties of the oxygen vacancy in ZnO. *Appl. Phys. A*, 88(1):147–151, July 2007.
- [58] Y. Heo, D. Norton, and S. Pearton. Origin of green luminescence in ZnO thin film grown by molecular-beam epitaxy. *J. Appl. Phys.*, 98(7):073502, OCT 1 2005.
- [59] F. Tuomisto, K. Saarinen, D.C. Look, and G.C. Farlow. Introduction and recovery of point defects in electron-irradiated ZnO. *Phys. Rev. B*, 72(8):085206, Aug 2005.
- [60] D.C. Look *et al.* Evidence for native-defect donors in n-type ZnO. *Phys. Rev. Lett.*, 225502(November):1–4, 2005.

- [61] B.K. Meyer *et al.* Bound exciton and donor-acceptor pair recombinations in ZnO. *Phys. Status Solidi B*, 241:231–260, February 2004.
- [62] R. Dingle. Luminescent transitions associated with divalent copper impurities and the green emission from semiconducting Zinc Oxide. *Phys. Rev. Lett.*, 23(11):579–581, 1969.
- [63] S.B. Zhang, S.H. Wei, and A. Zunger. Intrinsic n-type versus p-type doping asymmetry and the defect physics of ZnO. *Phys. Rev. B*, 63:075205–1–075205–5, 2001.
- [64] D.C. Herbert. An extension of Haynes’ rule for bound excitons. *J. Phys. C Solid State*, 17(34):L901, 1984.
- [65] D. Reynolds, C. Litton, and T. Collins. Zeeman Effects in the Edge Emission and Absorption of ZnO. *Phys. Rev.*, 140(5A):A1726–A1734, 1965.
- [66] D.C. Reynolds *et al.* Neutral-donorbound-exciton complexes in ZnO crystals. *Phys. Rev. B*, 57(19):151–155, 1998.
- [67] A. Teke *et al.* Excitonic fine structure and recombination dynamics in single-crystalline ZnO. *Phys. Rev. B*, 70(19):1–10, 2004.
- [68] C. Boemare, T. Monteiro, M.J. Soares, J.G. Guilherme, and E. Alves. Photoluminescence studies in ZnO samples. *Physica B*, 310:985–988, 2001.
- [69] P. Schröer, P. Krüger, and J. Pollmann. Self-consistent electronic-structure calculations of the (10 $\bar{1}$ 0) surfaces of the wurtzite compounds ZnO and CdS. *Phys. Rev. B*, 49(24):17092–17101, Jun 1994.
- [70] K. Ozawa, K. Sawada, Y. Shirotori, K. Edamoto, and M. Nakatake. Angle-resolved photoelectron spectroscopy study of the anion-derived dangling-bond band on ZnO(10 $\bar{1}$ 0). *Phys. Rev. B*, 68(12):125417, Sep 2003.
- [71] A. Soudi, P. Dhakal, and Y. Gu. Diameter dependence of the minority carrier diffusion length in individual ZnO nanowires. *Appl. Phys. Lett.*, 96(25):253115, 2010.
- [72] J. Wilson and J. Hawkes. *Optoelectronics: an introduction*. Prentice Hall, Great Britain, Third edition, 1998.

- [73] C.G. Van de Walle. Defect analysis and engineering in ZnO. *Physica B*, 308-310:899 – 903, 2001.
- [74] J. Neugebauer and C.G. Van de Walle. Gallium vacancies and the yellow luminescence in GaN. *Appl. Phys. Lett.*, 69(4):503–505, 1996.
- [75] A. Kobayashi, O. Sankey, and J. Dow. Deep energy levels of defects in the wurtzite semiconductors AlN, CdS, CdSe, ZnS, and ZnO. *Phys. Rev. B*, 28(2):946–956, 1983.
- [76] Y. Yan, S. Zhang, and S. Pantelides. Control of doping by impurity chemical potentials: Predictions for p-type ZnO. *Phys. Rev. Lett.*, 86(25):5723–5726, 2001.
- [77] F.H. Leiter, H.R. Alves, A. Hofstaetter, D.M. Hofmann, and B.K. Meyer. The oxygen vacancy as the origin of a green emission in undoped ZnO. *Phys. Status Solidi B*, 226(1):R4–R5, 2001.
- [78] F. Leiter. Oxygen vacancies in ZnO. *Physica B*, 340-342:201–204, 2003.
- [79] X. Yang *et al.* Effect of post-thermal annealing on properties of ZnO thin film grown on c-Al₂O₃ by metal-organic chemical vapor deposition. *J. Cryst. Growth.*, 252(1-3):275 – 278, 2003.
- [80] B. Guo, Z.R. Qiu, and K.S. Wong. Intensity dependence and transient dynamics of donor–acceptor pair recombination in ZnO thin films grown on (001) silicon. *Appl. Phys. Lett.*, 82(14):2290–2292, 2003.
- [81] H. Egelhaaf. Luminescence and nonradiative deactivation of excited states involving oxygen defect centers in polycrystalline ZnO. *J. Cryst. Growth.*, 161(1-4):190–194, 1996.
- [82] N. Korsunska. The influence of defect drift in external electric field on green luminescence of ZnO single crystals. *J. Lumin.*, 102:733–736, May 2003.
- [83] B. Lin, Z. Fu, and Y. Jia. Green luminescent center in undoped Zinc Oxide films deposited on silicon substrates. *Appl. Phys. Lett.*, 79(7):943–945, 2001.
- [84] S.A. Studenikin, N. Golego, and M. Cocivera. Fabrication of green and orange photoluminescent, undoped ZnO films using spray pyrolysis. *J. Appl. Phys.*, 84(4):2287–2294, 1998.

- [85] M.A. Reshchikov and R.Y. Korokov. Analysis of the temperature and excitation intensity dependencies of photoluminescence in undoped GaN films. *Phys. Rev. B*, 64(11):115205, Aug 2001.
- [86] W.M. Kwok, A.B. Djurisić, Y.H. Leung, W.K. Chan, and D.L. Phillips. Time-resolved photoluminescence study of the stimulated emission in ZnO nanoneedles. *Appl. Phys. Lett.*, 87(9):093108–093108–3, August 2005.
- [87] L.E. Greene *et al.* Low-temperature wafer-scale production of ZnO nanowire arrays. *Angew. Chem. Int. Edit.*, 42(26):3031–3034, 2003.
- [88] N. Ohashi *et al.* Yellowish-white luminescence in codoped Zinc Oxide. *Appl. Phys. Lett.*, 86(9):091902, 2005.
- [89] Y.J. Zeng *et al.* Identification of acceptor states in Li-doped p-type ZnO thin films. *Appl. Phys. Lett.*, 89(4):042106, 2006.
- [90] D. Behera and B. Acharya. Study of the microstructural and photoluminescence properties of Li-doped ZnO thin films prepared by spray pyrolysis. *Ionics*, 16:543–548, 2010.
- [91] R.M. de la Cruz, R. Pareja, R. González, L.A. Boatner, and Y. Chen. Effect of thermochemical reduction on the electrical, optical-absorption, and positron-annihilation characteristics of ZnO crystals. *Phys. Rev. B*, 45(12):6581–6586, Mar 1992.
- [92] W. Ehret and A. Greenstone. Red Zinc Oxide. *J. Am. Chem. Soc.*, 65:872–877, 1943.
- [93] L.E. Halliburton *et al.* Production of native donors in ZnO by annealing at high temperature in Zn vapor. *Appl. Phys. Lett.*, 87(17):172108, 2005.
- [94] S. Jokela and M. McCluskey. Hydrogen complexes in ZnO grown by chemical vapor transport. *Physica B*, 401-402:395 – 398, 2007. Proceedings of the 24th International Conference on Defects in Semiconductors.
- [95] F.A. Selim, M.H. Weber, D. Solodovnikov, and K.G. Lynn. Nature of native defects in ZnO. *Phys. Rev. Lett.*, 99(8):085502, Aug 2007.

- [96] Z.Q. Chen, M. Maekawa, A. Kawasuso, S. Sakai, and H. Naramoto. Annealing process of ion-implantation-induced defects in ZnO: Chemical effect of the ion species. *J. Appl. Phys.*, 99(9):093507, 2006.
- [97] M. Weber, N. Parmar, K. Jones, and K. Lynn. Oxygen deficiency and hydrogen turn ZnO red. *J. Elec. Mater.*, 39:573–576, 2010.
- [98] T. Yamamoto, T. Shiosaki, and A. Kawabata. Characterization of ZnO piezoelectric films prepared by rf planar-magnetron sputtering. *J. Appl. Phys.*, 51(6):3113–3120, 1980.
- [99] T. Mitsuyu, S. Ono, and K. Wasa. Structures and saw properties of rf-sputtered single-crystal films of ZnO on sapphire. *J. Appl. Phys.*, 51(5):2464–2470, 1980.
- [100] A. Hachigo, H. Nakahata, K. Higaki, S. Fujii, and S. ichi Shikata. Heteroepitaxial growth of ZnO films on diamond (111) plane by magnetron sputtering. *Appl. Phys. Lett.*, 65(20):2556–2558, 1994.
- [101] J.G.E. Gardeniers, Z.M. Rittersma, and G.J. Burger. Preferred orientation and piezoelectricity in sputtered ZnO films. *J. Appl. Phys.*, 83(12):7844–7854, 1998.
- [102] M. Kasuga and M. Mochizuki. Orientation relationships of Zinc Oxide on sapphire in heteroepitaxial chemical vapor deposition. *J. Cryst. Growth.*, 54: 185–194, August 1981.
- [103] S.K. Tiku, C.K. Lau, and K.M. Lakin. Chemical vapor deposition of ZnO epitaxial films on sapphire. *Appl. Phys. Lett.*, 36(4):318–320, 1980.
- [104] G. Galli and J.E. Coker. Epitaxial ZnO on Sapphire. *Appl. Phys. Lett.*, 16: 439–441, June 1970.
- [105] S. Wang. Method and apparatus for Zinc Oxide single crystal boule growth, May 2006. US Patent: 7279040.
- [106] H. Okamoto. Au-Zn (Gold-Zinc). *J. Phase. Equilib. Diff.*, 27(4):427–427, 2006.
- [107] Y. Zhang *et al.* A simple method to synthesize nanowires. *Chem. Mater.*, 14: 3564, 2002.

- [108] Y.C. Kong, D.P. Yu, B. Zhang, W. Fang, and S.Q. Feng. Ultraviolet-emitting ZnO nanowires synthesized by a physical vapor deposition approach. *Appl. Phys. Lett.*, 78(4):407–409, 2001.
- [109] R.S. Wagner and W.C. Ellis. Vapor-liquid-solid mechanism of single crystal growth. *Appl. Phys. Lett.*, 4(5):89–90, 1964.
- [110] K.A. Dick. A review of nanowire growth promoted by alloys and non-alloying elements with emphasis on Au-assisted III-V nanowires. *Prog. Cryst. Growth Ch.*, 54:138–173, 2008.
- [111] L. Schmidt-Mende and J.L. MacManus-Driscoll. ZnO - nanostructures, defects, and devices. *Mater. Today*, 10(5):40 – 48, 2007.
- [112] E.C. Greyson, Y. Babayan, and T.W. Odom. Directed growth of ordered arrays of small-diameter ZnO nanowires. *Adv. Mater.*, 16:1348–1352, 2004.
- [113] A.I. Persson *et al.* Solid-phase diffusion mechanism for GaAs nanowire growth. *Nat. Mater.*, 3:677–681, October 2004.
- [114] T.I. Kamins, R.S. Williams, D.P. Basile, T. Hesjedal, and J.S. Harris. Ti-catalyzed Si nanowires by chemical vapor deposition: Microscopy and growth mechanisms. *J. Appl. Phys.*, 89(2):1008–1016, 2001.
- [115] Z.R. Dai, Z.W. Pan, and Z.L. Wang. Novel nanostructures of functional oxides. *Adv. Func. Mat.*, 13, 2003.
- [116] H. Yasuda and H. Mori. Spontaneous alloying of zinc atoms into gold clusters and formation of compound clusters. *Phys. Rev. Lett.*, 69(26):3747–3750, Dec 1992.
- [117] M. Huang *et al.* Catalytic growth of Zinc Oxide nanowires by vapor transport. *Adv. Mater.*, 13(2):113–116, January 2001.
- [118] X. Wang, C.J. Summers, and Z.L. Wang. Large-scale hexagonal-patterned growth of aligned ZnO nanorods for nano-optoelectronics and nanosensor arrays. *Nano Lett.*, 4(3):423–426, 2004. doi: 10.1021/nl035102c.
- [119] H.T. Ng *et al.* Optical properties of single-crystalline ZnO nanowires on m-sapphire. *Appl. Phys. Lett.*, 82(13):2023–2025, 2003.

- [120] J. Park, H.H. Cho, K. Siebein, and R.K. Singh. Two-step evaporation process for formation of aligned Zinc Oxide nanowires. *J. Cryst. Growth.*, 258:342–348, November 2003.
- [121] X. Sun. Shape controllable synthesis of ZnO nanorod arrays via vapor phase growth. *Solid State Commun.*, 129(12):803–807, March 2004.
- [122] P. Buffat and J.P. Borel. Size effect on the melting temperature of gold particles. *Phys. Rev. A*, 13(6):2287–2298, 1976.
- [123] C. Ton-That, A.G. Shard, and R.H. Bradley. Thickness of spin-cast polymer thin films determined by angle-resolved XPS and AFM tip-scratch methods. *Langmuir*, 16(5):2281–2284, 2000.
- [124] W. Rasband. ImageJ. <http://rsb.info.nih.gov/ij/>, 1997-2009.
- [125] M. Abramoff, P. Magelhaes, and S. Ram. Image Processing with ImageJ. *Biophotonics International*, 11:36–42, 2004.
- [126] B.J. Chen, X.W. Sun, and C.X. Xu. Fabrication of Zinc Oxide nanostructures on gold-coated silicon substrate by thermal chemical reactions vapor transport deposition in air. *Ceram. Int.*, 30(7):1725 – 1729, 2004. 3rd Asian Meeting on Electroceramics.
- [127] P. Yang *et al.* Controlled growth of ZnO nanowires and their optical properties. *Adv. Func. Mat.*, 12(5):323–331, 2002.
- [128] H. Bracht. Diffusion and defect reactions in isotopically controlled semiconductors. *Adv. Mater.*, 8, 2008.
- [129] C. Jäger and W. Jäger. Defect formation and dopant diffusion in III V semiconductors: Zinc diffusion in GaP. *J. Phys.: Condens. Matter*, 14:12865–12870, 2002.
- [130] Y. Alivov, M. Chukichev, and V. Nikitenko. Green luminescence band of zinc oxide films copper-doped by thermal diffusion. *Semiconductors*, 38:31–35, 2004.
- [131] C. Ton-That *et al.* Diffusion synthesis and electronic properties of Fe-doped ZnO. *Mater. Lett.*, 64(3):386 – 388, 2010.

- [132] T.L. Phan, R. Vincent, D. Cherns, N.X. Nghia, and V.V. Ursaki. Raman scattering in Me-doped ZnO nanorods (Me = Mn, Co, Cu and Ni) prepared by thermal diffusion. *Nanotechnology*, 19(47):475702, 2008.
- [133] F.W. Kleinlein and R. Helbig. Diffusionskonstante und charakteristische Absorption vor der Bandkante von Mn in ZnO-Kristallen. *Z. Phys.*, 266(3): 201–207, June 1974.
- [134] F.A. Ponce, D.P. Bour, W. Götz, and P.J. Wright. Spatial distribution of the luminescence in GaN thin films. *Appl. Phys. Lett.*, 68(1):57–59, 1996.
- [135] H.J. Fan *et al.* Local luminescence of ZnO nanowire-covered surface: A cathodoluminescence microscopy study. *Appl. Phys. Lett.*, 86(2):023113, 2005.
- [136] K. Kanaya and S. Okayama. Penetration and energy-loss theory of electrons in solid targets. *J. Phys. D. Appl. Phys.*, 5(1):43–58, January 1972.
- [137] M.R. Phillips, H. Telg, S.O. Kucheyev, O. Gelhausen, and M. Toth. Cathodoluminescence efficiency dependence on excitation density in n-type gallium nitride. *Microsc. Microanal.*, 9:144–151, 2003.
- [138] S.O. Kucheyev, M. Toth, M.R. Phillips, J.S. Williams, and C. Jagadish. Effects of excitation density on cathodoluminescence from GaN. *Appl. Phys. Lett.*, 79 (14):2154, 2001.
- [139] J. Mullhauser, O. Brandt, H. Yang, and K. Ploog. Exciton luminescence of single-crystal GaN. *First International Symposium on Gallium Nitride and Related Materials*, pages 607–612, 1996.
- [140] R. Singh, R.J. Molnar, M.S. Unlu, and T.D. Moustakas. Intensity dependence of photoluminescence in GaN thin films. *Appl. Phys. Lett.*, 64(3):336–338, January 1994.
- [141] D. Drouin *et al.* CASINO v2.42 - a fast and easy-to-use modeling tool for scanning electron microscopy and microanalysis users. *Scanning*, 29:92–101, 2007.
- [142] M. Phillips. Unpublished work. 2006.

- [143] U. Rossler. *Landolt-Bornstein Numerical Data and Functional Relationships in Science and Technology: Semiconductors*, volume III/41. Springer-Verlag, Berlin, 1999.
- [144] H. Zhou *et al.* Behind the weak excitonic emission of ZnO quantum dots: ZnO/Zn(OH)₂ core-shell structure. *Appl. Phys. Lett.*, 80(2):210–212, 2002.
- [145] C. Ton-That, M.R. Phillips, and T.P. Nguyen. Blue shift in the luminescence spectra of MEH-PPV films containing ZnO nanoparticles. *J. Lumin.*, 128(12): 2031 – 2034, 2008.
- [146] M.W. Ahn *et al.* Gas sensing properties of defect-controlled ZnO-nanowire gas sensor. *Appl. Phys. Lett.*, 93(26), 2008.
- [147] R.A. Laudise and A.A. Ballman. Hydrothermal synthesis of zinc oxide and zinc sulfide. *J. Phys. Chem.*, 64(5):688–691, 1960.
- [148] C. Ye, X. Fang, Y. Hao, X. Teng, and L. Zhang. Zinc Oxide nanostructures: morphology derivation and evolution. *J. Phys. Chem. B*, 109(42):19758–65, October 2005.
- [149] R.T.R. Kumar *et al.* Growth of ZnO nanostructures on Au-coated Si: Influence of growth temperature on growth mechanism and morphology. *J. Appl. Phys.*, 104(8):84309, 2008.
- [150] M. Jung *et al.* Investigation of the luminescence properties of ZnO tetrapods and clusters grown on Si substrates. *Physica E*, 31(2):187190, 2006.
- [151] J.W. Shin *et al.* Growth mechanisms of thin-film columnar structures in Zinc Oxide on p-type silicon substrates. *Appl. Phys. Lett.*, 88(9):091911, 2006.
- [152] S. Pitayapiboonpong, S. Kanjanachuchai, D. Phokharatkul, A. Tuantranont, and A. Wisitsoraat. Effect of substrate position on the formation of ZnO nanostructures synthesized by thermal evaporation of ZnO-CNTs mixture. In *Electrical Engineering/Electronics Computer Telecommunications and Information Technology*, pages 768 –771, May 2010.
- [153] L. Liao *et al.* Self-assembly of aligned ZnO nanoscrews: Growth, configuration, and field emission. *Appl. Phys. Lett.*, 86(8):083106, 2005.

- [154] H.W. Kim *et al.* Effect of growth temperature on the ZnO nanowires prepared by thermal heating of Zn powders. *Curr. Appl. Phys.*, 10(1):52 – 56, 2010.
- [155] J. Song, X. Wang, E. Riedo, and Z.L. Wang. Systematic study on experimental conditions for large-scale growth of aligned ZnO nanowires on nitrides. *J. Phys. Chem. B*, 109(20):9869–9872, 2005.
- [156] H. Morkoç and Ümit Özgür. *Zinc Oxide: Fundamentals, Materials and Device Technology*. WILEY-VCH Verlag GmbH and Co., KGaA, Weinheim, 2009.
- [157] J.B. Baxter and E.S. Aydil. Epitaxial growth of ZnO nanowires on a- and c-plane sapphire. *J. Cryst. Growth.*, 274(3-4):407 – 411, 2005.
- [158] T.H. Fang, W.J. Chang, W. Water, and C.C. Lee. Effect of gas concentration on structural and optical characteristics of ZnO nanorods. *Physica E*, 42: 2139–2142, 2010.
- [159] X. Han *et al.* Controllable synthesis and optical properties of novel ZnO cone arrays via vapor transport at low temperature. *J. Phys. Chem. B*, 109:2733–2738, 2005.
- [160] H. Fu, H. Li, W. Jie, and C. Zhang. The O₂-dependent growth of ZnO nanowires and their photoluminescence properties. *Ceramics International*, 33:1119–1123, 2007.
- [161] M. Foley, C. Ton-That, and M.R. Phillips. Luminescent properties of ZnO structures grown with a vapour transport method. *Thin Solid Films*, 518(15): 4231 – 4233, 2010.
- [162] X. Meng *et al.* The structural and optical properties of ZnO nanorod arrays. *Solid State Commun.*, 135(3):179–182, 2005.
- [163] H. Fan *et al.* Well-ordered ZnO nanowire arrays on GaN substrate fabricated via nanosphere lithography. *J. Cryst. Growth.*, 287(1):34–38, 2006.
- [164] P. Sangpour, M. Roozbehi, O. Akhavan, and A.Z. Mosfegh. ZnO nanowires from nanopillars: Influence of growth time. *Curr. Nano.*, 5:479–484(6), 2009.
- [165] C. Ton-That, M. Foley, and M.R. Phillips. Luminescent properties of ZnO nanowires and as-grown ensembles. *Nanotechnology*, 19(41):415606, 2008.

- [166] L.C. Campos *et al.* Determination of the epitaxial growth of Zinc Oxide nanowires on sapphire by grazing incidence synchrotron x-ray diffraction. *Appl. Phys. Lett.*, 90(18):181929, 2007.
- [167] C. Ton-That, M.R. Phillips, M. Foley, S.J. Moody, and A.P.J. Stampfl. Surface electronic properties of ZnO nanoparticles. *Appl. Phys. Lett.*, 92(26):261916, 2008.
- [168] J.D. Prades, A. Cirera, J.R. Morante, and A. Cornet. Ab initio insights into the visible luminescent properties of ZnO. *Thin Solid Films*, 515(24):8670 – 8673, 2007. First International Symposium on Transparent Conducting Oxides.
- [169] H. Xue *et al.* Probing the surface effect on deep-level emissions of an individual ZnO nanowire via spatially resolved cathodoluminescence. *J. Phys. Chem. C*, 113(29):12715–12718, July 2009.
- [170] N. Pan, X. Wang, M. Li, F. Li, and J. Hou. Strong surface effect on cathodoluminescence of an individual tapered ZnO nanorod. *J. Phys. Chem. C*, 111(46):17265–17267, November 2007.
- [171] X. Zhou *et al.* The origin of green emission of ZnO microcrystallites: Surface-dependent light emission studied by cathodoluminescence. *Society*, pages 12091–12093, 2007.
- [172] Z.M. Liao, K.J. Liu, J.M. Zhang, J. Xu, and D.P. Yu. Effect of surface states on electron transport in individual ZnO nanowires. *Phys. Lett. A*, 367(3):207 – 210, 2007.
- [173] E. De la Rosa *et al.* Controlling the growth and luminescence properties of well-faceted ZnO nanorods. *Phys. Chem. C*, 111(24):8489–8495, 2007.
- [174] N.S. Ramgir *et al.* ZnO multipods, submicron wires, and spherical structures and their unique field emission behavior. *Phys. Chem. B*, 110(37):18236–18242, 2006.
- [175] D.Q. Fang, A.L. Rosa, R.Q. Zhang, and T. Frauenheim. Theoretical exploration of the structural, electronic, and magnetic properties of ZnO nanotubes with vacancies, antisites, and nitrogen substitutional defects. *J. Phys. Chem. C*, 114(13):5760–5766, 2010.

- [176] N. Ohashi *et al.* Effect of hydrogen doping on ultraviolet emission spectra of various types of ZnO. *Appl. Phys. Lett.*, 80(16):2869, 2002.
- [177] Y.M. Strzhemechny *et al.* Shallow donor generation in ZnO by remote hydrogen plasma. *J. Elec. Mater.*, 34(4):399–403, April 2005.
- [178] C.G. Van de Walle. Hydrogen as a cause of doping in Zinc Oxide. *Phys. Rev. Lett.*, 85(5):1012–5, July 2000.
- [179] D.C. Look *et al.* Electrical properties of bulk ZnO. *Solid State Commun.*, 105(6):399 – 401, 1998.
- [180] D.M. Hofmann *et al.* Hydrogen: A relevant shallow donor in Zinc Oxide. *Phys. Rev. Lett.*, 88(4):045504, 2002.
- [181] A. Schildknecht, R. Sauer, and K. Thonke. Donor-related defect states in ZnO substrate material. *Physica B*, 340-342:205 – 209, 2003. Proceedings of the 22nd International Conference on Defects in Semiconductors.
- [182] M.D. McCluskey, S.J. Jokela, K.K. Zhuravlev, P.J. Simpson, and K.G. Lynn. Infrared spectroscopy of hydrogen in ZnO. *Appl. Phys. Lett.*, 81(20):3807–3809, 2002.
- [183] E.V. Lavrov, J. Weber, F. Bo, and R. Helbig. Hydrogen-related defects in ZnO studied by infrared absorption spectroscopy . *Phys. Rev. B*, pages 1–7, 2002.
- [184] K. Ip *et al.* Hydrogen incorporation and diffusivity in plasma-exposed bulk ZnO. *Appl. Phys. Lett.*, 82(3):385, 2003.
- [185] Y.M. Strzhemechny *et al.* Remote hydrogen plasma processing of ZnO single crystal surfaces. *J. Appl. Phys.*, 94(7):4256–4262, 2003.
- [186] Y.M. Strzhemechny *et al.* Remote hydrogen plasma doping of single crystal ZnO. *Appl. Phys. Lett.*, 84(14):2545–2547, 2004.
- [187] V. Nikitenko. *Optics and Spectroscopy of Point Defects in ZnO*, pages 69–81. Springer Netherlands, 2005.
- [188] T.M. Brseth *et al.* Identification of oxygen and zinc vacancy optical signals in ZnO. *Appl. Phys. Lett.*, 89(26):262112, 2006.

- [189] A.B. Djurisić *et al.* Defect emissions in ZnO nanostructures. *Nanotechnology*, 18:095702, 2007.
- [190] T. Story, R.R. Galazka, R.B. Frankel, and P.A. Wolff. Carrier-concentration-induced ferromagnetism in PbSnMnTe. *Phys. Rev. Lett.*, 56(7):777–779, Feb 1986.
- [191] S.N. Khanna, B.K. Rao, P. Jena, and M. Knickelbein. Ferrimagnetism in Mn₇ cluster. *Chem. Phys. Lett.*, 378(3-4):374 – 379, 2003.
- [192] J.K. Furdyna. Diluted magnetic semiconductors. *J. Appl. Phys.*, 64(4):R29, 1988.
- [193] T. Dietl, H. Ohno, F. Matsukura, J. Cibert, and D. Ferrand. Zener model description of ferromagnetism in zinc-blende magnetic semiconductors. *Science*, 287:1019, 2000.
- [194] J. Kim, H. Song, and E. Kim. Study of magnetic impurity as defects in ZnO grown by pulsed laser deposition. *Microelectr. J.*, 40:283–285, 2009.
- [195] M. Diaconu *et al.* Deep defects generated in n-conducting ZnO:TM thin films. *Solid State Commun.*, 137:417–421, 2006.
- [196] H. Schmidt *et al.* Electrical and optical spectroscopy on ZnO:Co thin films. *Appl. Phys. A*, 88:157–160, 2007.
- [197] S. Mandal and T. Nath. Microstructural, magnetic and optical properties of ZnO:Mn (0.01 ≤ x ≤ 0.25) epitaxial diluted magnetic semiconducting films. *Thin Solid Films*, 515(4):2535 – 2541, 2006.
- [198] T. Dietl. Ferromagnetic semiconductors. *Semicond. Sci. Tech.*, 17:377, 2002.
- [199] C. Bates, W. White, and R. Roy. The solubility of transition metal oxides in zinc oxide and the reflectance spectra of Mn²⁺ and Fe²⁺ in tetrahedral fields. *J. Inorg. Nucl. Chem.*, 28:397–405, 1966.
- [200] T. Fukumura, Z. Jin, A. Ohtomo, H. Koinuma, and M. Kawasaki. An oxide-diluted magnetic semiconductor:Mn-doped ZnO. *Appl. Phys. Lett.*, 75:3366, 1999.

- [201] A. Polyakov *et al.* Optical and magnetic properties of ZnO bulk crystals implanted with Cr and Fe. *Mat. Sci. Semicon. Proc.*, 7(1-2):77–81, April 2004.
- [202] Z. Wang, X.Y. Ma, J.W. Song, and J.H. Yao. Optical properties of ZnO and Mn-doped ZnO nanocrystals fabrication by vapor phase transport processes. *Nano-Micro Letters*, 1(1):45–48, 2009.
- [203] M. Godlewski *et al.* Optical properties of manganese doped wide band gap ZnS and ZnO. *Optical Materials*, 31:1768–1771, 2009.
- [204] M. Godlewski *et al.* Luminescence of doped nanoparticles of wide band gap II-VI compounds. *Solid State Phenom.*, 128:123–134, 2007.
- [205] L. Chen *et al.* Dimensional dependence of the dynamics of the Mn $3d^5$ luminescence in (Zn, Mn)S nanowires and nanobelts. *Phys. Rev. B.*, 76:115325, 2007.
- [206] V. Avrutin *et al.* Optical and electrical properties of znmno layers grown by peroxide MBE. *Superlattices and Microstructures*, 39:291–298, 2006.
- [207] V.A.L. Roy *et al.* Magnetic properties of Mn doped ZnO tetrapod structures. *Appl. Phys. Lett.*, 84(5):756–758, 2004.
- [208] J. Li *et al.* The effect of Mn²⁺ doping on structure and photoluminescence of ZnO nanofilms synthesized by solgel method. *J. Lumin.*, 122-123:352–354, January 2007.
- [209] S. Senthilkumaar, K. Rajendran, S. Banerjee, T. Chini, and V. Sengodan. Influence of Mn doping on the microstructure and optical property of ZnO. *Mat. Sci. Semicon. Proc.*, 11(1):6–12, 2008.
- [210] R. Delhez, T.H. de Keijser, and E.J. Mittemeijer. The x-ray diffraction line broadening due to the diffractometer condition as a function of 2θ . *J. Phys. E. Sci. Instrum.*, 11(7):649, 1978.
- [211] D.C. Nagle and P.A. Thrower. The importance of strain in crystallite size determinations. *Carbon*, 11:663–664, 1973.
- [212] D. Balzar. Profile fitting of x-ray diffraction lines and Fourier analysis of broadening. *J. Appl. Cryst.*, 25:559–570, 1992.

- [213] G. Williamson and W. Hall. X-ray line broadening from fcc aluminium and wolfram. *Acta Metall. Mater.*, 1:22–31, 1953.
- [214] R.B. Bylsma, W.M. Becker, J. Kossut, and U. Debska. Dependence of energy gap on x and T in $\text{Zn}_{1-x}\text{Mn}_x\text{Se}$: The role of exchange interaction. *Phys. Rev. B*, 33(12):8207–8215, 1986.
- [215] S.S. Lee *et al.* Investigation of the phase separations and the local electronic structures of $\text{Zn}_{1-x}\text{T}_x\text{O}$ ($T = \text{Mn}, \text{Fe}, \text{Co}$) magnetic semiconductors using synchrotron radiation. *J. Appl. Phys.*, 99(8):08M103, 2006.
- [216] G. van der Laan and I.W. Kirkman. The 2p absorption spectra of 3d transition metal compounds in tetrahedral and octahedral symmetry. *J. Phys.: Condens. Matter*, 4:4189, 1992.
- [217] C. Colliex, T. Manoubi, and C. Ortiz. Electron-energy-loss-spectroscopy near-edge fine structures in the iron-oxygen system. *Phys. Rev. B.*, 44:11402, 1991.
- [218] J.W. Chiou *et al.* Electronic structure of ZnO nanorods studied by angle-dependent x-ray absorption spectroscopy and scanning photoelectron microscopy. *Appl. Phys. Lett.*, 84(18):3462–3464, 2004.